Title
Thermomechanical Energy Conversion Using Ferroelectric Materials

Author
McKinley, Ian Meeker

Publication Date
2013

Peer reviewed|Thesis/dissertation

University of California
Los Angeles

Thermomechanical Energy Conversion Using Ferroelectric Materials

A dissertation submitted in partial satisfaction
of the requirements for the degree
Doctor of Philosophy in Mechanical Engineering

by

Ian Meeker McKinley

2013

Abstract of the Dissertation

Thermomechanical Energy Conversion Using Ferroelectric Materials

by

Ian Meeker McKinley

Doctor of Philosophy in Mechanical Engineering

University of California, Los Angeles, 2013

Professor Laurent G. Pilon, Chair

This study is concerned with the direct conversion of thermal and mechanical energy into electricity using ferroelectric materials. These materials possess a spontaneous polarization and can undergo solid-state phase transitions as a result of a change in applied electric field. All ferroelectric materials are pyroelectric, i.e., phase transitions can also be induced by a change in temperature. The Olsen cycle takes advantage of the thermally-induced phase transitions to directly convert thermal energy into electrical energy. It consists of two isoelectric field and two isothermal processes in the electric displacement versus electric field diagram. This study aims to improve the understanding and performance of the Olsen cycle by exploring the use of relaxor ferroelectric lead zirconate niobate-lead titanate (PZN-5.5PT) and lead magnesium niobate-lead titanate (PMN-28PT) single crystals. These materials were chosen for the fact that their phase transitions take place at low temperatures. The performance of the cycle was improved by varying the operating frequency to maximize changes in polarization due to phase transition taking place during the cycle.

Moreover, all pyroelectric materials are also piezoelectric, i.e., phase transitions can occur as a result of a change in applied compressive stress. This study aims to explore new methods to simultaneously convert mechanical and thermal energy directly into electrical energy by combining electric field, compressive stress, and/or thermal cycling to induce phase transitions. Two new energy conversion cycles were conceived and demonstrated

on PMN-28PT for its outstanding piezoelectric response over a broad temperature range. First, a thermomechanical cycle converting thermal and mechanical energy into electricity was performed. It proved to be more versatile than the Olsen cycle by generating electrical energy at all temperatures. It also achieved larger power densities thanks to larger operating frequency. In addition, it improved upon the material efficiency of the Olsen cycle by reducing the heat input during the cycle. Second, a thermally-biased mechanical cycle converting mechanical energy into electricity under a thermal bias was performed. It improved upon the power generation and material efficiency of the thermomechanical cycle by substituting the thermal cycling with a thermal bias to approach the desirable phases. In addition, it was capable of generating larger power per unit volume of material than existing direct mechanical to electrical energy conversion methods.

The dissertation of Ian Meeker McKinley is approved.

Ertugrul Taciroglu

Christopher S. Lynch

Gregory P. Carman

Laurent G. Pilon, Committee Chair

University of California, Los Angeles

2013

Table of Contents

List of Figures

List of Tables

Nomenclature

a	lattice parameter, $\mathring{A}$
A	sample cross-sectional area, m^2
A_s	sample surface area, m^2
b	sample thickness, m
Bi	Biot number ($=hb/k$)
c_p	specific heat, J/kg·K
C	capacitance, F
D	electric displacement, C/m^2
d_{33}	piezoelectric coefficient, C/N
Δh	specific phase change enthalpy, J/kg
E	electric field, V/m
E_{br}	electrical breakdown field, V/m
E_c	coercive electric field, V/m
f	frequency, Hz
g	gravity of Earth (=9.81 m/s^2)
h	heat transfer coefficient, W/m^2·K
k	thermal conductivity, W/m·K
I_p	electric current, A
M_A	monoclinic M_A crystal phase
M_B	monoclinic M_B crystal phase
M_C	monoclinic M_C crystal phase
$mol\%$	molar fraction, %
MPB	morphotropic phase boundary
N_D	energy density, J/L
Nu	Nusselt number
O	orthorhombic crystal phase

p_c	pyroelectric coefficient, $\mathrm{C/m^2{\cdot}K}$
P	polarization density, $\mathrm{C/m^2}$
P_D	power density, W/L
P_r	remnant polarization, $\mathrm{C/m^2}$
P_s	saturation polarization, $\mathrm{C/m^2}$
Q	charge, C
Q_{in}	thermal energy input per unit volume, $\mathrm{J/m^3}$
PE	pyroelectric element
R	rhombohedral crystal phase
R	resistance, Ω
Ra	Rayleigh number
S	side length, m
s_{33}	elastic compliance, $\mathrm{m^2/N}$
t	time, s
T	tetragonal crystal phase
T	temperature, ^{o}C or K
T_{Curie}	Curie temperature, ^{o}C
x	molar fraction of lead titanate, %
x_3	strain in longitudinal direction $[=\int_{T_C}^{T}\alpha(T)\,\mathrm{d}T]$
$\not{V}$	volume, $\mathrm{m^3}$
V	voltage, V
V_1	voltage across capacitor, V
V_2	voltage across resistor, V
W_{in}	mechanical energy input per unit volume, $\mathrm{J/m^3}$

Greek symbols

α	linear thermal expansion coefficient, $\mathrm{K^{-1}}$
δ	relative error between experimental data and model predictions, %

ε_o	vacuum permittivity (= 8.854x10^{-12} F/m)
ε_r	relative permittivity
η	material efficiency, %
ν	kinematic viscosity, m^2/s
ρ	density, kg/m^3
σ	elastic stress, Pa
τ_t	thermal characteristic time constant, s
τ_{ij}	duration of process i-j, s

Subscripts

avg	refers to average
b	refers to bias
$cold$	refers to cold
eff	refers to effective
f	refers to fluid
H	refers to high
hot	refers to hot
L	refers to low
max	refers to maximum
PE	refers to pyroelectric element

Acknowledgments

I would like to thank my advisor, Professor Laurent Pilon, for his guidance and encouragement throughout the duration of my doctoral work. I am also grateful to Professor Christopher S. Lynch for providing me access to his lab and equipment. My thanks also go to Professor Gregory P. Carman for inspiring my ideas relating to ferroelectric energy conversion during his lectures on smart materials. Furthermore, I would like to thank Professor Ertugrul Taciroglu for serving on my thesis committee. I would also like to express my appreciation to Dr. Ignacio Martini for his assistance with the equipment in the Materials Creation Training Program laboratory. I would also like to acknowledge my fellow student collaborators Felix Y. Lee, Sam Goljahi, Bingang Mei, Razmig Kandilian, and Thomas K. Chin. Finally, I would like to thank Meredith Martin-Almy and my family for their endless love and support.

This research has been supported in part by NSF-IGERT program Clean Energy for Green Industry at UCLA (NSF Award 0903720). In addition, this material is based upon work supported by the NSF-IGERT Materials Training Program under grant no. DGE-0114443.

Vita

2010	B.A., Physics 3/2 Occidental College Los Angeles, CA
2010	B.S., Mechanical Engineering with Latin Honors, Cum Laude Columbia University New York, NY

CHAPTER 1

Introduction

This chapter presents the motivations and background of this study. First, it discusses energy usage in our society and the inevitable production of waste mechanical and thermal energies and their ubiquitous nature. This is followed by a brief discussion of common methods of converting ambient mechanical energy and waste heat into useful electrical energy. This chapter concludes with the objectives of this study and the scope of the document.

1.1 Motivations

Our society is facing a combination of economic, environmental, demographic, and energy challenges that are exerting stress on the Earth's natural resources and the quality of life of its inhabitants. In fact, the world population grew by 79% from 3.9 to 7.0 billion people between 1973 and 2010.[1] Furthermore, the world population is projected to increase by 2.3 billion people before 2050.[2] In the same time period, urban areas are projected to grow by 2.9 billion people and absorb the majority of this population growth.[3] This will result in a significant increase in energy demand. Therefore, these trends call for more efficient and less polluting energy technologies.

Recent pursuits in efficient and clean energy include the advancement of solar photovoltaic and wind turbine technologies. These energy technologies convert solar and wind energy directly into electricity. A number of other harvestable ambient energy sources exist, including waste heat, vibrations, electromagnetic waves, and flowing water.[4] In fact, ambient energy sources with the largest energy densities are light, thermal gradients, thermal variations, and mechanical vibrations and strains.[5] The present study focuses on converting

thermal energy and mechanical energy directly into electricity.

1.2 Mechanical and thermal energy sources

Waste mechanical energy is the inevitable by-product of objects in motion and exists in the form of vibrations, shocks, or strains.[5] Vibrations are characterized by high frequency, small amplitude displacements and their sources include household appliances with motors, industrial plant equipment, moving vehicles, and structures such as buildings and bridges.[6] On the other hand, strains are characterized by low frequency, high amplitude displacements and their sources include fluid flow such as air movements and the human body.[7]

Waste heat can be divided into three categories: low, medium, and high grade heat with temperatures ranging from 27 to 205^{o}C, 205 to 593^{o}C, and 593 to 1649^{o}C, respectively.[8] For example, the second law of thermodynamics requires that power, refrigeration, and heat pump cycles produce waste heat.[9] It is often released into the atmosphere in the form of hot gases or hot water. High-grade waste heat is typically the by-product of large scale industrial processes such as power plants and oil refineries. On the other hand, heat dissipated from servers, data centers, solar panels, and internal combustion engines falls into the medium and low-grade heat categories. Figure 1.1 shows estimates of the energy consumed, used, and wasted in the United States in 2012 in quadrillion British thermal units (10^{15} BTU).[10] It establishes that only 38.9% of the raw energy consumed, such as petroleum, natural gas, and coal, was used for useful ends while the remaining 61.1% was wasted. For example, Figure 1.1 demonstrates that only 21% of the energy consumed in the transportation sector was useful while the remaining 79% was lost primarily in the form of low-grade waste heat.[11] Similarly, nearly 70% of the energy consumed for generating electricity was wasted mainly in coal, natural gas, or nuclear power plants. As the demand for energy continues to increase, it would be beneficial to harvest this large amount of heat that would otherwise be wasted by converting it into usable energy.

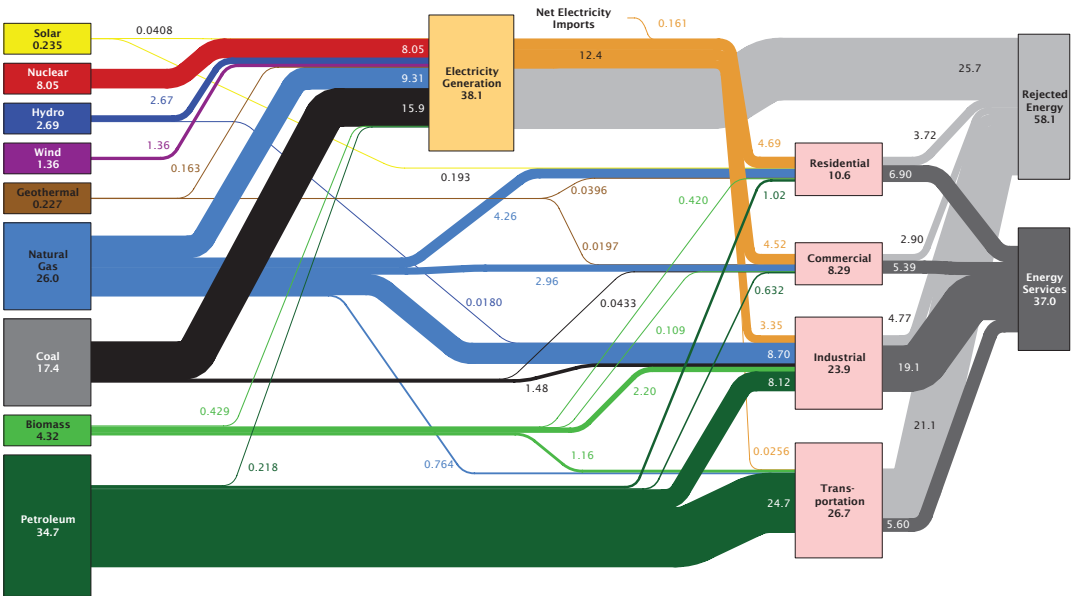

Figure 1.1: Flow chart of the energy produced, used, and wasted in the United States in 2012 (unit in quads, 10^{15} Btu).[10]

1.3 Waste mechanical energy conversion

Methods for direct mechanical to electrical energy conversion include electromagnet, electrostatic, electroactive polymer, and piezoelectric generators.[5] Electromagnetic generators rely on time-varying magnetic fields caused by the relative motion between a magnet and a coil to generate electrical energy.[5] Electrostatic generators rely on temporal variations in the capacitance of a structure caused by mechanical motion to generate electrical energy.[5] By contrast, electroactive polymers generate electrical energy in response to a large change in shape or size due to mechanical deformations.[5]

Piezoelectric energy conversion is the most widely used method to harvest mechanical energy.[4] It consists of directly converting time-dependent mechanical deformations into electricity.[4,5] It makes use of the piezoelectric effect to create a flow of charge to or from the surface of a piezoelectric material as a result of successive deformations.[5] Piezoelectric energy conversion can be divided into two categories, namely (i) inertial and (ii) kinematic. Inertial piezoelectric energy conversion relies on the resistance to acceleration by a mass.[12] This type

of piezoelectric energy harvesting aims to convert high frequency, low amplitude vibrations into electrical energy.[6] A typical inertial harvester consists of a piezoelectric cantilever beam with a mass at the tip. Acceleration from vibration occurs at the base and the inertia of the tip mass bends the cantilever. Inertial devices typically operate near a resonant frequency to enhance the amplitude of the tip oscillation.[6] On the other hand, kinematic piezoelectric energy conversion does not rely on inertia or resonance. Instead, the piezoelectric material is connected to the mechanical energy source at more than one point so that it is directly coupled to the flexing, extension, or compression of the source.[12] In both of these cases, electrodes are deposited on opposite faces of the piezoelectric material and connected to a resistive electrical load. The use of piezoelectric materials to harvest mechanical energy has been explored both experimentally and theoretically and was thoroughly reviewed in Refs.[4,13] Research related to piezoelectric energy harvesting has focused mainly on exploring the performance of different materials and loading configurations as well as on circuitry for conditioning and storing the generated power.[4,13]

1.4 Waste heat energy conversion

High-grade waste heat can be easily converted efficiently to electricity or hot water for district heating or industrial thanks to cogeneration.[14] On the contrary, harvesting medium and low-grade waste heat is challenging due to the low temperature and the associated small Carnot efficiency. However, technologies exist to convert such waste heat into usable energy, namely (i) Stirling engines,[15] (ii) organic Rankine cycles,[16,17] and (iii) thermoelectric generators.[18,19] Stirling engines and organic Rankine cycles convert heat into mechanical energy, while thermoelectric generators directly produce electrical energy by means of a steady-state temperature difference at the junction of two dissimilar metals or semiconductors.

Alternatively, pyroelectric energy conversion directly converts low-grade waste heat into electricity.[20–40] It makes use of the pyroelectric effect and time-dependent temperature oscillations to create a flow of charge to or from the surface of a pyroelectric material as a result of successive heating and cooling.[41] Pyroelectric energy conversion can be divided into two

categories, namely (i) passive pyroelectric conversion and (ii) solid-state thermodynamic cycles.

The first category of pyroelectric energy harvesting consists of connecting a pyroelectric material to a resistive electrical load and subjecting it to cyclic temperature fluctuations.[12] In this case, the pyroelectric material typically undergoes temperature fluctuations on the order of 10^oC or less.[37,42,43] This type of pyroelectric energy conversion suffers from small electrical energy and power outputs.[44]

On the other hand, the Olsen cycle subjects a pyroelectric material to temperature fluctuations on the order of 50^oC. The cycle was developed by Olsen and co-workers between 1978 and 1985.[26,28,41,45–49] It can be represented in the electric displacement (charge per unit area) versus electric field (D-E) diagram of a pyroelectric material. It is analogous to the Ericsson cycle defined in the pressure versus specific volume diagram of a working fluid.[20] It consists of two isothermal and two isoelectric processes performed on a pyroelectric element (PE) consisting of a pyroelectric slab or film coated with electrodes on opposite faces.[20] Figure 1.2 shows the isothermal bipolar hysteresis curves between electric displacement D and electric field E exhibited by a non-linear pyroelectric material at two different temperatures T_{cold} and T_{hot}. Figure 1.2 also illustrates the four processes of the Olsen cycle. Process 1-2 consists of charging the pyroelectric element at T_{cold} by increasing the applied electric field from E_L to E_H. Process 2-3 corresponds to discharging the PE by heating it from T_{cold} to T_{hot} under constant electric field E_H. Process 3-4 consists of reducing the electric field from E_H to E_L under isothermal conditions at T_{hot}. Finally, Process 4-1 closes the cycle by cooling the PE from T_{hot} to T_{cold} under constant electric field E_L. In brief, the principle of the Olsen cycle is to charge a capacitor via cooling at small electric field and to discharge it under heating at large electric field. It has been demonstrated to produce both the largest electrical energy[50] and power[51] per unit volume of material of among the different pyroelectric and piezoelectric energy conversion methods.

The generated energy density N_D is defined as the electrical energy produced per unit volume of the material per cycle. It is expressed in J/L/cycle (1 J/L/cycle=1 mJ/cm^3/cycle)

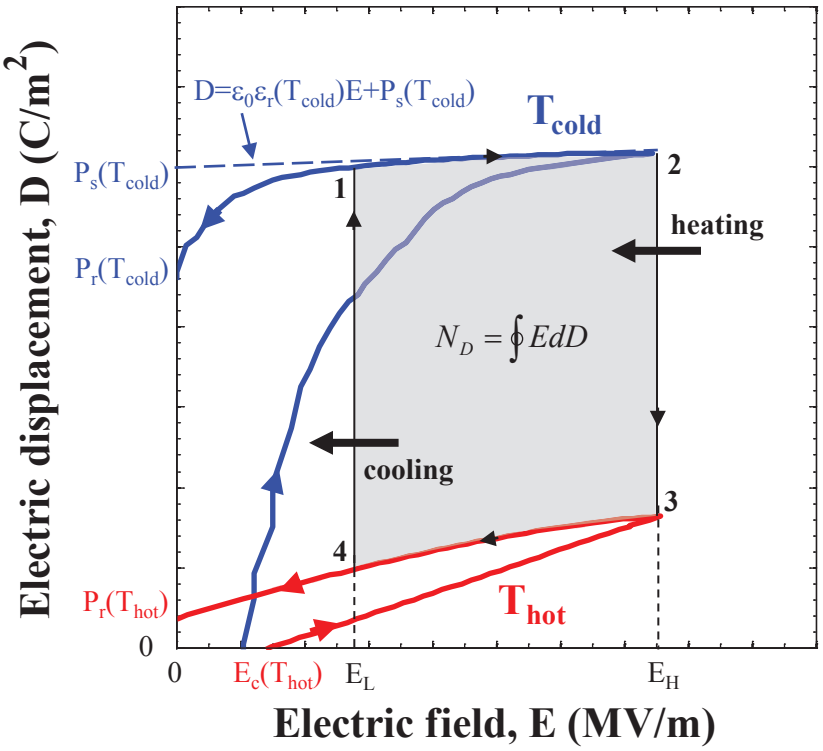

Figure 1.2: Isothermal bipolar electric displacement versus electric field (D-E) hysteresis loops for a typical pyroelectric material at temperatures T_{hot} and T_{cold} along with the Olsen cycle. The electrical energy generated per unit volume of material per cycle N_D is represented by the area enclosed between 1-2-3-4.

and defined as[20]

$$N_D = \oint E\mathrm{d}D \tag{1.1}$$

The area enclosed by the four states 1 to 4 shown in Figure 1.2 correspond to N_D. The power density P_D is the amount of energy generated by the pyroelectric material per unit volume per unit time. It is expressed in W/L and defined as

$$P_D = N_D f \tag{1.2}$$

where f is the overall cycle frequency defined as $f = (\tau_{12} + \tau_{23} + \tau_{34} + \tau_{41})^{-1}$ where τ_{ij} is the duration of process i-j. Note that N_D is also dependent on the cycle frequency.[34,52]

1.5 Pyroelectric materials

Categories of pyroelectric materials include

1. ceramics such as lead zirconate titanate (PZT), barium titanate ($BaTiO_3$), and lithium titanate ($LiTiO_3$).[45]

2. single crystals such as lead magnesium niobate-lead titanate (PMN-PT) and lead zirconate niobate-lead titanate (PZN-PT).[53–56]

3. polymers like polyvinylidene fluoride (PVDF), polyvinylidene fluoride trifluoroethylene (P(VDF-TrFE)), and polyvinylidene fluoride trifluoroethlyene chlorofluoroethylene (P(VDF-TrFE-CFE)).[45,49]

4. biological materials including bovine phalanx, femur bones, and collagen (found in fish scales and hair).[41,57]

5. minerals such as tourmaline and quartz.[41]

Ceramics and single crystals based on the lead zirconate titanate system (PZT) are the most commonly used material in piezoelectric and pyroelectric applications since they are strong and chemically stable.[41] In addition, variation of the Zr/Ti ratio and the addition of dopants in PZT may favorably alter the physical properties of the materials.[41] On the other hand, polyvinylidene fluoride polymer (PVDF) and its copolymers are inexpensive to fabricate, can be operated at low temperatures, and possess large energy densities per unit mass. In addition, polymers have large mechanical resistance while single crystals and ceramics are delicate and susceptible to aging.[5] However, pyroelectric polymers suffer from lower electrical resistivity responsible for leakage current under large temperature and electric fields.[51] Furthermore, crystalline and ceramic materials are more efficient than polymers at converting mechanical energy into electricity.[5] Based on these observations, this study is limited to pyroelectric single crystals, and in particular to relaxor ferroelectric lead zirconate niobate-lead titanate (PZN-PT) and lead magnesium niobate-lead titanate (PMN-PT) for their outstanding electromechanical properties.[56]

1.6 Objectives of this study

The objectives of the present study are as follows: (1) to improve our understanding and the performance of the Olsen cycle by exploring the use of different materials and by taking advantage of solid-state phase transitions, (2) to explore new methods to simultaneously convert mechanical and thermal energy directly into electrical energy. The tasks to achieve these objectives can be listed as follows:

Objective 1

1. To measure the energy and power densities of PZN-5.5PT and PMN-28PT single crystals undergoing the Olsen cycle under various operating conditions.
2. To fully characterize the dielectric properties of PMN-28PT single crystals under various temperatures and uniaxial stresses.
3. To elucidate the dynamic effects of phase transition and thermal expansion in PMN-28PT on pyroelectric energy conversion based on the Olsen cycle.

Objective 2

1. To conceive and demonstrate a thermomechanical power cycle capable of simultaneously harvesting waste heat and/or mechanical energy.
2. To conceive and demonstrate a thermally-biased mechanical power cycle capable of harvesting mechanical energy under a thermal bias.
3. To develop a physical model predicting the energy and power densities of the new thermally-biased mechanical power cycle.

1.7 Scope of this document

Chapter 2 reviews the current state of knowledge in ferroelectric materials and presents the experimental implementation of the Olsen cycle. Chapters 3 describes experimental measurement of the energy and power densities generated by PZN-5.5PT undergoing the Olsen

cycle. Chapter 4 presents characterization of the dielectric and thermal properties of single crystal PMN-28PT under various electric fields, temperatures, and compressive stresses. Chapter 5 explores the dynamic effects of phase transitions and thermal expansion on the energy conversion of PMN-28PT single crystals subjected to the Olsen cycle. Chapter 6 describes a novel thermomechanical energy conversion cycle capable of simultaneously converting mechanical and thermal energy directly into electricity. Its practical demonstration on PMN-28PT and the effects of different operating parameters on the energy and power generation performance are discussed in detail. Chapter 7 describes a novel thermally-biased energy conversion cycle performed on pyroelectric materials capable of directly converting mechanical energy into electricity under a thermal bias. It was demonstrated on PMN-28PT under various temperatures, compressive stresses, and cycle frequencies. Finally, Chapter 8 summarizes the different conclusions that can be drawn from this study and provides recommendations for future research.

CHAPTER 2

Current State of Knowledge

This chapter presents an overview of the material science background necessary to this study. Then, it reviews the current state of knowledge of relaxor ferroelectric single crystals PZN-PT and PMN-PT used in this study. Next, implementation and performance of the Olsen cycle used for thermal to electrical energy conversion are discussed in detail.

2.1 Material considerations

2.1.1 Dielectric materials

A dielectric material is an electrical insulator that can be polarized by an applied electric field. When a dielectric material is subject to an applied electric field, electric charges do not flow through the material, unlike in electrical conductors. Instead, the charges slightly shift from their average equilibrium positions causing dielectric polarization.[45] Dielectric materials are widely used in capacitors and resonators.[45]

Figure 2.1 depicts a dielectric material with thickness b (in m) and cross-sectional area A (in m^2) sandwiched between two electrodes subjected to an electric field E (in V/m). The field is perpendicular to the electrode surface and its amplitude is given by,

$$E = \frac{V}{b} \tag{2.1}$$

where V is the applied voltage (in V). The maximum electric field that the material can withstand without being conductive is called the electric breakdown field or dielectric strength denoted by E_{br}.[45] For applied fields larger than E_{br}, the material is no longer an insulator and instead charges are conducted through it.

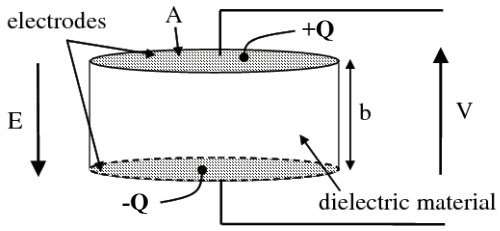

Figure 2.1: Schematic of a dielectric sample of thickness b with metallic electrodes subjected to an electric field E and collecting charges $+Q$ and $-Q$.

The applied electric field causes electrical charges to accumulate at the surface of the material. The amount of charge Q per unit area A is called the electric displacement D (in $\mathrm{C/m^2}$) defined as

$$D = \frac{Q}{A} = \varepsilon_r \varepsilon_0 E + P \tag{2.2}$$

where ε_r is the relative permittivity, ε_0 is the vacuum permittivity ($= 8.854\times10^{-12}$ F/m) and P is the polarization density (in $\mathrm{C/m^2}$). Here, the electric displacement, electric field, and polarization are all vectors that may not be collinear. However, for simplicity, and unless otherwise noted, they are discussed in terms of their component in the direction normal to the electrode surface.

2.1.2 Crystalline dielectric material classifications

There are a total of 32 crystal classes of dielectric materials.[45] Twenty of these classes have an asymmetric structure and are called piezoelectric materials.[45] Ten of the twenty piezoelectric materials also have a unique polar axis.[45] Materials belonging to these ten classes are called pyroelectrics. Furthermore, there is a subgroup of pyroelectric materials known as ferroelectrics. The orientation of the polarization vector of these materials can be switched by the application of an electric field. Note that while all ferroelectrics are

pyroelectric and all pyroelectrics are piezoelectric, the converse is not true. Figure 2.2 illustrates how these different crystals can be classified into the different categories.

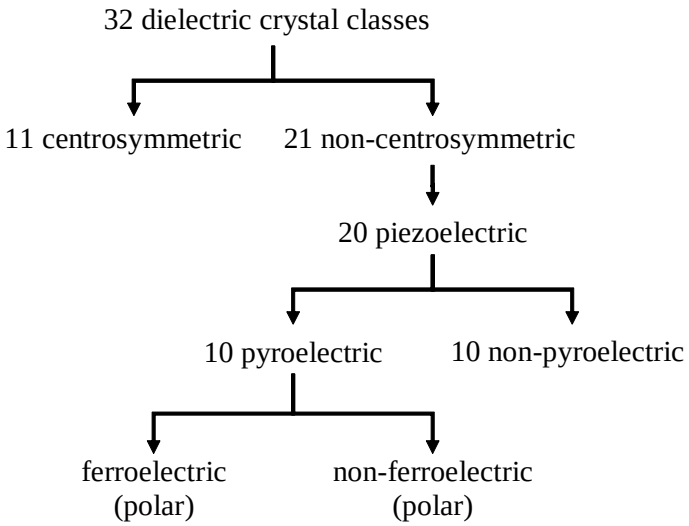

Figure 2.2: Classification of dielectric crystal symmetry classes depicting the relationship between piezoelectric, pyroelectric, and ferroelectric materials.[45]

2.1.2.1 Piezoelectricity

A piezoelectric material has the ability to generate an electric potential in response to an applied mechanical stress or vice versa.[58] Piezoelectricity is observed only in dielectric materials and requires (i) anisotropy in the material and (ii) a structure that does not possess a center of symmetry.[58] The application of a mechanical or electrical stress to a piezoelectric material causes a displacement of the centers of mass of positive and negative charges.[59] Because of the absence of a center of symmetry in the structure, the charge displacement is non-symmetrical resulting in a dipole moment.[59] If this dipole moment is produced by a mechanical stress, it will cause a change in charge at the material surface. Conversely, if an external field displaces the charges by electrostatic attraction or repulsion, the dipole moment produces the mechanical strain which causes the material to deform.[59] Small changes in me-

chanical stress in the poling direction cause proportional changes in the electric displacement according to[58,60]

$$\mathrm{d}D = d_{33}\mathrm{d}\sigma \tag{2.3}$$

where σ is the compressive stress (in Pa) applied in the direction parallel to the polarization and d_{33} is the piezoelectric coefficient (in C/N) defined as[58,60]

$$d_{33} = \left(\frac{\partial D}{\partial \sigma}\right)_{E,T} = \left(\frac{\partial P}{\partial \sigma}\right)_{E,T} \tag{2.4}$$

where T is the temperature (in ^{o}C) and E is the electric field (in V/m). Note that the piezoelectric coefficient is a matrix that can be treated as a scalar corresponding to its element d_{33} if the electrodes are normal to the applied stress. The electric current I_p generated by piezoelectric materials due to changes in compressive stress perpendicular to the electrode surface is given by[58,60]

$$I_p = Ad_{33}\frac{\mathrm{d}\sigma}{\mathrm{d}t} \tag{2.5}$$

where A is the electrode surface area (in m^2). Note that Equation (2.5) is not valid for large changes in compressive stress due to non-linear behavior in electric displacement versus stress.[61]

2.1.2.2 Pyroelectricity

Pyroelectricity is defined as the manifestation of the temperature dependence of the spontaneous polarization of certain anisotropic materials.[45] A pyroelectric material exhibits a temperature-dependent spontaneous polarization defined as the average electric dipole moment per unit volume in absence of an applied electric field.[62] The spontaneous polarization is strongly dependent on temperature due to the pyroelectric material's crystallographic structure.[41] Small changes in temperature cause proportional changes in the electric displacement according to[41]

$$\mathrm{d}D = p_c\mathrm{d}T \tag{2.6}$$

where p_c is the pyroelectric coefficient (in C/m^2·K) defined as[41]

$$p_c = \left(\frac{\partial D}{\partial T}\right)_{E,\sigma} = \left(\frac{\partial P}{\partial T}\right)_{E,\sigma} \tag{2.7}$$

where σ is the applied stress (in Pa) and E is the electric field (in V/m). The pyroelectric coefficient is a vector which can be treated as a scalar if the electrodes are normal to the poling direction. The electric current I_p generated by pyroelectric materials during heating and cooling is given by[26]

$$I_p = A p_c \frac{\mathrm{d}T}{\mathrm{d}t} \tag{2.8}$$

where A is the electrode surface area. Note that Equation (2.8) is not valid for large temperature changes due to non-linear behavior in electric displacement versus temperature.[63]

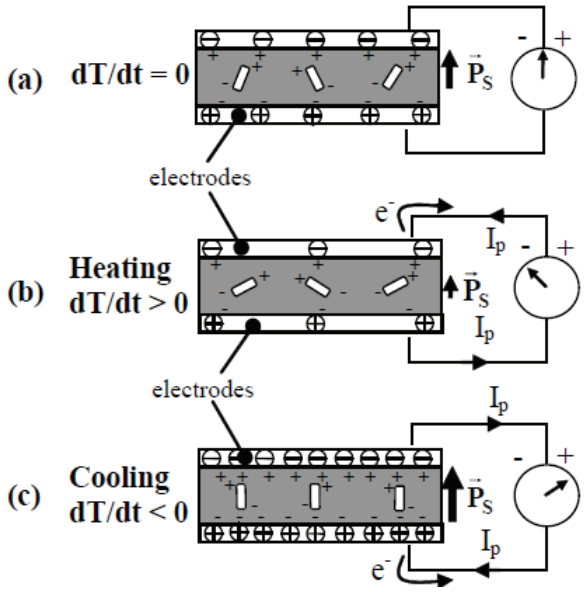

Figure 2.3: Schematic of a pyroelectric sample with electrodes and connected to an ammeter (a) at constant temperature, (b) while being heated, and (c) while being cooled (adapted from Lang[41]).

Figure 2.3 depicts the pyroelectric effect taking place in a pyroelectric material.[41] Figure 2.3a illustrates the case when electrodes deposited onto the top and bottom surfaces

of the pyroelectric film are connected to an ammeter. Under steady-state (dT/dt = 0), the spontaneous polarization remains constant and therefore no current flows through the ammeter. Figure 2.3b illustrates the material subject to a temperature increase (dT/dt > 0). The electric dipole moments lose their orientation, leading to a decrease in spontaneous polarization and a flow of electric current. Similarly, Figure 2.3c shows the material during cooling (dT/dt < 0). The electric dipole moments become more oriented thus increasing the spontaneous polarization and reversing the current through the ammeter.

2.1.2.3 Ferroelectricity

Ferroelectric materials have a spontaneous polarization that can be switched by reversing the applied electric field.[45] Their electric displacement D features a history-dependent response to an external electric field characterized by non-linear hysteresis loops. Figure 2.4 illustrates the relationship between electric displacement D and electric field E (D-E loops) for a typical ferroelectric material. These so-called D-E loops travel in a counter-clockwise direction and exhibit 180^o rotational symmetry about the origin. The electric displacement in the absence of an applied electric field is the remnant polarization P_r while the field needed to reach zero electric displacement is the coercive electric field E_c.[64]

The polarization density of a ferroelectric material can be expressed as the sum of (i) the induced polarization due to the displacement of space charges, ions, and electrons in the material in the presence of an electric field and (ii) the polarization due to the spontaneous alignment of dipoles in the material.[65] Then, for a ferroelectric material at temperature T at large electric field E under compressive stress σ in the poling direction, Equation (2.2) can be written as[45,61]

$$D(E,T,\sigma) = \varepsilon_0 \varepsilon_r(T,\sigma)E + P_s(T,\sigma) \tag{2.9}$$

Here, $\varepsilon_r(T,\sigma)$ is the large-field relative permittivity of the material at temperature T and under stress σ. The saturation polarization $P_s(T,\sigma)$ is equal to the electric displacement in the linear fit of D versus E at large-field extrapolated to zero electric field[66] and the slope of

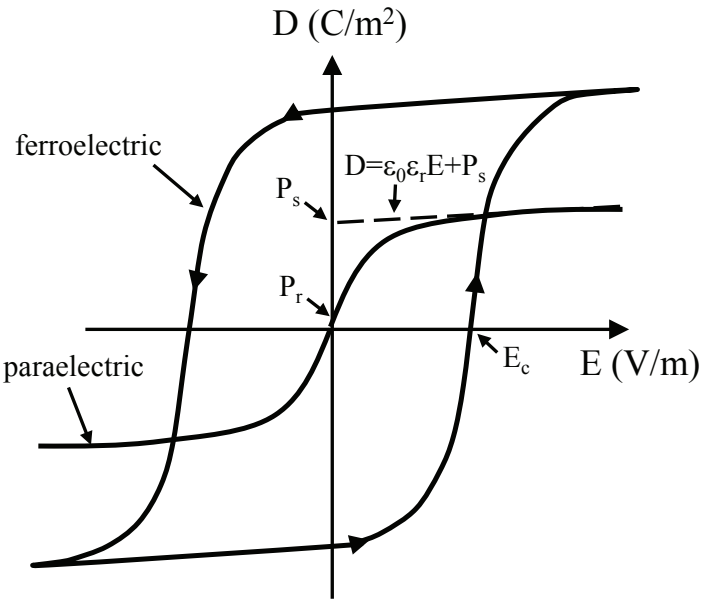

Figure 2.4: Typical electric displacement D versus electric field E diagram for ferroelectric and paraelectric materials.

this linear fit corresponds to the product $\varepsilon_0\varepsilon_r(T,\sigma)$ as illustrated in Figure 2.4. Note that the relative permittivity of a pyroelectric material $\varepsilon_r(T,\sigma)$ is assumed to be independent of electric field for the large electric fields considered. This assumption is valid when a single phase is present in a ferroelectric single crystal.[67] Also note, in the following chapters, references to $P_s(T)$ and $\varepsilon_r(T)$ imply the saturation polarization and large-field relative permittivity for temperature T in the absence of compressive stress.

2.1.2.4 Paraelectricity

Paraelectricity occurs in crystal phases in which electric dipoles are unaligned. Paraelectric materials do not have spontaneous polarization but may become polarized when subjected to an external electric field.[68] Paraelectric behavior occurs due to (i) the distortion of individual ions and (ii) the polarization of molecules.[69] The domains are unordered and the internal

electric field is weak in comparison to that of ferroelectric materials.[68] Figure 2.4 shows an ideal bipolar D-E loop of a paraelectric material featuring local lattice distortions.[70] It is characterized by zero remnant polarization and non-zero saturation polarization. As the electric field increases, ferroelectric domains grow.[71] Such a non-linear D-E loop exhibiting paraelectric behavior at small electric fields and ferroelectric behavior at large fields is called a double hysteresis loop.[72] However, paraelectric materials may also exhibit linear behavior in D vs. E provided there is a sufficient energy barrier to poling. In this case, both the remnant and saturation polarizations are small. In reality, all paraelectric D-E loops exhibit hysteresis and have small, non-zero remnant polarization.

2.1.3 Phase transitions

As previously discussed, an applied electric field can cause a paraelectric to ferroelectric phase transition in ferroelectric materials. In addition, heating ferroelectric materials can cause a phase transition into the paraelectric phase. The temperature at which this transition occurs is called the Curie temperature (or Curie point) denoted by T_{Curie}. It depends on the magnitude, direction, and frequency of the applied electric field as well as the applied compressive stress.[61] It is defined as the temperature corresponding to the maximum of the real part of the complex relative permittivity for a given electric field and compressive stress.[73] The Curie temperature typically increases with increasing electric field.[74] On the contrary, it typically decreases with increasing compressive stress applied in the poling direction.[75] In addition, a ferroelectric material may undergo phase transitions between different ferroelectric phases as a result of changing stress, temperature, and/or electric field conditions.[76]

2.2 Selected pyroelectric materials

2.2.1 PZN-xPT single crystals

Relaxor ferroelectric lead zirconate niobate-lead titanate PZN-xPT have been studied extensively as they are popular ferroelectric materials used in sensors and actuators for their strong electromechanical coupling.[77–86] Poled single crystal PZN-4.5PT undergoes a phase transformation sequence from rhombohedral (R) to tetragonal (T) to depolarized cubic (C) during heating from 25 to 160^{o}C under zero electric field.[82] A small fraction of rhombohedral domains exist in the tetragonal phase.[82] The phase diagram for PZN-xPT at zero electric field indicates that, for PZN-5.5PT, the rhombohedral to tetragonal phase transition occurs between 122 and 130^{o}C and the tetragonal to cubic transition occurs around T_{Curie}=165^{o}C at zero-field.[83] Renault *et al.*[86] showed that during field cooling from 177 to 27^{o}C [001]-oriented PZN-4.5PT has an additional orthorhombic (O) phase and undergoes a C-T-O-R phase transition sequence between these temperatures. Note that the orthorhombic phase was not depolarized and its polarization vector was in the [101] direction.[86] The authors also demonstrated that the transition temperatures were dependent on the applied electric field which varied from 0 to 300 kV/m.[86]

Ren *et al.*[77] showed that electric field induced phase transitions and piezoelectric properties of PZN-xPT are strongly dependent on temperature and composition for x between 4.5 and 8 mol%. In addition, Shen and Cao[80] reported the temperature dependence of the piezoelectric, pyroelectric, and dielectric properties of PZN-xPT poled by two different methods for x equal to 4.5 and 8 mol%. The relative permittivity and saturation polarization of PZN-4.5PT were found to be extremely sensitive to (i) the applied electric field used during poling[85] and (ii) to the poling method.[80] Although the properties of PZN-4.5PT have been reported in the literature,[77–86] to the best of our knowledge, dielectric properties of PZN-5.5PT, investigated in this study, have not been reported.

2.2.2 PMN-xPT single crystals

Relaxor ferroelectric lead magnesium niobate-lead titanate PMN-xPT ferroelectric single crystals with x ranging from 0 to 35 mol% display large electromechanical coupling and piezoelectric coefficients.[76] In fact, single crystal PMN-xPT possesses extraordinarily large piezoelectric constants near the morphotropic phase boundary (MPB) separating the rhombohedral and tetragonal phases.[87] This phase boundary in PMN-xPT corresponds to x ranging between 27.5 and 33 mol%.[88] In addition, the physical properties of these crystals are related to their domain structures and phase states.[76,89,90] The phase of these crystals is a function of composition, temperature, applied stress, as well as magnitude, frequency, and direction of applied electric field.[75,76,91] Furthermore, Zhou *et al.*[92] determined in a comparison of PMN-xPT with x equal to 28, 30, and 32 mol% that 28 mol% is the preferred composition for applications in transducers, sensor, and actuators due to its larger piezoelectric response in a broad temperature range. Based on these observations, single crystal PMN-28PT samples are used in the present study.

Figure 2.5 shows the phases and domain states of PMN-28PT single crystals under electric field E and compressive stress σ loading along the [001] direction. PMN-xPT near the MPB assumes the phases rhombohedral (R), monoclinic M_A, M_B, and M_C, tetragonal (T), cubic (C), and orthorhombic (O) depending on stress, electric field, and temperature.[74–76,93] Figure 2.6 illustrates the directions and planes of the polarization vector for the different crystal phases in a relaxor ferroelectric single crystal. Note that, for clarity, Figure 2.6 shows only one polarization vector for each phase. In reality, PMN-28PT single crystals possess four equivalent polarization vectors as shown in Figure 2.5. The polarization vector is oriented in the [111] direction for the rhombohedral phase and along the (110) and (100) planes for the M_A and M_C phases, respectively.[86,94] For the tetragonal phase, the polarization vector is oriented in the [001] direction.[94] At room temperature under zero electric field, PMN-28PT is in the rhombohedral phase[93] and is poled into the monoclinic M_A phase at 0.2 MV/m.[74] In addition, the material has a monoclinic-tetragonal (M-T) phase boundary at 90^{o}C under zero electric field.[74] This phase boundary temperature decreases to 85^{o}C and 70^{o}C as the electric

field increases to 0.2 and 0.8 MV/m, respectively.[74] Note that an intermediate monoclinic M_C phase exists in some PMN-28PT samples between the monoclinic M_A and tetragonal phases.[74] The phase transition sequence from the R phase to the T phase is characterized by continuous rotation and increase in polarization with each transition.[95] Further heating in the tetragonal phase leads to relaxation into the depolarized cubic phase at the zero-field Curie temperature T_{Curie}=126°C.[74] The Curie temperature shifts to 153 and 166°C as the [001] electric field increases to 0.2 and 0.3 MV/m, respectively.

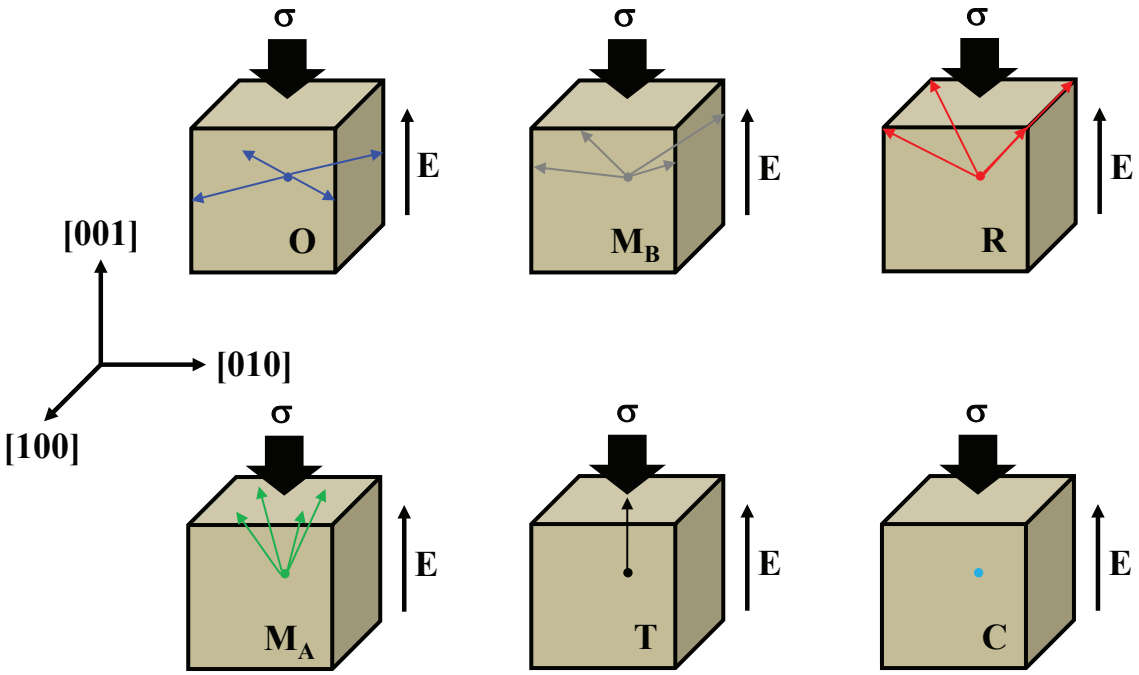

Figure 2.5: Possible phases and domain states of PMN-28PT single crystal under [001] electric field and stress loading. Phases include orthorhombic (O), monoclinic M_B, rhombohedral (R), monoclinic M_A, tetragonal (T), and cubic (C).

To the best of our knowledge, the phase boundaries of [001] PMN-28PT have not been reported as a function of temperature, electric field, and compressive stress. However, McLaughlin *et al.*[76] investigated the phases boundaries of [001] PMN-32PT. In PMN-32PT, the electric fields corresponding to the R-M_A and M_A-T phase boundaries increase with in-

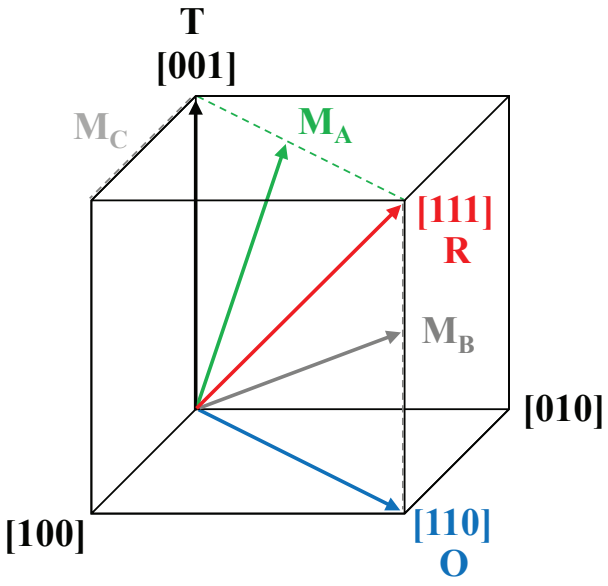

Figure 2.6: Orientation of the polarization vector for different phases in relaxor ferroelectric single crystals.

creasing compressive stress for a given temperature.[76] In addition, the material takes on a depolarized orthorhombic (O) phase under large compressive stress and small electric field.[76] This unpoled phase has an in-plane random distribution of spontaneous polarization perpendicular to the [001] direction.[76] However, it is not present under zero-stress conditions[76] due to the fact that it is usually unstable.[75] In addition, rhombohedral to orthorhombic (R-O) phase transition occurs with the application of compressive stress to [001] PMN-32PT for temperature below 60^{o}C.[76] However, a direct monoclinic M_A to orthorhombic (M_A-O) phase transition occurs with the application of compressive stress for temperature above 60^{o}C.[76] Furthermore, the O-M_A and M_A-T phase transitions that occur at high temperature exhibit small hysteresis characteristic of continuous polarization rotation.[76] Moreover, PMN-32PT at room temperature subject to compressive stress in [001] undergoes continuous polarization rotation from rhombohedral to either orthorhombic via monoclinic M_B or depolarized tetragonal via monoclinic M_A pathways.[75] The continuous polarization rotation suggests

that there are continuous rather than abrupt phase transitions.[75,76] In addition, compositions of PMN-xPT near the MPB can be in a multiphase state in which R, M, O, or T phases coexist.[75,76] Thus, an increase in the applied electric field will gradually increase the volume fraction of the new phase at the expense of the old phase, resulting in a continuous transition between phases that occurs over a range of electric fields.[96]

2.3 Olsen cycle

2.3.1 Introduction

Passive pyroelectric power generation does not take advantage of the large change in polarization that pyroelectric materials experience as a result of ferroelectric to paraelectric phase transition. This is due to the fact that poled pyroelectric materials lose their spontaneous polarization when heated above their Curie temperature and may not become repoled during subsequent cooling below the Curie temperature.[97] As a consequence, passive pyroelectric power generation suffers from low energy and power outputs. On the other hand, the Olsen cycle, described in Chapter 1, takes advantage of this temperature induced phase transition by applying an electric field during cooling to facilitate the material repoling. As a consequence, the Olsen cycle is able to generate a much larger electrical energy output.

2.3.2 Experimental implementation

Implementation of the Olsen cycle requires an electrical and a thermal subsystem. A simple thermal subsystem for performing Olsen cycle has been developed that consists of hot and cold isothermal dielectric oil baths.[23,26,30,33,34,52,97–99] The pyroelectric material is alternately submerged in the oil baths to create the temporal temperature oscillations required for the cycle. In addition, all Olsen cycle experiments make use of a similar electrical subsystem consisting of a modified Sawyer-Tower circuit to apply the required electric field and to measure charge Q collected on the sample electrodes.[61] Figure 2.7 shows this subsystem. In fact, this is the same electrical circuit that is widely used to collect D-E loops on dielectric

materials. The electrical subsystem serves two main purposes when performing the Olsen cycle, namely (i) to control the voltage applied to the pyroelectric element and impose V_L or V_H at appropriate times during the Olsen cycle (see Figure 1.2) and (ii) to determine the electrical energy generated by the pyroelectric element by measuring the voltage V_{PE} and charge Q_{PE} displayed by the pyroelectric element.

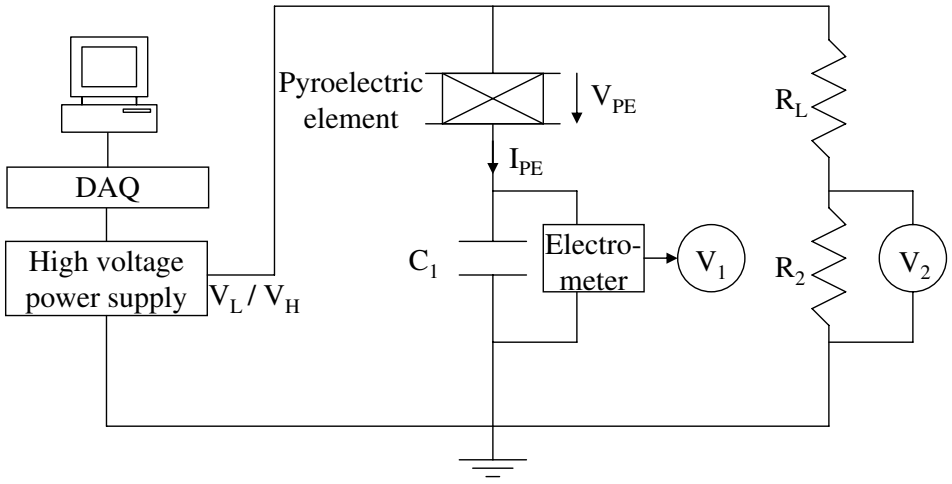

Figure 2.7: Electrical circuit used in experiments to perform the Olsen cycle and measure D-E loops.

The voltage V_1 across the capacitor C_1 is measured using an electrometer to minimize discharge of the capacitor connected to a data acquisition system (DAQ). Commonly, a resistive voltage divider (R_L and R_2 in Figure 2.7) is placed in parallel with the Sawyer-Tower bridge to scale down the voltage across the resistor R_2 so that it can be read by the low voltage DAQ. The electric field is applied by a computer generated function through the DAQ connected to a high voltage power supply. The magnitude of the electric displacement D of the PE is defined as

$$D = \frac{Q_{PE}}{A} = \frac{C_1 V_1}{A} \tag{2.10}$$

where A is the surface area of one electrode. The magnitude of the electric field across the

sample is calculated from Ohm's law and Kirchhoff's law and expressed as

$$E = \frac{V_{PE}}{b} = \frac{V_2(1 + R_L/R_2) - V_1}{b} \tag{2.11}$$

where b is the pyroelectric element thickness. Then, the D-E diagram can be generated.

2.3.3 Olsen cycle on selected pyroelectric materials

Two previous studies have investigated the energy generation capabilities of PZN-4.5PT undergoing the Olsen cycle using a thermal subsystem consisting of two isothermal dielectric oil baths.[33,34] Khodayari *et al.*[33] studied the energy harvesting capabilities of [110]-oriented PZN-4.5PT using the Olsen cycle. The authors achieved 216.5 J/L/cycle by successively dipping a 1 mm thick single crystal PZN-4.5PT sample in baths at 100^{o}C and 160^{o}C while the electric fields varied between E_L=0 MV/m and E_H=2 MV/m. Zhu *et al.*[34] also used 1.1 mm thick [110]-oriented PZN-4.5PT single crystals to examine the energy generated with electric field induced phase transitions through rhombohedral, orthorhombic, and tetragonal phases during the Olsen cycle. The authors obtained 101.8 J/L/cycle operating between temperatures 100 and 130^{o}C and electric fields E_L=0 MV/m and E_H=2 MV/m.[34] For these operating conditions, they determined that, during the isothermal processes 1-2 and 3-4 in the Olsen cycle, the samples experienced rhombohedral to orthorhombic (R-O) and orthorhombic to tetragonal (O-T) frequency-dependent phase transitions, respectively. Zhu *et al.*[34] also found that the energy density increased with reducing the duration of isothermal process 1-2 and increasing the duration of isothermal process 3-4 which varied from 0.1 to 100 seconds. Finally, if the isothermal processes were of equal duration, the energy density increased with increasing duration.[34] In both of these studies,[33,34] it is unclear if the experimental results were averaged over multiple cycles and/or were repeated for different samples. By contrast, the present study performs the Olsen cycle on several PZN-5.5PT single crystal samples and assesses the sample variability in terms of generated energy.

In addition, Kandilian *et al.*[97] used a similar thermal subsystem to study the pyroelectric energy generation of 140 μm thick [001]-oriented PMN-32PT single crystals using the Olsen

cycle. The maximum generated energy density was 100 J/L/cycle for electric field cycled between 0.2 and 0.9 MV/m and temperatures varying between 80 and 170^{o}C. In addition, T_{Curie} under zero-field was determined to be around 150^{o}C.[97] Moreover, the PMN-32PT samples experienced dielectric breakdown for electric fields larger than ∼0.9 MV/m, and suffered from cracking due to thermal stress for temperature differences in excess of 90^{o}C.[97]

2.3.4 Physical modeling

Recently, Kandilian *et al.*[97] derived a model estimating the energy harvesting capabilities of relaxor ferroelectric materials undergoing the Olsen cycle under quasi-equilibrium conditions, i.e., low frequency. The model assumes a linear relationship between electric displacement and electric field as in Equation (2.9). It expresses the energy density as[97]

$$\begin{aligned} N_D &= (E_H - E_L)\left[\frac{\varepsilon_0}{2}\left[\varepsilon_r(T_C) - \varepsilon_r(T_H)\right](E_H + E_L)\right] + \\ &\quad + (E_H - E_L)\left[P_s(T_C) - P_s(T_H) + \frac{d_{33}x_3}{s_{33}}\right] \end{aligned} \tag{2.12}$$

where $\varepsilon_r(T_C)$ and $\varepsilon_r(T_H)$ are the low-frequency ($\sim$ 0.1 Hz) large-field dielectric constants of the pyroelectric material at the cold and hot source temperatures T_C and T_H, respectively. Similarly, $P_s(T_C)$ and $P_s(T_H)$ are the saturation polarizations at the respective temperatures and are expressed in C/m^2.[64] The last term on the right-hand side of Equation (2.12) represents the contribution of the secondary pyroelectric coefficient to the generated energy density due to dimensional changes in the crystal structure caused by temperature changes. Here, d_{33} is the piezoelectric coefficient of the single crystal (in C/N) and s_{33} its elastic compliance (in m^2/N). The strain resulting from temperature change from T_C to T is defined as $x_3 = \int_{T_C}^{T} \alpha(T)\,\mathrm{d}T$ where $\alpha(T)$ is the thermal expansion coefficient in the direction of the applied electric field (in K^{-1}).[100] This model was validated against experimental data collected on PMN-32PT single crystal samples[97] using $\varepsilon_r(T)$ and $P_s(T)$ reported in the literature.[66] The authors observed that the Olsen cycle exceeded the bounds of the isothermal D-E loops at the silicone oil bath temperatures T_C and T_H. They attributed this to the secondary pyroelectric effect occurring during the heating process 3-4 featuring a rhombohedral

to tetragonal phase transition. Equation (2.12) was also validated with lanthanum-doped zirconate titanate (8/65/35 PLZT) ceramics.[98] But then, the thermal expansion term was ignored because the Olsen cycle fell within the bounds of the isothermal D-E loops at T_C and T_H. Here also, the model predictions are compared with the energy density experimentally measured with PZN-5.5PT[52] and PMN-28PT.[100]

2.3.5 Maximizing energy conversion

The Olsen cycle depicted in Figure 1.2 illustrates that (i) increasing the change in electric displacement as the material temperature goes between T_{hot} and T_{cold} and/or (ii) increasing the electric field span (E_H - E_L) results in larger energy generated. In order to maximize the energy density N_D generated, the electric field span (E_H - E_L) should be as large as possible without causing electric breakdown and/or depoling.[98] To achieve this, (i) the pyroelectric material should possess a large electric breakdown field E_{br} and (ii) E_L should be above the electric field required for poling at T_{cold}. The electric field required for poling is slightly larger than the coercive electric field E_c.[74] Similarly, the change in electric displacement as the material heats and cools should be the largest possible. To maximize the change in D, T_{hot} should be slightly greater than the Curie temperature T_{Curie} at E_H. In addition, T_{cold} should be chosen so that the material exhibits the largest electric displacement in the range E_L to E_H.

2.4 Summary

This chapter introduced the different classifications of dielectric materials. It reviewed the features of ferroelectric, pyroelectric, and piezoelectric materials and how their polarization is affected by the applied temperature, stress, and electric field. In addition, the large change in polarization associated with ferroelectric to paraelectric phase transition was discussed. The Olsen cycle takes advantage of this phase transition by heating a ferroelectric material past its Curie temperature and is able to achieve much larger electrical energy output than its

passive pyroelectric conversion counterpart. In addition, the behavior of relaxor ferroelectric single crystal PZN-PT and PMN-PT under varying temperature, stress, and electric field conditions was presented.

The discussion and results presented in the following chapters will focus on improving the electrical power output of the Olsen cycle performed on PZN-PT and PMN-PT. In addition, the study will explore new energy conversion cycles that convert mechanical and thermomechanical energy into electrical energy by taking advantage of phase transitions and the piezoelectric response of these materials.

CHAPTER 3

Waste Heat Energy Harvesting Using Olsen Cycle on PZN-5.5PT Single Crystals

This chapter presents an experimental study of the Olsen cycle performed on PZN-5.5PT single crystals. It reports the electrical energy and power densities generated by PZN-5.5PT under various operating conditions. It contributes to the exploration of new materials for improving our understanding and the performance of the Olsen cycle.

3.1 Introduction

PZN-xPT single crystal is a promising material for low-grade waste heat energy harvesting thanks to its large polarization and small Curie temperature (T_{Curie}<200^{o}C). In fact, in the temperature range 130 to 165^{o}C at zero-field, PZN-4.5PT spans the highly polarized tetragonal and depolarized cubic phases.[33] Previous studies performing the Olsen cycle on [110] PZN-4.5PT single crystals[33,34] were presented in Chapter 2 Section 2.3.3. The material demonstrated relatively large energy densities compared to other single crystals. However, the thermal energy conversion ability of closely related [001] PZN-5.5PT has not been previously explored. Thus, the present chapter aims (i) to assess the performance of PZN-5.5PT single crystals undergoing the Olsen cycle, (ii) to measure the large-field dielectric properties of the material, and (iii) to further validate the physical model[97] discussed in Chapter 2 Section 2.3.4 predicting the energy density generated by the cycle.

3.2 Experiments

Samples

In the present study, five single crystal PZN-5.5PT samples were purchased from Microfine Materials Technologies PTE Ltd, Singapore. The samples were poled in the [001]-direction. Their cross-sectional area and thickness were 1×1 cm^2 and 200 μm, respectively. Each 1×1 cm^2 face of the samples was coated with a $\sim$10 nm NiCr bond layer and a $\sim$1 μm thick $Au_{0.68}Pd_{0.32}$ electrode. These layers were deposited by RF sputter-deposition technique. Electrical wires were attached to the electrodes using conductive silver epoxy.

D-E loops

Isothermal bipolar displacement versus electric field hysteresis curves were collected at various temperatures by applying a triangular voltage with frequency of 0.1 Hz across the single crystal samples. The samples were placed in a silicone oil bath at the desired temperatures of 100, 125, 150, 175 or 190^{o}C. The amplitude of the voltage corresponded to an electric field varying from -1 to 1 MV/m. All measurements were repeated five times on each of the five different samples to assess repeatability and experimental uncertainty.

Moreover, the saturation polarization $P_s(T)$ and the large-field dielectric constant $\varepsilon_r(T)$ of each sample at temperature T were evaluated by linearly fitting the section of the bipolar D-E loops corresponding to relatively large electric field decreasing from 1 to 0.5 MV/m according to Equation (2.9).

Finally, isothermal unipolar D-E loops were collected on Sample 5 for the same above temperatures. They were compared with bipolar D-E loops along with the associated values of $\varepsilon_r(T)$ and $P_s(T)$.

Olsen cycle

The Olsen cycle was performed on the PZN-5.5PT samples for (i) different values of low and high electric fields E_L and E_H, (ii) various hot source temperature T_H, and (iii) various cycle frequency f. The experimental setup consisted of a thermal and an electrical subsystem. The experimental apparatus and procedure were identical to those that were introduced in Chapter 2 Section 2.3.2 and used in our previous studies[97,101] and need not be repeated. The cold source temperature T_C was fixed at 100^{o}C. The hot source temperature was varied from 125 to 190^{o}C. The electric fields E_L and E_H ranged from 0 to 0.2 MV/m and from 0.5 to 1.5 MV/m, respectively. The overall cycle frequency varied from 0.021 to 0.15 Hz by changing the duration of the isoelectric field heating and cooling processes 2-3 and 4-1 denoted by τ_{23} and τ_{41} (Figure 1.2). However, the time rate of change of the electric field during the isothermal processes 1-2 and 3-4 remained the same at 0.4 MV/m/s. Note that this rate was identical to that used to collect the D-E loops between -1 and 1.0 MV/m at 0.1 Hz. In other words, τ_{12} and τ_{34} were equal and constant for a given electric field span. For example τ_{12}=τ_{34}=2.5 s for E_H-E_L=1 MV/m. The times τ_{23} and τ_{41} varied between 0.5 and 20 s corresponding to cycle frequency varying from 0.15 to 0.021 Hz. The energy density was calculated by numerical integration of Equation (1.1) using the trapezoidal rule.

3.3 Results and discussion

3.3.1 D-E loops

Figure 3.1 shows typical isothermal bipolar D-E loops at T_C=100^{o}C as well as loops for T_H equal to (a) 125^{o}C, (b) 150^{o}C, (c) 175^{o}C, and (d) 190^{o}C obtained with Sample 5. The isothermal D-E loops followed a counter-clockwise path. Figure 3.1 also shows the Olsen cycles corresponding to the above temperatures with E_L=0.0 or 0.2 MV/m and E_H=1.0 MV/m. Results indicated that all [001] PZN-5.5PT samples were ferroelectric at 100, 125, and 150^{o}C. They were paraelectric at 190^{o}C as their saturation polarization vanished (Figure 3.1d). In addition, Samples 1 and 2 were paraelectric at 175^{o}C while Samples 3, 4, and 5

were ferroelectric at 175^{o}C.

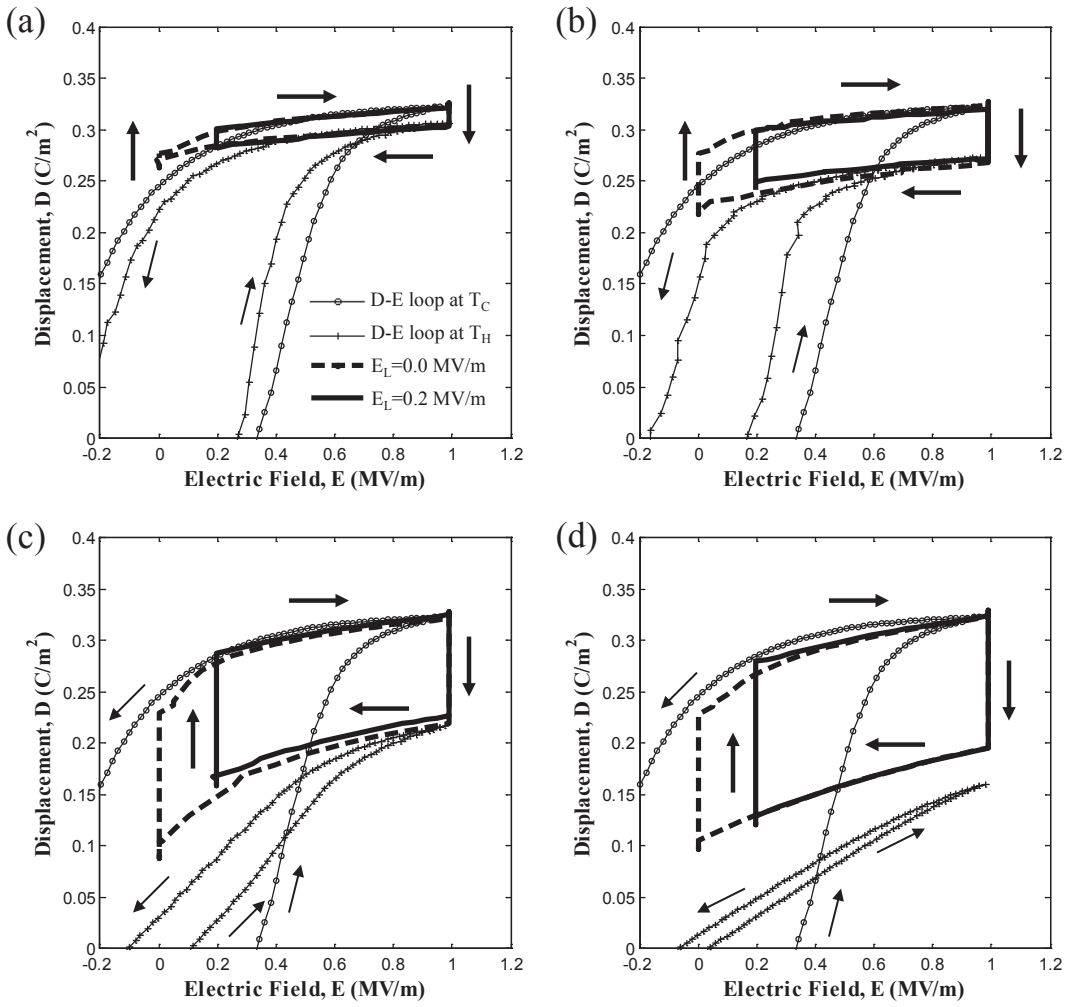

Figure 3.1: Isothermal bipolar D-E loops and experimental Olsen cycles at E_L=0.0 and 0.2 MV/m for PZN-5.5PT (Sample 5) with T_C=100^{o}C and E_H=1.0 MV/m for T_H equal to (a) 125^{o}C, (b) 150^{o}C, (c) 175^{o}C, and (d) 190^{o}C.

Moreover, Table 3.1 summarizes the values of $P_s(T)$ and $\varepsilon_r(T)$ retrieved from the isothermal D-E loops for each sample at different temperatures. The greatest inter-sample variability in D-E loops and in the resulting $P_s(T)$ and $\varepsilon_r(T)$ values was observed at 125 and 175^{o}C.

The relative errors in $P_s(T)$ and $\varepsilon_r(T)$ among samples were less than 20% for temperatures 100, 150, and 190^{o}C. They were less than 25% and 30% for temperatures 125 and 175^{o}C, respectively. The variability at 125^{o}C can be attributed to the presence of mixed rhombohedral and tetragonal phases. In fact, the volume ratio of these phases may vary from one sample to another due to small chemical inhomogeneities.[102] The sample variability observed at 175^{o}C can be attributed to the fact that Samples 3, 4, and 5 were ferroelectric with $P_s \approx$0.13 C/m^2 while Samples 1 and 2 were paraelectric at this temperature.

Table 3.1: Saturation polarization $P_s(T)$ and large-field dielectric constant $\varepsilon_r(T)$ for the five [001] PZN-5.5PT samples used in this study.

Sample	**Properties**	**Units**					
	T	(^{o}C)	100	125	150	175	190
1	$P_s(T)$	(C/m^2)	0.233	0.221	0.2049	0.0593	-
	$\varepsilon_r(T)$	-	2535	4327	4833	16684	-
2	$P_s(T)$	(C/m^2)	0.2554	0.2569	0.2322	0.0959	0.034
	$\varepsilon_r(T)$	-	2937	3445	4352	13889	12781
3	$P_s(T)$	(C/m^2)	0.2078	0.2110	0.2222	0.1346	0.0529
	$\varepsilon_r(T)$	-	3617	5620	5136	10015	13598
4	$P_s(T)$	(C/m^2)	0.2922	0.2801	0.2458	0.1308	0.0451
	$\varepsilon_r(T)$	-	3500	3471	3840	10448	14364
5	$P_s(T)$	(C/m^2)	0.2967	0.2814	0.2397	0.1266	0.0384
	$\varepsilon_r(T)$	-	3180	3180	4100	11100	14500

Finally, Figure 3.2 compares unipolar and bipolar D-E loops performed on Sample 5 at 100^{o}C. The unipolar D-E loop, corresponding to a frequency of 0.2 Hz, had the same time rate of change in the electric field as the bipolar D-E loop measured at 0.1 Hz. Note also that the unipolar D-E loops measured at 0.1 and 0.2 Hz were nearly identical. A notable difference between the unipolar and bipolar D-E loops at 100^{o}C was the absence of a field-induced phase transition in the unipolar loops. Such a phase transition was responsible for the non-

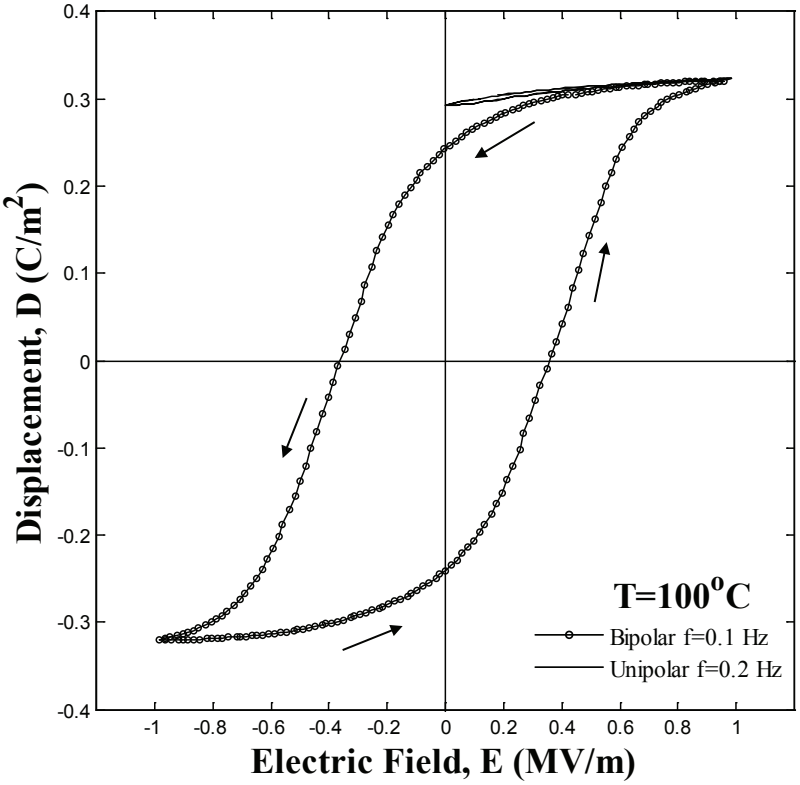

Figure 3.2: Isothermal bipolar D-E loops at 0.1 Hz and unipolar D-E loops at 0.2 Hz for PZN-5.5PT (Sample 5) at T=100^{o}C.

linear behavior of the bipolar D-E loops at low electric field. By contrast, the unipolar D-E loops followed a nearly linear path between 0.0 and 1.0 MV/m. Figure 3.2 establishes that the unipolar D-E loops followed the upper curve of the bipolar D-E loop corresponding to a decreasing electric field. Thus, analysis of the unipolar D-E loops or the upper curve of bipolar D-E loops resulted in nearly identical values of saturation polarization $P_s(T)$ and dielectric permittivity $\varepsilon_0\varepsilon_r(T)$. The same conclusions were reached at other temperatures (not shown). Finally, the D-E loops were closed for all temperatures indicating that there was no leakage current.

3.3.2 Effect of frequency on N_D and P_D

Figure 3.3 shows the isothermal bipolar D-E loops at temperatures 100 and 190^{o}C for Sample 4. It also depicts the experimental Olsen cycle in the D-E diagram for Sample 4 at various cycle frequencies between 0.021 and 0.15 HZ. The cycle followed a clockwise path and was performed between T_C=100^{o}C and T_H=190^{o}C and electric field from E_L=0 MV/m to E_H=1.0 MV/m. Note also that all the experimental Olsen cycles were closed and, unlike P(VDF-TrFE),[101] no leakage current was observed.

First, it is interesting to note that the Olsen cycles measured at frequencies of 0.021 Hz and 0.034 Hz overlapped. Indeed, for these frequencies, the electric displacement had reached steady-state, i.e., $\partial D/\partial t = 0$, before the electric field was varied. In this case, processes 1-2 and 3-4 followed a relatively smooth path, indicating that the four different processes in the Olsen cycle were performed under quasiequilibrium conditions.

Moreoever, for cycle frequencies larger than 0.034 Hz, the isoelectric field processes 2-3 and 4-1 were not performed under quasiequilibrium conditions. For such cycle frequencies, the electric displacement had not reached steady-state before the electric field was varied to perform processes 1-2 and 3-4. In other words, the phase transition was incomplete. In addition, the Olsen cycles did not follow a smooth path between E_L and E_H during processes 1-2 and 3-4 in the D-E diagram, as illustrated in Figure 3.3.

Figures 3.4a and 3.4b respectively show the energy density and power density as functions of frequency for the Olsen cycles performed on Sample 4 and reported in Figure 3.3. Each data point corresponds to the energy density or power density averaged over five cycles. The associated error bars correspond to two standard deviations or a 95% confidence interval. The energy density reached a plateau of 140 J/L/cycle at frequencies below 0.034 Hz and decreased with increasing cycle frequency. Reducing the cycle frequency below 0.034 Hz, by increasing the duration of the isoelectric field processes 2-3 and 4-1, did not result in larger energy density because each process of the Olsen cycle was in quasiequilibrium.

Conversely, the power density increased with increasing frequency and reached a maxi-

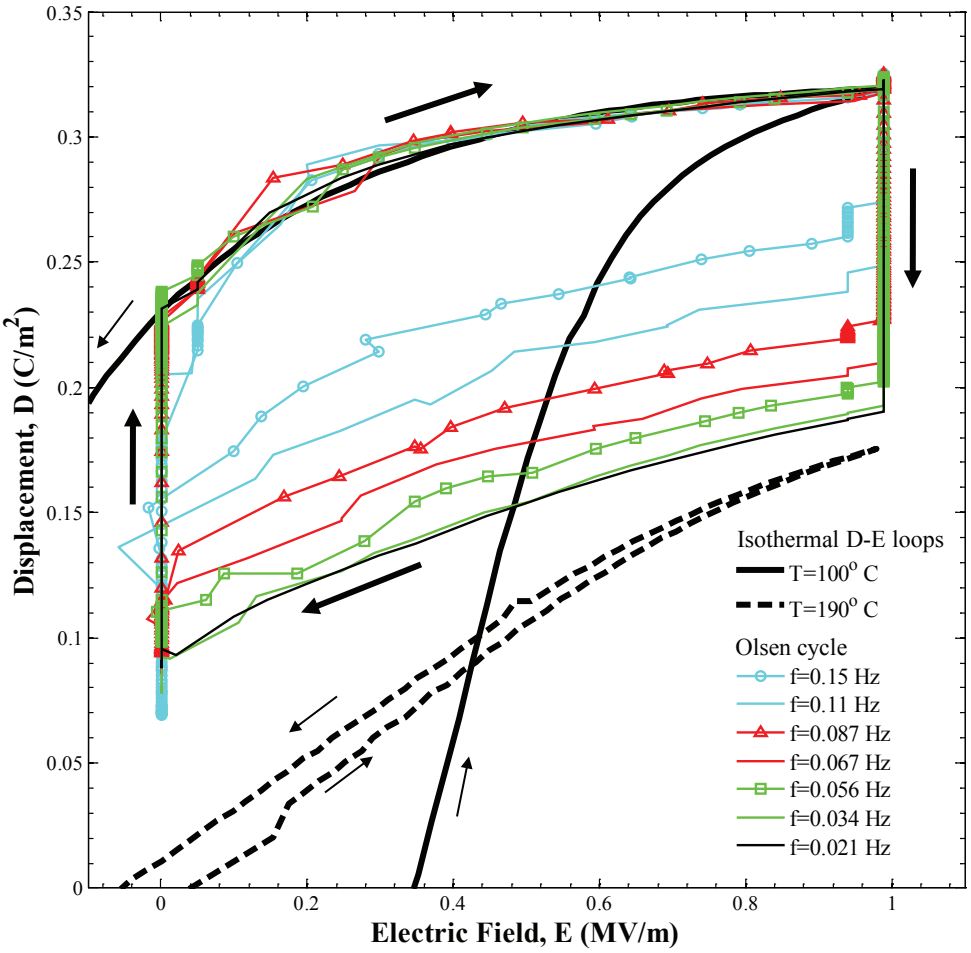

Figure 3.3: D-E diagram of isothermal bipolar D-E loops and experimental Olsen cycles at various frequencies for PZN-5.5PT (Sample 4). The temperatures T_C and T_H were maintained at 100 and 190^{o}C, respectively and the low and high electric fields E_L and E_H were set at 0.0 and 1.0 MV/m, respectively.

mum of 10.1 W/L at 0.1 Hz. For frequencies larger than 0.1 Hz, P_D decreased with increasing frequency. This can be explained by considering the expression $P_D = N_D(f)f$. For frequencies less than 0.1 Hz, the decrease in $N_D(f)$, previously discussed, was compensated by the raise in frequency so that P_D increased. However, beyond 0.1 Hz, N_D decreased significantly with frequency resulting in smaller values of P_D. In practice, the operating frequency could be adjusted according to the power needed for a given load. Note that the frequency of 0.15

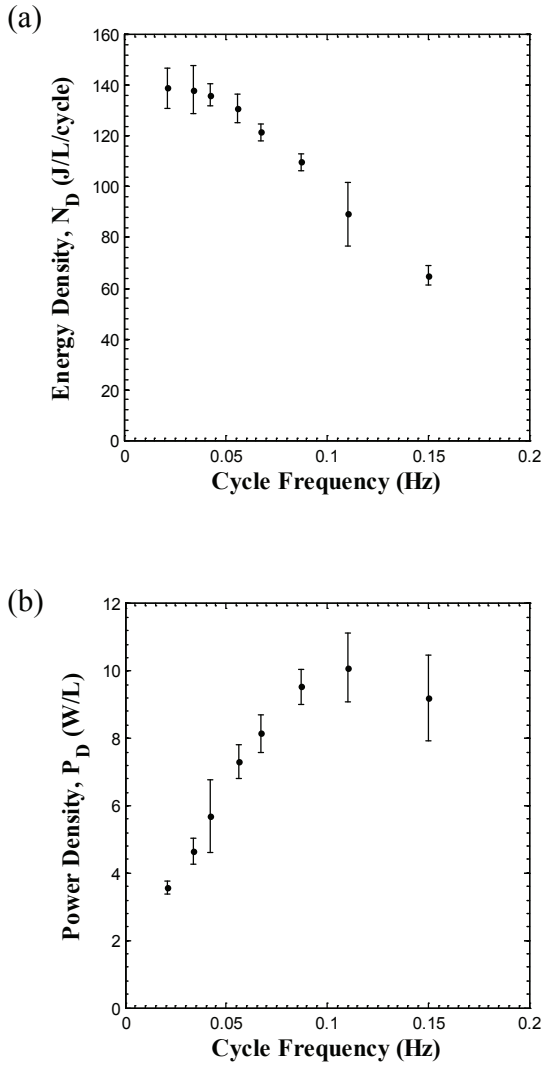

Figure 3.4: Experimentally measured (a) energy density and (b) power density generated with PZN-5.5PT single crystal (Sample 4) as a function of cycle frequency. The temperatures T_C and T_H were maintained at 100 and 190^{o}C, respectively. The low and high electric fields E_L and E_H were set at 0.0 and 1.0 MV/m, respectively.

Hz corresponded to τ_{23}=τ_{41}=0.5 s while the time required to physically transfer the sample between the hot and cold baths was ∼0.25 s per transfer.

Furthermore, the Biot number for the pyroelectric assembly (film with electrodes) is defined as $Bi = hb/k_{eff}$ where h is the heat transfer coefficient, b and k_{eff} are the sample thickness and effective thermal conductivity, respectively. The heat transfer coefficient h=300 W/m^2·K corresponded to convective quenching in an oil bath.[103] The effective thermal conductivity of the assembly was estimated using the series model. The thermal conductivity of PZN-5.5PT could not be found in the literature and was approximated to be that of PZT, i.e., $k \simeq$1.2 W/m·K at room temperature[104] while that of gold was k=310 W/m·K.[105] Thus, the effective thermal conductivity of the assembly of thickness b=202 μm was $k_{eff} \simeq$ 1.21 W/m·K resulting in $Bi \simeq 0.05$ or $Bi \ll 1$. Therefore, the temperature was uniform across the sample and the lumped capacitance approximation was valid for all conditions considered.[105]

Finally, the thermal time constant τ_t associated with processes 2-3 and 3-4 can be estimated as $\tau_t = \rho_{eff} c_{p,eff} b/h$[105] where ρ_{eff} and $c_{p,eff}$ are the effective density and specific heat of the pyroelectric assembly, respectively. The thermal time constant was estimated to be 1.68 s for a 200 μm thick PZN-5.5PT film with ρ=8,000 kg/m^3[106] and c_p= 312.5 J/kg·K[107] sandwiched between two 1 μm thick $Au_{0.68}Pd_{0.32}$ electrodes having ρ=16,951 kg/m^3[108] and specific heat c_p=156.8 J/kg·K. This time constant indicates that for cycle frequencies above 0.065 Hz the sample may have not reached thermal equilibrium during processes 2-3 and 4-1 of the Olsen cycle.

3.3.3 Sample variability at peak power

For practical purposes and for validating the model, it is important to assess sample variability. Figure 3.5 shows the power density generated experimentally as a function of high electric field E_H at cycle frequency of 0.1 Hz for four different samples. Here also, each data point corresponds to the power density averaged over five cycles and the associated

error bars correspond to two standard deviations. In these cycles, T_C and E_L were set to be 100^{o}C and 0.2 MV/m, respectively. The temperature T_H varied from 125 to 190^{o}C while E_H ranged from 0.5 to 1.5 MV/m. Figure 3.5 demonstrates that, for all samples, the power density increases with increasing electric field E_H and with hot source temperature T_H. The maximum power obtained was 11.7 W/L for T_C=100^{o}C, T_H=190^{o}C, E_L=0.2 MV/m, and E_H=1.5 MV/m. Increasing the electric field E_H beyond 1.5 MV/m during the Olsen cycle led to sample failure caused by thermo-electro-mechanical stress.

Furthermore, the maximum relative error in P_D among samples for all values of E_H was 18.3% for T_H=125^{o}C. It decreased to 18.0%, 9.8%, and 6.5% as T_H increased from 150, 175, to 190^{o}C, respectively. The larger variability observed at lower temperature can be attributed to the large differences in the rhombohedral and tetragonal volume fractions among samples. This was already observed in the bipolar D-E loops and in the retrieved properties $P_s(T)$ and $\varepsilon_r(T)$. On the other hand, the value of E_H was found to have no significant effect on sample variability.

3.3.4 Energy density under quasiequilibrium conditions

Figures 3.6 and 3.7 show the energy density N_D as a function of electric field E_H for Sample 5 with low electric field E_L equal to 0.0 and 0.2 MV/m, respectively. In all cases, the temperature T_C was 100^{o}C while T_H was (a) 125, (b) 150, (c) 175, and (d) 190^{o}C. The cycle frequency was 0.034 Hz corresponding to Olsen cycles with quasiequilibrium processes, as previously discussed. Results for E_H=1.0 MV/m correspond to the Olsen cycles shown in Figure 3.1 for each value of T_H.

Figures 3.6 and 3.7 indicate that the energy density increased with increasing values of T_H and E_H. They demonstrate that operating the cycle with T_H above T_{Curie}=165^{o}C yields significantly higher energy densities than cycles operating below T_{Curie}. In fact, a maximum energy density of 150 J/L/cycle was achieved for operating temperatures between T_C=100^{o}C and T_H=190^{o}C and electric fields E_L and E_H equal to 0.0 and 1.2 MV/m, respectively.

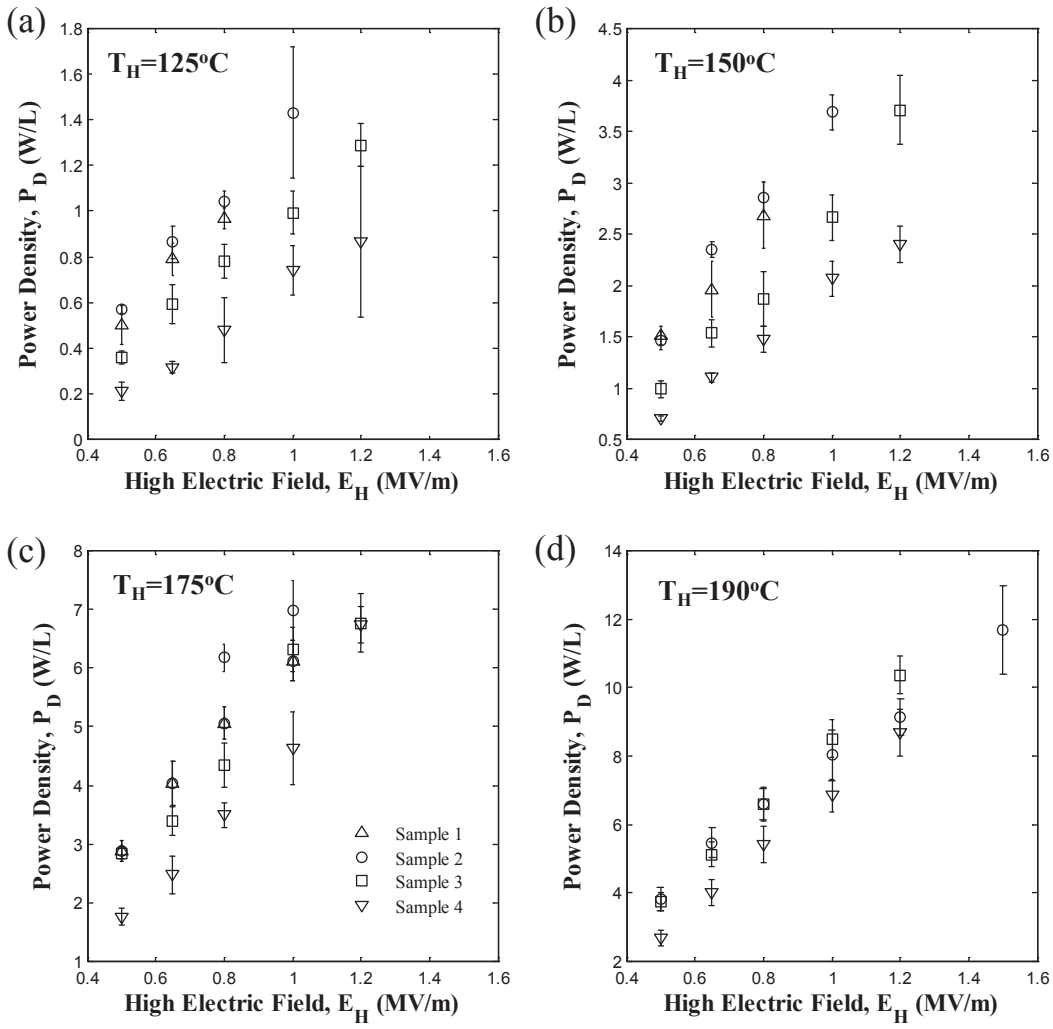

Figure 3.5: Experimentally measured power density generated at 0.1 Hz from 4 different samples of PZN-5.5PT single crystal as a function of high electric field E_H for T_H equal to (a) 125^{o}C, (b) 150^{o}C, (c) 175^{o}C, and (d) 190^{o}C. The temperature T_C was maintained at 100^{o}C and the low electric field E_L was set at 0.2 MV/m.

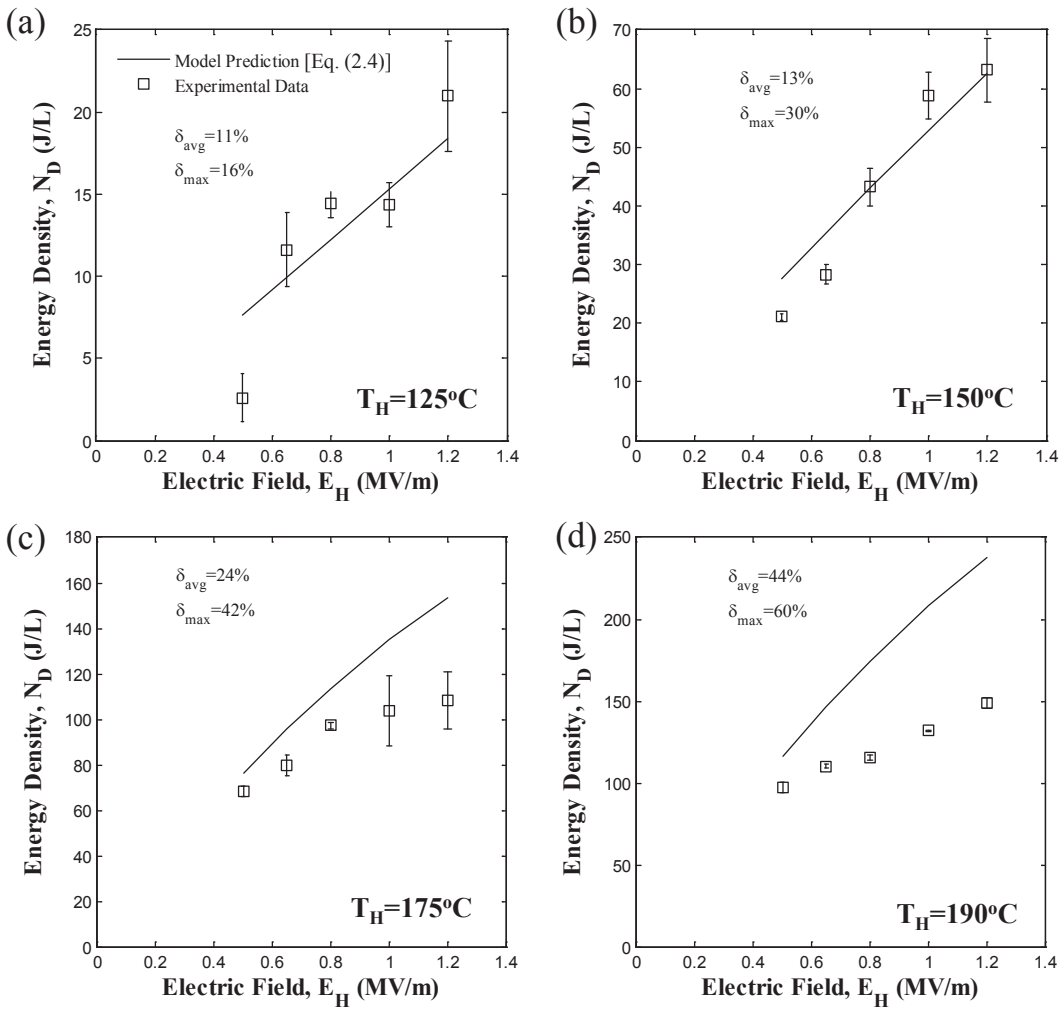

Figure 3.6: Experimentally measured energy density generated at 0.034 Hz from PZN-5.5PT single crystal (Sample 5) versus high electric field E_H for T_H equal to (a) 125^{o}C, (b) 150^{o}C, (c) 175^{o}C, and (d) 190^{o}C. The temperature T_C was maintained at 100^{o}C and the low electric field E_L was set at 0.0 MV/m. The solid line corresponds to predictions by Equation (2.12) using properties retrieved from isothermal D-E loops (Table 3.1).

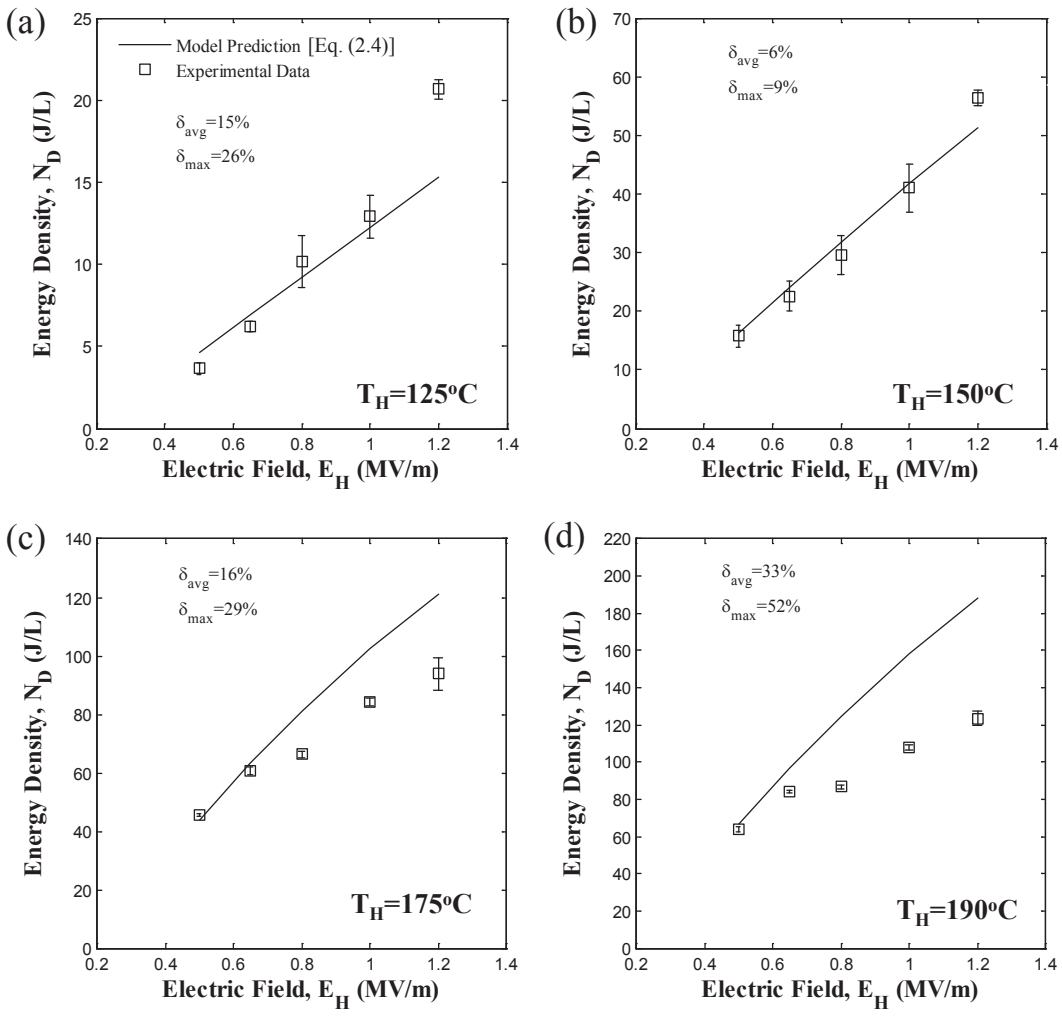

Figure 3.7: Experimentally measured energy density generated at 0.034 Hz from PZN-5.5PT single crystal (Sample 5) versus high electric field E_H for T_H equal to (a) 125^{o}C, (b) 150^{o}C, (c) 175^{o}C, and (d) 190^{o}C. The temperature T_C was maintained at 100^{o}C and the low electric field E_L was set at 0.2 MV/m. The solid line corresponds to predictions by Equation (2.12) using properties retrieved from isothermal D-E loops (Table 3.1).

In addition, increasing E_L resulted in a decrease in the generated energy density. For example, the maximum energy density decreased from 150 to 124 J/L/cycle as E_L increased from 0.0 to 0.2 MV/m for the same T_C=100^{o}C, T_H=190^{o}C, and E_H=1.2 MV/m. This indicates that the PZN-5.5PT sample did not become depoled when lowering the applied electric field to 0.0 MV/m, unlike observations made with PMN-32PT.[97] Since PZN-5.5PT retains its polarization at zero electric field, the isoelectric field cooling process 4-1 can be performed at E_L=0 MV/m which may simplify the practical implementation of the Olsen cycle.

Moreover, it is interesting to compare the maximum energy density of 150 J/L/cycle obtained with PZN-5.5PT with 100 J/L/cycle obtained with PMN-32PT for the same temperature difference (90^{o}C) and for E_L and E_H equal to 0.2 and 0.9 MV/m, respectively. However, note that T_C and T_H were 80 and 170^{o}C for PMN-32PT[97] instead of 100 and 190^{o}C for PZN-5.5PT. This suggests that these two materials should be operated in slightly different temperature ranges for optimum performance. This could be useful in a multistage pyroelectric converter as envisioned by Olsen *et al.*[24] Another material that could be included in the same multistage device is [110]-oriented PZN-4.5PT whose Curie temperature is around 157^{o}C[83] compared with 150^{o}C and 165^{o}C for PMN-32PT and PZN-5.5PT, respectively.

Finally, Khodayari *et al.*[33] obtained 216.5 J/L with PZN-4.5PT single crystal samples with operating conditions T_C, T_H, E_L, and E_H equal to 100^{o}C, 160^{o}C, 0.0 MV/m, and 2.0 MV/m, respectively. The larger energy density obtained for PZN-4.5PT can be attributed to the larger electric field span ($E_H - E_L$) and to the lower Curie temperature. Indeed, the lower Curie temperature of PZN-4.5PT allowed for the tetragonal to cubic phase transition to occur for smaller temperature swing but with the same value of T_C. This resulted in reduced thermal stress on the samples. It may also be why the PZN-4.5PT samples were able to withstand electric field as high as 2.0 MV/m without sample failure[33,34] compared with up to 1.5 MV/m in the present study.

3.3.5 Model predictions

Figures 3.6 and 3.7 also compare experimental energy density generated by Sample 5 with predictions of the model given by Equation (2.12). The saturation polarization and dielectric constant of Sample 5 at T_C and T_H retrieved from D-E loops are given in Table 3.1. Here, the last term of Equation (2.12), corresponding to the contribution of thermal expansion to the energy density, was ignored. Indeed, the Olsen cycles performed on PZN-5.5PT fell on or within the bounds of the isothermal D-E loops at T_C and T_H (Figure 3.1), indicating that thermal expansion did not contribute to the generated energy.

Figures 3.6 and 3.7 also report the average and maximum relative error between experimental data and model predictions denoted by δ_{avg} and δ_{max}, respectively. Relatively good agreement was observed between model predictions and experimental data, particularly for temperature T_H less than 175^{o}C and E_L=0.2 MV/m. Then, the average relative error was less than 24%. Both the average and maximum relative errors were larger for E_L=0.0 MV/m than for E_L=0.2 MV/m for any given temperature T_H. This can be explained by considering the isothermal D-E loops shown in Figures 3.1 and 3.2. For low electric fields (E <0.2 MV/m) and for temperatures below T_{Curie}=165^{o}C, the material is ferroelectric, and the electric displacement is a non-linear function of electric field. This non-linearity was also observed by Zhu *et al.*[34] for [110]-oriented PZN-4.5PT and was attributed to electric-field induced phase transitions. This phenomenon was not accounted for by the above model which treated $\varepsilon_r(T)$ as a function of temperature only.[97] However, $\varepsilon_r(T)$ could be assumed to depend only on T for electric field larger than 0.2 MV/m as previously discussed.

Moreover, Figures 3.6d and 3.7d indicate that the average difference between experimental and model predictions reached 44 and 33% for E_L=0.0 and 0.2 MV/m at T_H=190^{o}C, respectively. For such large value of T_H, the model systematically overpredicted the experimental data. For T_H=175^{o}C, the discrepancies can be attributed to the fact that the quasiequilibrium Olsen cycles did not follow the isothermal D-E loop as the electric field was reduced from 1 to 0 MV/m (Process 3-4) as illustrated in Figure 3.1c. This suggests

that the sample did not undergo the same phase transition during the isothermal D-E loops and the Olsen cycle. However, for T_H=190^{o}C process 2-3 of the Olsen cycles did not span the same electric displacement as the isothermal D-E loop as illustrated in Figure 3.1d. An electric displacement extending beyond the bounds of the D-E loops was attributed to positive thermal expansion by Kandilian *et al.*[97] Conversely, the reduced electric displacement span can be attributed to negative thermal expansion. The lattice parameters of PZN-5.5PT were reported to be constant between 190 and 100^{o}C[81] indicating zero thermal expansion, whereas the thermal expansion coefficient of $Au_{0.75}Pd_{0.25}$ was reported to be 12 μm/m·K.[108] The mismatch in thermal expansion coefficients between the electrode and the PZN-5.5PT sample induced a tensile stress in the material, which may have resulted in a decrease in sample thickness. This phenomenon was not observed for T_H=125 and 150^{o}C as is evident in Figures 3.1a and 3.1b where the Olsen cycles tended to follow the path of the unipolar D-E loops measured at T_H. Then, good agreement was observed between model predictions and experimental data.

3.3.6 Sample durability

The samples used in this study broke after 100 to 250 cycles. The successive thermal stress in combination with the electrically induced strains contributed to the samples eventually cracking and breaking. This explains why data were not reported for all samples under all conditions (Figure 3.5). Strategies to increase the sample durability include (i) pre-stressing the sample such as in thin layer unimorph ferroelectric driver and sensor actuators[109] and (ii) applying a conformal coating (e.g., Parylene HT) to the sample.[55]

3.4 Chapter summary

This chapter presented experimental measurements of energy and power densities generated by performing the Olsen cycle on [001]-poled PZN-5.5PT single crystals. It showed that as the cycle frequency increased, the energy density decreased while the power density increased

up to 0.1 Hz when it reached a maximum. For cold and hot source temperatures T_C=100^{o}C and T_H=190^{o}C and electric fields between 0.2 and 1.5 MV/m the power densities reached a maximum of 11.7 W/L at 0.1 Hz. The maximum energy density achieved was 150 J/L at frequency 0.034 Hz for T_C=100^{o}C, T_H=190^{o}C, E_L=0.0 MV/m, and E_H=1.2 MV/m. Sample variability was relatively small. It was the largest around 125^{o}C due to variation in the rhombohedral/tetragonal volume fraction among samples and around 175^{o}C due to difference in Curie temperature. Moreover, the large-field dielectric constant and saturation polarization of PZN-5.5PT are presented in Table 3.1 for temperatures between 100 and 190^{o}C at 0.1 Hz. Finally, the results confirmed the validity of a recently developed model[97] given by Equation (2.12) predicting the energy density generated from ferroelectric single crystals using the Olsen cycle under quasiequilibrium conditions.

CHAPTER 4

PMN-28PT Crystals: Thermal Properties and Bipolar Dielectric Characterization for Varying Temperature and Uniaxial Stress

This chapter presents the dielectric and thermophysical properties as well as the phase diagram of [001]-poled PMN-28PT single crystals over a wide range of compressive stress and temperature. These properties will be useful for determining the operating conditions of the Olsen cycle in order improve its performance. The results will also be useful in subsequent chapters when PMN-28PT is used in thermomechanical energy conversion cycles.

4.1 Introduction

Ferroelectric materials have been used in various transducer applications including energy harvesters, sensors, and actuators. Many of these applications rely on the fact that the dielectric response of ferroelectric materials can vary drastically with varying temperature and/or stress. For example, mechanical and thermal energy harvesting applications using ferroelectric materials rely on changes in polarization to generate electricity in response to applied mechanical stress[110] or temperature.[37] In addition, power cycles based on alternatingly varying the applied electric field and temperature and/or stress can be used to generate electricity.[20,111,112] Moreover, pyroelectric and piezoelectric sensors take advantage of the change in polarization of the material due to very small changes in temperature or stress, respectively.[61] Furthermore, ferroelectric memory relies on polarization switching due to an applied field. The electric field required for switching is affected by the temperature

and stress state of the material.[61] In all of these applications, it is important to understand and predict the dielectric behavior of the ferroelectric material for varying temperature and compressive stress. The material performance is affected by phase transitions occurring as a result of change in electric field and/or temperature and/or stress conditions. Thus, knowing the phases of a material for varying temperature, stress, and electric field is also critical.

Due to its extraordinarily large piezoelectric response near the MPB,[87] ferroelectric PMN-xPT has been widely used in mechanical sensors and actuators and their piezoelectric and dielectric properties have been studied extensively.[66,74–76,87,88,92,113–119] However, to the best of our knowledge, the dielectric response of [001]-poled PMN-28PT for varying temperature and [001] compressive stress has never been investigated. Thus, this chapter presents experimental measurements of bipolar hysteresis loops performed on [001]-poled PMN-28PT single crystals under uniaxial compressive stress in the [001] direction ranging from 0 to 25.13 MPa and temperature ranging from 22 to 170^{o}C. This chapter aims to provide information useful for evaluating [001] PMN-28PT in many applications. The presented information includes (i) the dielectric properties as a function of temperature and stress, (ii) an assessment of extending a previously developed model to include stress dependence, (iii) an electric field-temperature- compressive stress phase transition map, and (iv) the thermal properties including the phase change enthalpy as well as the thermal expansion coefficient and specific heat as a function of temperature. Note that some of the properties presented in this chapter are used in later chapters for conducting analysis of the energy harvesting performance of PMN-28PT.

4.2 Background

Dielectric properties

Herklotz *et al.*[74] reported the remnant polarization P_r and coercive field E_c of [001]-poled PMN-28PT under zero-stress as a function of temperature between -75 and 130^{o}C. The remnant polarization P_r decreased with increasing temperature up to 49^{o}C. It then increased

up to 63^{o}C when the material underwent a monoclinic M_A to M_C phase transition.[74] Between 63 and 72^{o}C, P_r decreased and then increased between 72 and 82^{o}C where it reached a maximum as the material transitioned into the tetragonal phase.[74] For temperature above 82^{o}C, P_r decreased with increasing temperature as the material relaxed into the paraelectric cubic phase.[74] Similarly, the coercive electric field E_c decreased with increasing temperature up to 70^{o}C.[74] Between 70 and 82^{o}C it increased slightly and then decreased with increasing temperature beyond 82^{o}C as the material relaxed.[74]

The remnant polarization P_r and coercive field E_c were reported as functions of compressive stress for PMN-xPT compositions near the MPB at room temperature.[75,113] The remnant polarization for [001]-poled PMN-32PT under uniaxial compressive stress in the poling direction decreased with increasing stress for all stresses considered.[75] It ranged from 0.25 to 0.04 C/m^2 for stress between 0 and 40 MPa.[75] In addition, the coercive electric field E_c decreased with increasing compressive stress up to 15 MPa and remained constant at 0.08 MV/m for further increasing stress.[75] Similar trends were reported for [001]-poled PMN-30PT and [001]-poled PMN-33PT.[113]

Herklotz *et al.*[74] reported the zero-field, zero-stress relative permittivity of [001] poled and unpoled PMN-28PT as a function of temperature. The authors found the unpoled crystals to exhibit typical relaxor ferroelectric behavior featuring one broad peak in the relative permittivity versus temperature diagram.[74] On the other hand, the [001]-poled crystals exhibited a second pronounced peak at 97^{o}C in the relative permittivity versus temperature diagram where the crystal underwent a monoclinic to tetragonal phase transition.[74] In addition, Suchanicz and Kania[120] reported the peak of the relative permittivity of unpoled PMN-28PT to decrease with increasing uniaxial stress in the [001] direction. Furthermore, the relative permittivity of PMN-xPT is frequency-dependent typical of relaxor behavior.[91,120] For example, Chen *et al.*[91] found the peak of the relative permittivity as a function of temperature for PMN-20PT ceramics heated at 1 ^{o}C/min to vary from 84 to 96^{o}C for frequency ranging from 0.1 to 100 kHz.

Thermal properties

Slodczyk[121] reported the lattice parameters as a function of temperature for PMN-xPT with x ranging from 9 to 64 mol%. The lattice parameter a of PMN-28PT increased with increasing temperature up to 110^{o}C where it reached a local maximum.[121] This behavior can be attributed to continuous polarization from the rhombohedral to tetragonal phase.[74] With further heating, a decreased between 110 and 130^{o}C and then remained nearly constant up to 200^{o}C.[121] This can be attributed to the relaxation of the material from the tetragonal to the cubic phase.[74] Finally, the lattice parameter a began to increase rapidly with further heating beyond 200^{o}C.[121] The thermal expansion coefficient in the [001] direction α can be estimated from the lattice parameter $a(T)$ according to[122]

$$\alpha(T) = \frac{1}{a}\frac{\mathrm{d}a}{\mathrm{d}T} \tag{4.1}$$

Tang *et al.*[118] used differential scanning calorimetry to measure the specific heat of PMN-xPT for x ranging from 13 to 40 mol% in the temperature range 20 to 55^{o}C. The authors found that the specific heat increased with increasing temperature and was about 2.5 MJ/m^3·K at room temperature over a wide range of compositions.[118] In addition, Kutnjak and Blinc[123] found, at zero-field, that the enthalpy associated with the cubic-tetragonal (C-T) phase transition $\Delta h_{\text{C-T}}$ was larger than that associated with the tetragonal-monoclinic (T-M$_C$) phase transition $\Delta h_{\text{T-M}_C}$ in single crystal PMN-29.5PT, namely $\Delta h_{\text{C-T}}$=0.092 J/g versus $\Delta h_{\text{T-M}_C}$=0.035 J/kg.[123]

Bipolar hysteresis loop simulation

The Preisach model assumes that hysteresis loops can be described as the parallel connection of independent relay hysterons.[124] Many models simulating bipolar dielectric hysteresis loops of ferroelectric materials have been developed based on this theory.[125–128] These models have been demonstrated to accurately predict history-dependent properties[125] as well as hysteresis loops at various frequency[128] and temperature.[127,128] Schultz *et al.*[127] developed a model based on Preisach theory that accurately predicted the bipolar D-E loops of pyroelectric

strontium bismuth tantalate for temperature ranging from 20 to 150^{o}C. This model was given by[127]

$$\begin{aligned} D(E) &= \frac{2P_s}{\pi^2}\left\{tan^{-1}\left[tan\left(\frac{\pi P_r}{2P_s}\right)\left(\frac{E}{E_c}-1\right)\right]+\frac{\pi}{2}\right\}\times \\ &\times \left\{tan^{-1}\left[tan\left(\frac{\pi P_r}{2P_s}\right)\left(\frac{E}{E_c}+1\right)\right]+\frac{\pi}{2}\right\}-P_s+\varepsilon_r\varepsilon_0 E \end{aligned} \tag{4.2}$$

where b is the thickness of the ferroelectric sample, E is the applied electric field, and ε_o is the vacuum permittivity. The remaining parameters consist of the dielectric properties P_r, E_c, ε_r, and P_s that can be extracted from measured D-E loops. The remnant polarization P_r corresponds to D at zero electric field and the coercive field E_c corresponds to the electric field required so that the electric displacement equals zero. The saturation polarization P_s and large-field relative permittivity ε_r can be retrieved according to Equation (2.9) as previously discussed.

4.3 Experiments

4.3.1 Samples

Lead magnesium niobate-lead titanate single crystal samples with the composition $0.72PbMg_{1/3}Nb_{2/3}O_3$-$0.28PbTiO_3$ (PMN-28PT) were purchased from Sinoceramics, LLC. The samples were 5 × 5 × 3 mm^3 and poled in the [001]-direction. The two 5 × 5 mm^2 faces of each sample were entirely coated with Cr/Au electrodes. The average weight of the samples was 588.5±0.8 mg, corresponding to a density of ρ=7847±11 kg/m^3.

4.3.2 Bipolar hysteresis

Experimental setup

The experimental setup consisted of a thermomechanical and an electrical subsystem. The electrical subsystem consisted of a Sawyer-Tower circuit[129] and was described in Ref.[44,97,130] The thermomechanical subsystem was similar to that we used previously.[112] In brief, it

consisted of a piston actuated by compressed air, an isothermal silicone oil bath, an acrylic support structure, and two copper rods. A sample was placed in the acrylic sample holder and sandwiched between two copper rods. The sample holder forced the motion of the copper rods along the vertical axes. Then, compressed air actuated a McMaster-Carr 6498K252 air cylinder that applied force to the copper rods, thus compressing the sample. The applied compressive stress σ was controlled by the air pressure reaching a maximum of 469 kPa. This assembly was placed inside of an isothermal silicone oil bath. The bath temperature was kept constant using an Omega CN-7823 proportional integral derivative (PID) temperature controller and a 100 W cartridge heater immersed in the oil. Note that this experimental setup is described in further detail in Chapter 7 Section 7.2.2 and shown in Figure 7.2.

Experimental procedure

Isothermal and isostress bipolar D-E loops were collected for stress ranging from 0 to 25.13 MPa for temperature ranging from 22 to 170^{o}C in 10^{o}C increments. These D-E loop measurements were carried out by imposing a continuous triangular voltage signal across the sample. The amplitude of the applied voltage corresponded to an electric field cycling between -0.75 and 0.75 MV/m. For each temperature and stress four consecutive D-E loops were collected. The low frequency of 0.1 Hz was chosen to allow the sample to fully relax and to maximize the amplitude of the electric displacement.

Dielectric properties

The dielectric properties of PMN-28PT were estimated from the isothermal and isostress bipolar D-E loops. The saturation polarization $P_s(T, \sigma)$ and the large-field dielectric permittivity $\varepsilon_r(T, \sigma)$ were evaluated by linearly fitting the bipolar D-E loops corresponding to a decrease in electric field from 0.75 to 0.2 MV/m according to Equation (2.9). The remnant polarization $P_r(T, \sigma)$ and the coercive electric field $E_c(T, \sigma)$ were evaluated by determining the electric displacement at zero electric field and the electric field corresponding to zero

electric displacement, respectively.

Phase transitions

PMN-28PT undergoes continuous phase transitions occurring over a range of electric fields.[96] The onset and completion of electric field induced phase transitions were estimated from the upper section of the isothermal and isostress bipolar D-E loops corresponding to electric field decreasing from 0.75 to 0 MV/m. The presence of a single phase in a ferroelectric single crystal yields a dielectric permittivity that is independent of electric field corresponding to linear behavior of D versus E.[67] The presence of a phase transition corresponds to the experimental D-E loop deviating from linearity. The beginning and end of a phase transition were defined as the electric fields corresponding to the slope of the experimental D-E loop deviating by 5% from linear behavior.[96] This method was previously implemented on unipolar D-E loops for varying temperature and compressive stress to estimate the phase boundaries of single crystal PMN-32PT.[96]

4.3.3 Differential scanning calorimetry

Differential scanning calorimetry (DSC) measurements were performed using a Diamond DSC (by Perkin Elmer, USA). The specific heat $c_p(T)$ of the PMN-28PT sample was estimated as

$$c_p(T) = \frac{\dot{Q}_{DSC}}{m\dot{T}} \tag{4.3}$$

where $\dot{Q}_{DSC}$ is the measured heat transfer rate (in W) to achieve constant heating or cooling rate of $\dot{T}{=}dT/dt$ (in ^{o}C/s) for a sample of mass m (in kg).

The DSC instrument was successfully calibrated using an indium standard of mass 5.6 mg. The melting temperature at atmospheric pressure and specific phase change enthalpy were measured to be 160.8^{o}C and 26.9 J/g, respectively. These values fall within 2.7% and 5.6% of the properties reported in the literature.[131] The procedure to measure the specific heat c_p was also validated using an aluminum sample of mass 47 mg. The specific heat c_p of

aluminum was found to be 898 J/kg·K at 27^{o}C falling within 0.6% of the value reported in the literature.[132] In addition, we verified that the measured specific heat $c_p(T)$ of PMN-28PT samples was independent of heating/cooling rate $\dot{T}$ between 5 and 10^{o}C/s.

4.4 Results and discussion

4.4.1 Bipolar hysteresis loops

Figure 4.1 plots the isothermal and isostress bipolar D-E loops measured at 0.1 Hz for temperatures between 22 and 170^{o}C under compressive stress (a) σ=0 MPa, (b) σ=6.16 MPa, (c) σ=10.38 MPa, (d) σ=18.81 MPa, (e) σ=23.02 MPa, and (f) σ=25.13 MPa. The consecutive D-E loops at any given stress and temperature overlapped establishing that leakage current was negligible. Figure 4.1a indicates that the material exhibited square ferroelectric behavior with large polarizations at temperatures up to 90^{o}C. Between 90 and 130^{o}C the electric displacement decreased slightly with increasing temperature. Above 130^{o}C, the loops became slimmer with increasing temperature and degenerated into narrow and linear loops. The D-E loops under the small compressive stresses of 6.16 MPa (Figure 4.1b) and 10.38 MPa (Figure 4.1c) exhibited behavior similar to zero stress except, for a given temperature, the loops became slimmer with increasing stress. This was previously observed at room temperature for PMN-xPT with x=30, 32, and 33 mol%.[75,113] This can be attributed to the increasing stress providing an increasing energy barrier to polarization rotation.[75] Furthermore, Figures 4.1e and 4.1f demonstrate that for a given temperature between 22 and 170^{o}C, the D-E loops under 23.02 and 25.13 MPa were nearly indistinguishable. In other words, increasing the compressive stress above 23.02 MPa did not change the dielectric behavior of [001] PMN-28PT for the temperature range considered.

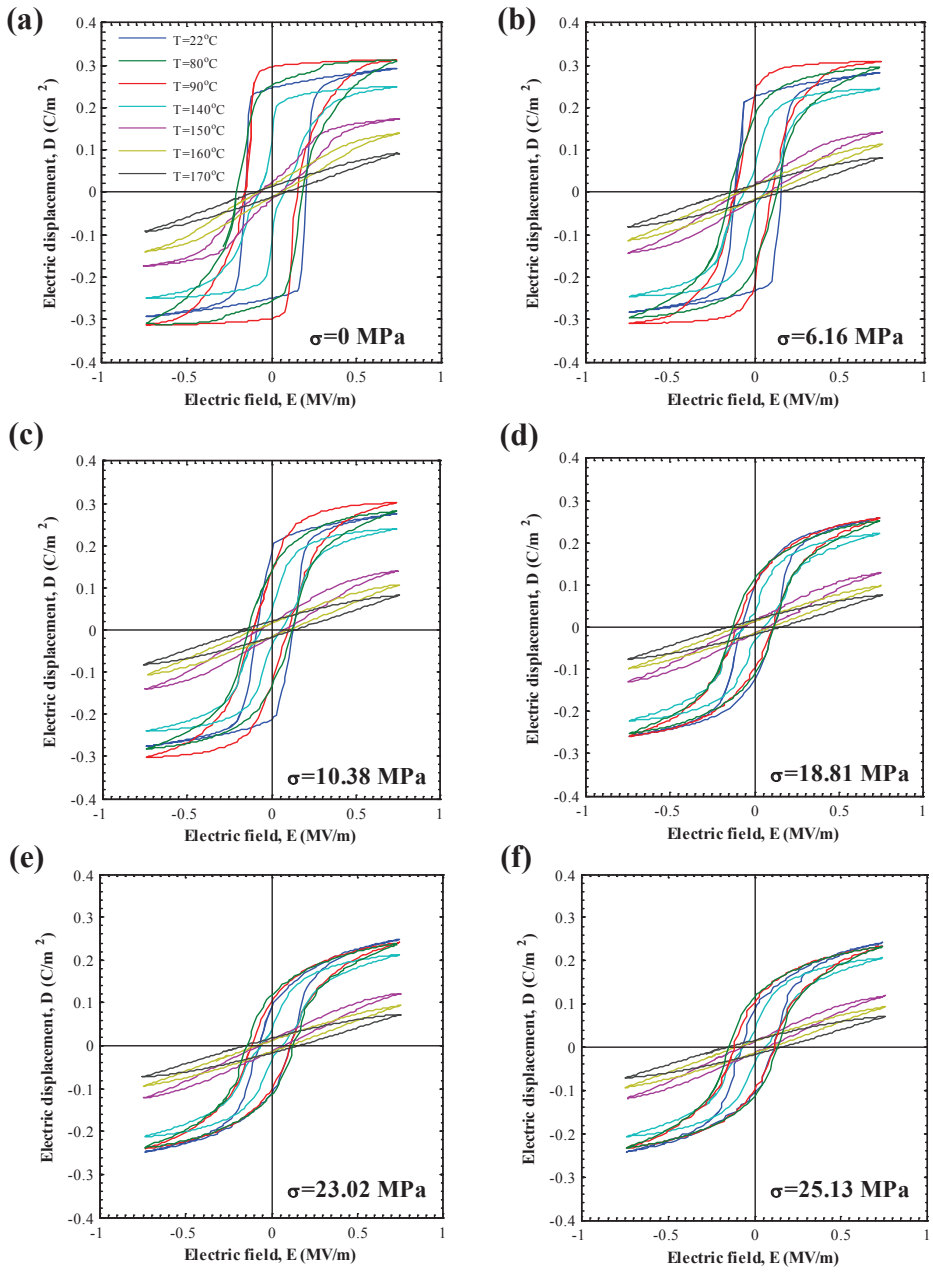

Figure 4.1: Experimental bipolar isothermal and isostress electric displacement versus electric field (D-E) hysteresis curves measured at 0.1 Hz for temperatures between 22 and 170^{o}C under (a) σ=0 MPa, (b) σ=6.16 MPa, (c) σ=10.38 MPa, (d) σ=18.81 MPa, (e) σ=23.02 MPa, and (f) σ=25.13 MPa.

4.4.2 Dielectric properties

Remnant polarization

Figure 4.2 plots the remnant polarization P_r of [001] PMN-28PT as a function of temperature between 22 and 170^{o}C for uniaxial compressive stress ranging from 0 to 25.13 MPa. For any given temperature, the remnant polarization decreased with increasing compressive stress up to 18.81 MPa. For compressive stress above 18.81 MPa, P_r was small and independent of compressive stress. This behavior can be attributed to the large compressive stress inducing a small polarization component along the applied field direction.[75]

Under compressive stress σ less than or equal to 6.16 MPa, the remnant polarization was the largest at 90^{o}C where the single crystal was in the tetragonal phase. Above 90^{o}C, P_r decreased with increasing temperature as the material relaxed into the cubic phase, as previously observed for [001] PMN-28PT under zero stress.[74] Note that Herklotz *et al.*[74] observed a decrease in P_r for [001] PMN-28PT in the M_C phase between 63 and 72^{o}C. Figure 4.2 indicates that this feature was present at 80^{o}C under 6.16 MPa, but not at 0 MPa. However, this can be attributed to the large temperature increments of the measurements. In fact, D-E loops were measured by 10^{o}C increments in the present study, while they were measured continuously during heating at 2^{o}C/min in Ref.[74]

Under large compressive stress σ greater than or equal to 18.81 MPa, the remnant polarization was less than 0.1 C/m^2 up to 60^{o}C indicating the material was in the orthorhombic phase. At these large stresses, P_r reached a maximum at 70^{o}C and was nearly constant between 70^{o}C and 110^{o}C. The increase in P_r from 60 to 70^{o}C can be attributed to a polarization rotation occurring from orthorhombic towards rhombohedral phase via a monoclinic M_B pathway, as previously observed in [001] PMN-32PT.[75] For temperatures beyond 110^{o}C, P_r decreased with increasing temperature as the material relaxed into the cubic phase.

The behavior of the remnant polarization between 6.16 and 18.81 MPa exhibited features characteristic of an unstable equilibrium, as previously observed in [001] PMN-32PT.[75] Wan *et al.*[75] observed that the sample went through orthorhombic to rhombohedral phase tran-

sition at zero-field upon unloading for compressive stress less than 10 MPa. On the other hand, for compressive stress greater than 10 MPa, the crystals remained in the orthorhombic phase upon the removal of the stress.[75] In this case, [001] PMN-28PT under a compressive stress of 10.38 MPa remained in the rhombohedral phase up to 40^{o}C at zero electric field. However, for temperatures between 50 and 60^{o}C, the crystals took on the orthorhombic phase at zero electric field, as indicated by the small remnant polarization. At 70^{o}C, the remnant polarization increased indicating a polarization rotation towards the rhombohedral phase. Then, for temperature T greater than or equal to 70^{o}C, P_r decreased with increasing temperature as the material relaxed into the cubic phase.

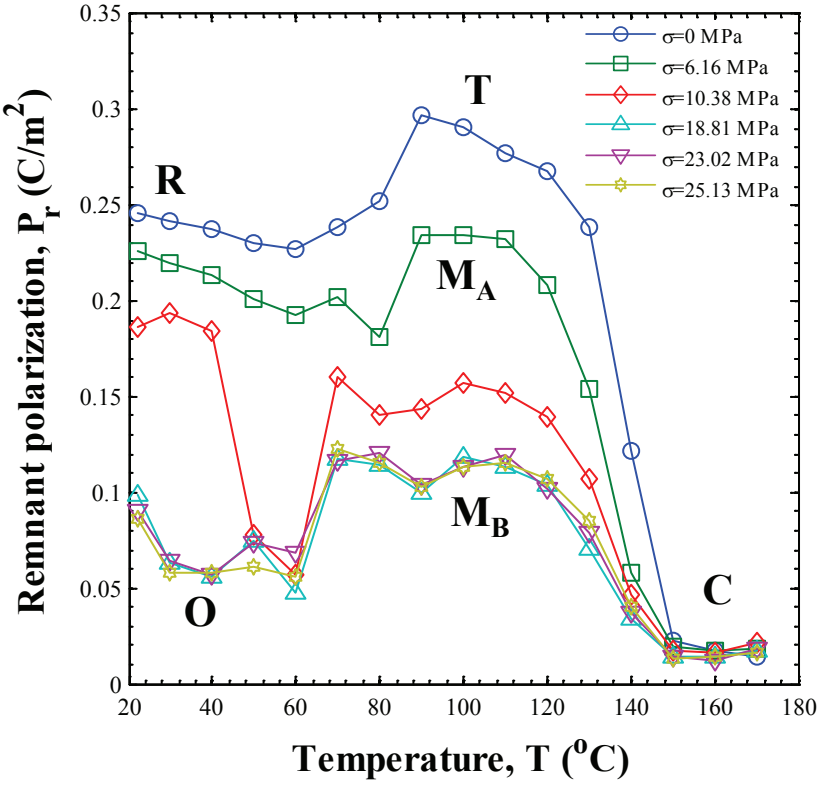

Figure 4.2: Measured remnant polarization P_r of PMN-28PT single crystal as a function of temperature for compressive stress ranging from 0 to 25.13 MPa.

Coercive electric field

Figure 4.3 shows the coercive electric field E_c as a function of temperature between 22 and 170^{o}C for compressive stress ranging from 0 to 25.13 MPa. The coercive field E_c under all compressive stresses followed a similar trend to that previously observed in [001] PMN-28PT between 22 and 140^{o}C under zero stress.[74] For any given temperature up to 60^{o}C, E_c decreased with increasing stress up to 18.81 MPa. Beyond 18.81 MPa, it became nearly independent of compressive stress and was dependent only on temperature. This is consistent with the behavior of E_c previously observed at room temperature for PMN-xPT with x=31, 32, and 33 mol%.[75,113] For temperature between 70 and 110^{o}C and all non-zero stresses, the coercive field E_c was nearly constant. This indicates that the same electric field was required to induce polarization switching for all compressive stresses in this temperature range. For temperature greater than 130^{o}C, E_c increased with increasing temperature for all compressive stresses.

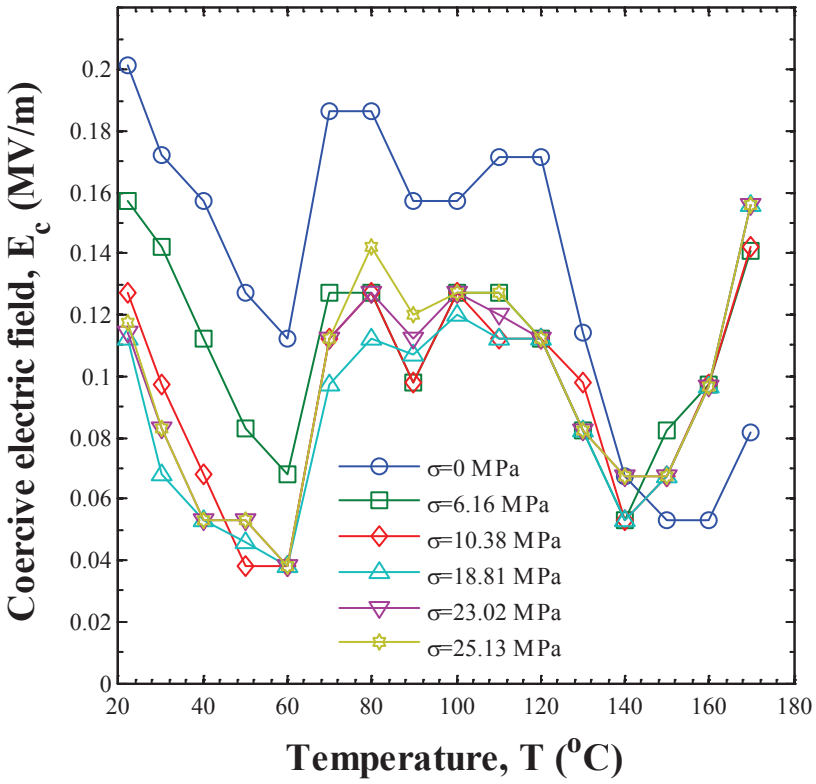

Figure 4.3: Measured coercive electric field E_c of PMN-28PT single crystal as a function of temperature for compressive stress ranging from 0 to 25.13 MPa.

Saturation polarization

Figure 4.4a plots the saturation polarization $P_s(T)$ as a function of temperature between 22 and 170^{o}C for uniaxial compressive stress varying from 0 to 25.13 MPa. For a given temperature, the saturation polarization decreased with increasing compressive stress. This behavior can be attributed to the large compressive stress constraining polarization rotation towards the electric field direction.[75] In addition, for a given compressive stress, the saturation polarization P_s reached a maximum $P_{s,max}$ between 90 and 100^{o}C and decreased with further increase in temperature as the material relaxed into the cubic phase. Furthermore, for temperature above 150^{o}C, the saturation polarization was negligibly small (P_s $\leq$0.03

C/m^2) for all compressive stresses.

Figure 4.4b plots the maximum saturation polarization $P_{s,max}(\sigma)$ as a function of compressive stress. The solid line represents a polynomial fit and was plotted to guide the eye. The maximum saturation polarization $P_{s,max}(\sigma)$ was maximum under zero stress and decreased with increasing compressive stress. Figure 4.4c plots the non-dimensional saturation polarization $P_s(T)/P_{s,max}(\sigma)$ as a function of temperature. It indicates that the saturation polarization $P_s(T)$ exhibited self-similar behavior between 90 and 170^{o}C for all compressive stresses tested. In fact, Piquette *et al.*[133] suggested fitting $P_s(T)$ with the Fermi function. In this case, taking advantage of the self-similar behavior, $P_s(T)/P_{s,max}(\sigma)$ can be fitted according to the Fermi function given by,

$$\frac{P_s(T)}{P_{s,max}(\sigma)} = \frac{1}{1 + e^{c(T-T_0)}} \tag{4.4}$$

where the empirical constants were determined by the least square method to be c=0.18 K^{-1}, and T_0=145^{o}C. This suggests that the ferroelectric to paraelectric phase transition temperature at large electric field occurred around 145^{o}C. However, below 90^{o}C, the saturation polarization plots did not collapse perfectly. This can be attributed to the fact that phase transition sequence in the temperature range 22 to 90^{o}C was not the same for all compressive stresses considered.

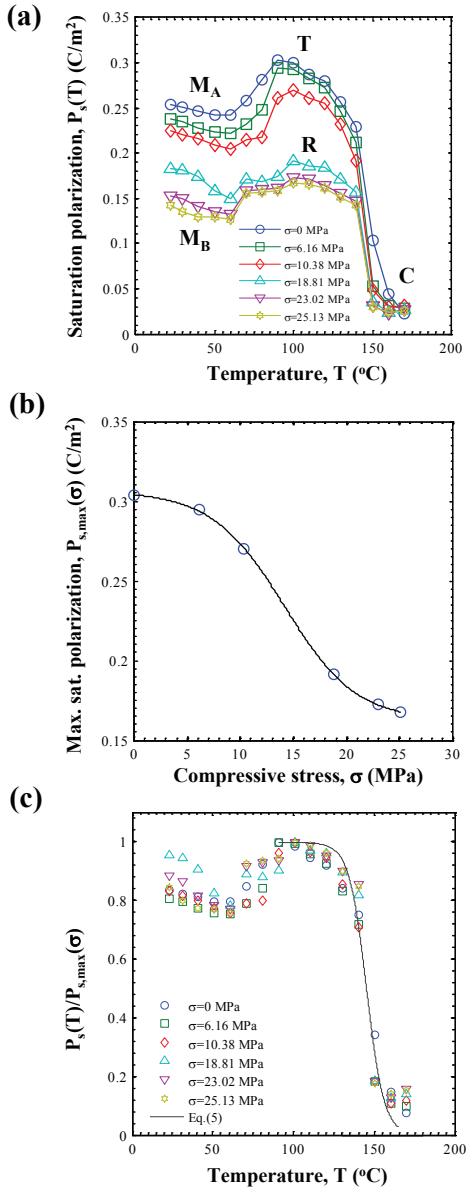

Figure 4.4: (a) Measured saturation polarization $P_s(T)$ as a function of temperature for compressive stress ranging from 0 to 25.13 MPa (b) Maximum saturation polarization $P_{s,max}(\sigma)$ as a function of compressive stress. The solid line represents a polynomial fit and was plotted to guide the eye. (c) Non-dimensional measured saturation polarization $P_s(T)/P_{s,max}(\sigma)$ as a function of temperature and fitting curve given by Equation (4.4) with c=0.18 K^{-1}, and T_0=145^{o}C.

Large-field relative permittivity

Figure 4.5 plots the large-field relative permittivity as a function of temperature for compressive stress ranging from 0 to 25.13 MPa. For a given temperature, the large-field relative permittivity ε_r increased with increasing compressive stress. For compressive stress σ less than 10.38 MPa, ε_r increased between 22 and 60^{o}C and decreased between 60 and 120^{o}C. Between 120 and 140^{o}C, it increased and reached a maximum around 150^{o}C. This behavior was similar to that reported by Herklotz *et al.*[74] for [001]-poled PMN-28PT under zero stress and zero electric field. Then, the local peak around 100^{o}C was attributed to the monoclinic to tetragonal phase transition.[74] In the present case, at large-field, the M_A-T phase transition occurred between 60 and 80^{o}C under compressive stress σ less than or equal to 10.38 MPa. In addition, the peak of the large-field permittivity indicated the Curie temperature at large electric field was 160^{o}C under zero stress and 150^{o}C for all non-zero stresses. Figure 4.5 indicates that, for large electric field, the magnitude of this peak decreased slightly with increasing stress. This trend was previously observed in the zero-field relative permittivity of PMN-28PT for varying uniaxial stress applied in the [001] direction.[120] Note that the magnitude of the peaks in the large-field relative permittivity were significantly lower than those of the zero-field relative permittivity.[74] This is consistent with the behavior reported for [111] PMN-29.5PT for electric field ranging from 0 to 0.4 MV/m.[134] Overall, the smaller relative permittivity at large-field can be attributed to the fact that the material was typically near saturation at large electric fields.

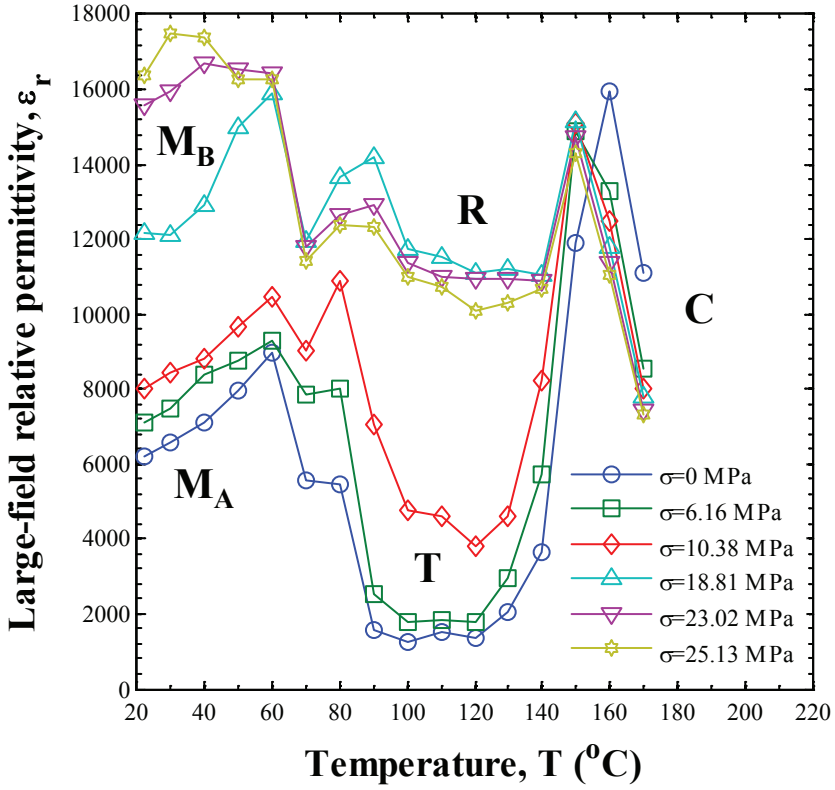

Figure 4.5: The large-field dielectric permittivity ε_r of PMN-28PT single crystal as a function of temperature for compressive stress ranging from 0 to 25.13 MPa.

4.4.3 Bipolar hysteresis simulation

Figure 4.6a compares the experimental and predicted D-E loops for three representative cases corresponding to (i) T=40^{o}C, σ=6.16 MPa, (ii) T=90^{o}C, σ=0 MPa, (iii) T=130^{o}C, σ=10.38 MPa, and (iv) T=170^{o}C, σ=25.13 MPa. The model predictions were computed based on Equation (4.2) using the dielectric properties retrieved from the experimental D-E loops. The first case represents one where the model predictions were accurate. The remaining three cases represent three phenomena that yielded large average relative error between the experimental and predicted bipolar D-E loops. The average relative error associated with these four cases was 3.7%, 25.8%, 24.3%, and 50.4%, respectively. For the first case, the

model accurately captured the behavior of the experimentally measured D-E loop for all electric fields. For the second case, the model did not accurately predict D for electric fields ranging from 0.1 to 0.6 MV/m. In fact, at 90^{o}C PMN-28PT was in the tetragonal phase.[74] Thus, the polarization direction switched by 180^o as the applied [001] electric field went from negative to positive. The model predicted that this switching process occurred in the electric field span 0.1 to 0.2 MV/m, when in fact, it occurred over a broader range from 0.1 to 0.6 MV/m. For the third case, the model under-predicted the electric displacement for all electric fields. As the electric field increased, this experimental loop exhibited double hysteresis characteristic of the growth of ferroelectric domains in the paraelectric phase.[72] The model did not capture the upturn of the loop as the electric field increased beyond 0.2 MV/m, and thus under-predicted the saturation behavior. For the fourth case, the sample was in the paraelectric phase for all electric fields considered and the experimental loop demonstrated linear dielectric behavior. The model was based on an inverse tangent function and intended to predict ferroelectric behavior. Thus, it over-predicted the electric displacement for electric field increasing from 0 to 0.75 MV/m leading to large average relative error. However, it is evident from Figure 4.6a that the model adequately captured the paraelectric behavior of the sample.

Figure 4.6b shows the average relative error between the experimental and simulated D-E loops as the electric field E varies between -0.75 and 0.75 MV/m for temperature ranging from 22 to 170^{o}C and compressive stress σ ranging from 0 to 25.13 MPa. Overall, the average relative error increased with increasing temperature. This can be attributed to the fact that, as the temperature increased, the absolute electric displacement decreased. Thus, similar absolute errors led to a larger relative error at high temperatures. For example, the average absolute error was 0.016 and 0.0065 C/m^2 under σ=25.13 at 22 and 170^{o}C, respectively. Then, the respective average relative errors were 10.0 and 50.4%. In addition, for temperature up to 80^{o}C, the model predicted within 20% on average for all compressive stresses. Furthermore, Figure 4.6b indicates that the average relative error between the model predictions and the experimental loops was independent of compressive stress for

σ>0 MPa. This demonstrates that the model is valid for non-zero compressive stress.

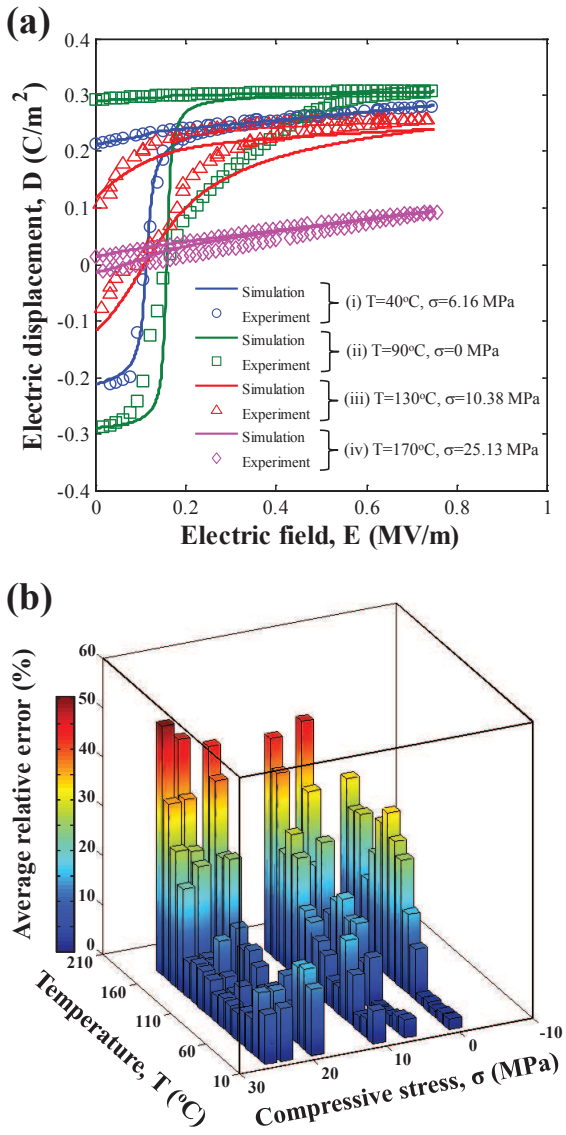

Figure 4.6: (a) Experimental and predicted D-E loops for (i) T=40^{o}C and σ=6.16 MPa, (ii) T=90^{o}C and σ=0 MPa, (iii) T=130^{o}C and σ=10.38 MPa, and (iv) T=170^{o}C and σ=25.13 MPa. (b) The average relative error between the experimental and predicted D-E loops as a function of temperature and compressive stress. Predictions were based on Equation (4.2) using the dielectric properties retrieved from the experimental loops.

4.4.4 Phase transition map

Figure 4.7 shows the electric field and temperature corresponding to onset and completion of electric field induced phase transitions in the E-T diagram under compressive stress (a) σ=0 MPa, (b) σ=6.16 MPa, (c) σ=10.38 MPa, (d) σ=18.81 MPa, (e) σ=23.02 MPa, and (f) σ=25.13 MPa. The orientation of the polarization vectors for a given phase are shown in Figure 2.6. Note that the phase transitions in PMN-xPT near the MPB are continuous occurring over a range of electric fields.[96] For a given temperature and compressive stress, the electric fields corresponding to the onset and completion of a phase transition for decreasing electric field was the electric field where the experimental D-E loop displayed a 5% variation of slope from the linear material response.[96] The solid lines correspond to linear fits of the phase transition points retrieved experimentally. The vertical lines correspond to temperature induced phase transitions. The phases on either side of each boundary were determined by referring to recent studies of phase transitions in PMN-xPT near the MPB.[74–76] These determinations were supported by analysis of the dielectric properties. Figure 4.7a shows the phase boundaries determined by Herklotz *et al.*[74] for [001] PMN-28PT from unipolar D-E loops at 10 Hz. The experimentally determined phase transition points fall approximately on the phase boundaries previously reported.[74] This indicates that this method of determining electric field induced phase transitions was consistent with that of Ref.[74] Note that the M_A-R boundary shown in Figure 4.7a was observed by Herklotz *et al.*[74] during step-wise increase in electric field at constant temperature after zero-field cooling. It was not present in the unipolar loops at 10 Hz.[74] Its presence here can be attributed to the low frequency of the D-E loops allowing enough time for the polarization rotation from monoclinic to rhombohedral to begin to occur as the electric field decreased. This behavior has been previously observed in PZN-4.5PT single crystal possessing an electric field induced phase transition at 0.01 Hz that was absent at 10 Hz.[34]

Figures 4.7b and 4.7c demonstrate the growth of the rhombohedral phase with increasing compressive stress similar to that observed in [001] PMN-32PT.[76] In addition, the growth of the cubic phase region with increasing stress is evident. This was done at the expense of

the tetragonal phase whose region shrank with increasing stress and was not present for any small electric field. As the electric field was decreased in the tetragonal phase, the material underwent a phase transition into a monoclinic M_A or M_C phase. This is supported by the fact that (i) the material exhibits continuous polarization rotation and (ii) the remnant polarization was the largest in this temperature range for all compressive stresses considered. However, due to the fact that the monoclinic M_C phase was not present in all PMN-28PT samples,[74] it is likely that the material was in the monoclinic M_A phase.

Figures 4.7d, 4.7e, and 4.7f illustrate the phase boundaries for large stress conditions. The material was in the orthorhombic phase under small electric field and temperature less than 60^oC as previously observed in PMN-32PT.[76] As the electric field increased, the material transitioned into the intermediate monoclinic M_B phase. This is supported by the continuous polarization rotation between the rhombohedral and orthorhombic phases via monoclinic M_B pathways observed in PMN-32PT for compressive stress exceeding 15 MPa.[75] In addition, PMN-28PT did not reach the rhombohedral phase in this regime. This is supported by the fact that the saturation polarization for large compressive stress was less 0.2 C/m^2, while the remnant polarization under small stress and temperature when the material was in the rhombohedral phase was greater than 0.2 C/m^2.

Furthermore, between 60 and 70^oC, the material underwent a temperature induced phase transition shown with vertical grey lines. This was indicated by an increase in both the remnant and saturation polarizations (Figures 4.2 and 4.4a). Thus, for temperatures above 70^oC, the phase transition induced for decreasing electric field must correspond to rhombohedral to monoclinic M_B to maintain continuous polarization rotation. Moreover, for a given temperature, the electric field corresponding to the onset of the M_B-O transition increased with increasing stress. Finally, the tetragonal phase was not present under large stress. Overall, Figures 4.7 illustrates that, for any fixed temperature and electric field, the material is not in the same phase under all compressive stresses.

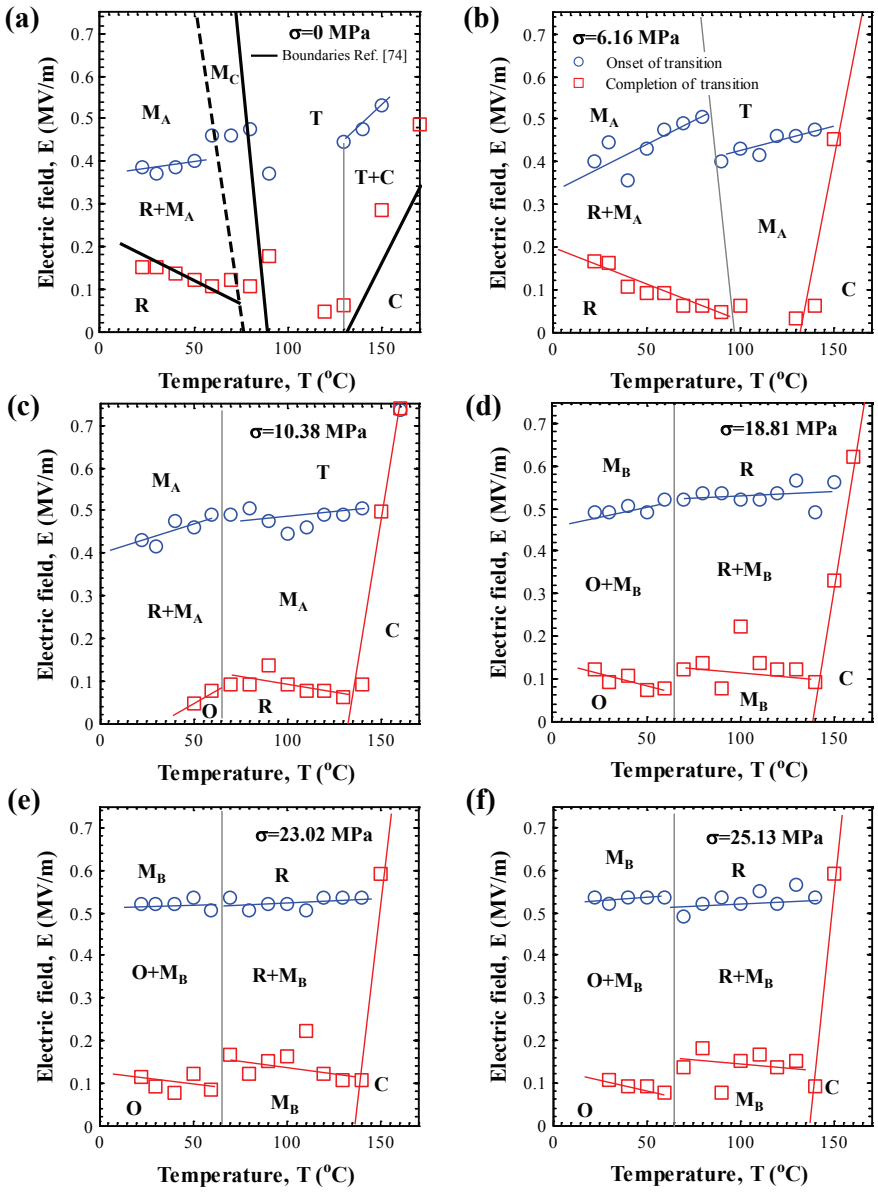

Figure 4.7: Experimentally measured phase transition points of [001]-poled PMN-28PT in the E-T diagram under [001] uniaxial compressive stress (a) σ=0 MPa, (b) σ=6.16 MPa, (c) σ=10.38 MPa, (d) σ=18.81 MPa, (e) σ=23.02 MPa, and (f) σ=25.13 MPa. In addition, the solid black lines in (a) correspond to the zero-stress phase boundaries reported in Ref.[74]

4.4.5 Thermal properties

Thermal expansion coefficient

Figure 4.8a shows the zero-field lattice parameter $a(T)$ as previously reported for unpoled PMN-28PT between 7 and 200^{o}C[121] and the accompanying third order polynomial spline fit. Figure 4.8a establishes that the variation in lattice parameter was well captured by the spline fit. Figure 4.8b shows the corresponding thermal expansion coefficient $\alpha(T)$ as a function of temperature for PMN-28PT. It was computed numerically according to Equation (4.1) using the spline fit of the lattice parameter $a(T)$ shown in Figure 4.8a. Figure 4.8b also shows the zero-field phase boundaries as reported by Herkoltz *et al.*[74] Figure 4.8b indicates that the thermal expansion coefficient of PMN-28PT reached a maximum in the tetragonal phase. As PMN-28PT was heated from 22^{o}C at zero field, it expanded until the temperature reached 108^{o}C when it began to contract. It continued to contract as the temperature increased to 140^{o}C where it transitioned into the cubic phase. For further heating beyond 140^{o}C, PMN-28PT underwent small thermal expansion up to 200^{o}C.

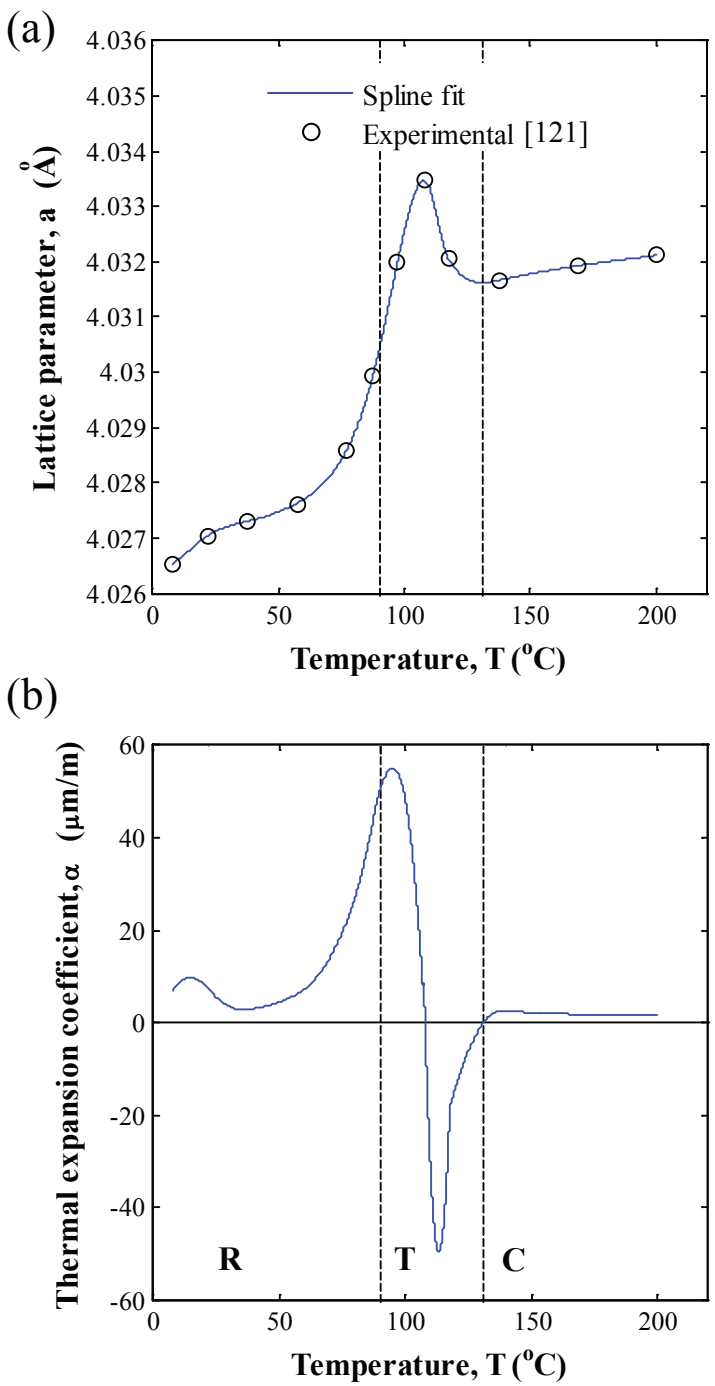

Figure 4.8: (a) Lattice parameter $a(T)$ of unpoled PMN-28PT single crystals as reported in Ref.[121] and associated spline fit along with (b) the corresponding thermal expansion coefficient $\alpha(T)$.

Specific heat

Figure 4.9 shows the specific heat c_p of [001]-poled PMN-28PT computed according to Equation (4.3) as a function of temperature T during heating from 15 to 175^{o}C, followed by cooling from 175 to 15^{o}C. The heating rate and sample mass were $\dot{T}$=10^{o}C/min and m=148.3 mg, respectively. The measured specific heat near room temperature was in good agreement with data reported in the literature.[118] Tang *et al.*[118] reported c_p of PMN-xPT single crystal at room temperature over a wide range of x to be 2.5 MJ/m^3·K. This corresponded to 319 J/kg·K assuming the density of PMN-28PT to be 7847 kg/m^3. In addition, during heating, the PMN-28PT sample exhibited peaks in c_p at the phase transition temperatures of 85 and 148^{o}C corresponding respectively to monoclinic M$_A$ to tetragonal (M$_A$-T) and tetragonal to cubic (T-C) phase transitions as suggested by the field cooling phase diagram for [001]-poled PMN-28PT.[117] The PMN-28PT sample underwent the reverse phase transition sequence during cooling with the phase transitions occurring at 132 and 69^{o}C. Such thermal hysteresis[61] has also been observed in PMN-xPT compositions with x ranging from 0 to 29.5%.[119,134]

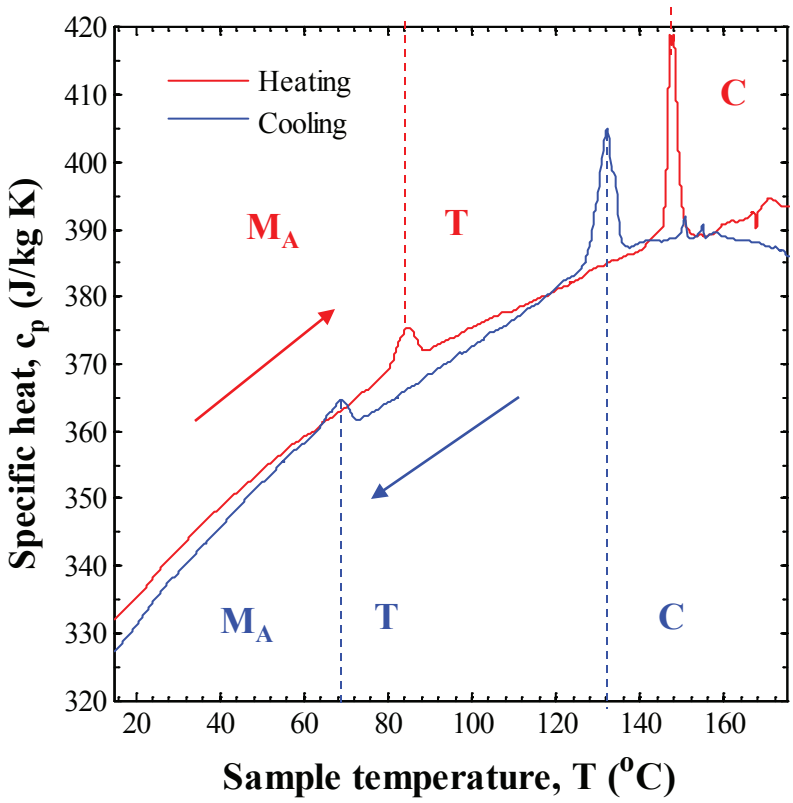

Figure 4.9: Measured specific heat $c_p(T)$ of PMN-28PT as a function of temperature between 15 and 175^{o}C.

Specific phase change enthalpy

The ferro- to paraelectric phase change enthalpy $\Delta h_{\text{T-C}}$ was 0.11 J/g for the PMN-28PT samples. The corresponding para- to ferroelectric phase change enthalpy $\Delta h_{\text{C-T}}$ was 0.094 J/g. In addition, the samples had a monoclinic M_A to tetragonal phase change enthalpy $\Delta h_{M_A\text{-T}}$ of 0.020 J/g and a corresponding tetragonal to monoclinic phase change enthalpy $\Delta h_{\text{T-}M_A}$ of 0.019 J/g. In other words, the energy associated with the ferroelectric to paraelectric phase transition was approximately five times larger than the energy associated with

the monoclinic M_A to tetragonal phase transition. Furthermore, Kutnjak and Blinc[123] reported $\Delta h_{\text{C-T}}$ of 0.092 J/g for PMN-29.5PT under zero electric field. A larger phase change enthalpy $\Delta h_{\text{C-T}}$ for PMN-28PT implied the presence of a larger ferroelectric phase in the sample.[130]

4.5 Chapter summary

This chapter presented experimental measurements of bipolar hysteresis D-E loops performed on [001]-poled PMN-28PT single crystals under uniaxial compressive stress in the [001] direction ranging from 0 to 25.13 MPa and temperature ranging from 22 to 170^{o}C. The dielectric properties were retrieved from the hysteresis curves and reported for all conditions considered. Then, the retrieved properties were used in a previously developed model to predict hysteresis D-E loops. The results indicated that the model agreed with experimental measurements within 20% for temperature up to 80^{o}C and for all compressive stresses considered. In addition, an E-σ-T phase diagram was developed. Finally, the thermophysical properties of PMN-28PT were reported as functions of temperature under zero stress at zero field including the enthalpy of phase change, the thermal expansion coefficient, and the specific heat.

CHAPTER 5

Phase Transitions and Thermal Expansion in Pyroelectric Energy Conversion

This chapter aims to elucidate the dynamic effects of phase transitions and thermal expansion on pyroelectric energy conversion. It reports the electrical energy and power densities generated by [001]-poled PMN-28PT single crystals undergoing the Olsen cycle under different cycle frequencies. It contributes to improving the performance of the Olsen cycle by taking advantage of different solid-state phase transitions to maximize the electrical energy and power generated.

5.1 Introduction

Recently, Kandilian *et al.*[97] derived a model estimating the energy density generated by relaxor ferroelectrics undergoing the Olsen cycle. The model was previously discussed in Chapter 2 Section 2.3.4 and is given by Equation (2.12). The last term on the right-hand side of Equation (2.12) represents the contribution of the secondary pyroelectric coefficient to the generated energy density due to dimensional changes in the crystal structure caused by temperature changes. This term accounted for the fact that the electric displacement bounds of Olsen cycle exceeded the bounds of the isothermal D-E loops at the cold and hot source temperatures T_C and T_H.[97] Equation (2.12) was validated with lanthanum-doped zirconate titanate (8/65/35 PLZT) ceramics[98] and PZN-5.5PT single crystals.[52] But then, the thermal expansion term was ignored because the Olsen cycle fell within the bounds of the isothermal D-E loops at T_C and T_H. The goal of this model was to rapidly characterize the energy density of materials undergoing the Olsen cycle without physically having to

perform the cycle. However, without performing the cycle, it is currently unclear whether to include the thermal expansion term in predicting N_D. This problem is due to a lack of understanding of the physical phenomena taking place during the cycle which is exacerbated by experimental uncertainty in the actual sample temperature which may differ from the hot and cold source temperatures. This chapter aims to elucidate the dynamic effects of thermal expansion and temperature induced phase transitions on the energy density generated during the Olsen cycle. It identifies the circumstances under which the contribution of the secondary pyroelectric effect is important.

5.2 Experiments

Single crystal PMN-28PT samples similar to those described in Chapter 4 Section 4.3.1 were used in this study.

The Olsen cycle was performed using an experimental setup consisting of the electrical and thermal subsystems described in detail in Refs.[97,101] and presented in Chapter 2 Section 2.3.2. In brief, the thermal subsystem was composed of two isothermal silicone oil baths held at constant and uniform temperatures T_C=22^{o}C and T_H=140^{o}C. The electrical subsystem consisted of a high-voltage power amplifier and a Sawyer-Tower circuit.[129] Note that the sample temperature was not measured to avoid electrical conduction between the thermocouple and the sample. Alternatively, the lumped capacitance approximation[105] can be used to predict the sample temperature $T_s(t)$ as a function of time t after it is transferred from the hot silicone bath at 140^{o}C. It is valid when the Biot number, defined as $Bi = h(t)L/k$, is much less than 1.0 where $h(t)$ is the heat transfer coefficient, L is the sample characteristic length, and k is its thermal conductivity. The energy conservation equation is given by $\rho c_p \not{V} \mathrm{d}T_s/\mathrm{d}t = -h(t)A_s(T_s - T_C)$ where A_s and $\not{V}$ are the surface area and volume of the sample, i.e., A_s=1.1 cm^2 and $\not{V}$=0.075 cm^3. The heat transfer coefficient $h(t)$ due to natural convection was estimated based on a correlation given in Ref.[135] to find an analytical expression for $T_s(t)$ presented Appendix A.1.

First, isothermal bipolar D-E loops were collected by applying a triangular voltage signal

at 0.1 Hz across the single crystal samples in silicone oil baths between 22 and 170^{o}C by increments of 10^{o}C. This corresponded to an electric field varying from -0.75 to 0.75 MV/m. The saturation polarization $P_s(T)$ and the large-field dielectric constant $\varepsilon_r(T)$ were retrieved by fitting the linear portion of each D-E loop corresponding to electric field decreasing from 0.75 to 0.2 MV/m with Equation (2.9) for each temperature. Then, the Olsen cycle was performed by consecutively dipping the samples in the hot and cold silicone oil baths while cycling the electric field between E_L=0.2 MV/m and E_H=0.75 MV/m. The cycle was performed at two different cycle frequencies, namely 0.0173 and 0.0211 Hz. The lowest cycle frequency allowed the electric displacement D to reach a steady state before the next process of the Olsen cycle was performed, corresponding to quasiequilibrium conditions. At higher frequency, isothermal processes 1-2 and 3-4 were performed after processes 4-1 and 2-3 as soon as the electric displacement reached a maximum or minimum, respectively.

Finally, in order to compare experimental results and predictions by Equation (2.12), the thermal expansion coefficient α was necessary. The latter was estimated from the lattice parameter $a(T)$ according to Equation (4.1) as previously discussed in Chapter 4 Section 4.4.5. Then, the strain x_3 was computed by numerically integrating $\alpha(T)$ between T_C and T using the trapezoidal rule. The zero-field lattice parameter $a(T)$[121] and the corresponding thermal expansion coefficient $\alpha(T)$ as a function of temperature for PMN-28PT were presented in Chapter 4 Section 4.4.5.

5.3 Results and discussion

Table 5.1 summarizes the properties of [001] PMN-28PT needed in the model given by Equation (2.12). The piezoelectric coefficient d_{33} and the elastic compliance s_{33} at 22^{o}C were reported in the literature.[92] The strain x_3 was estimated between 22 and 90^{o}C as well as between 22 and 140^{o}C from the lattice parameter reported by Slodczyk,[121] as previously discussed. It should be noted that x_3 between 22 and 90^{o}C represents more than 70% of its value between 22 and 140^{o}C. In addition, $P_s(T)$ and $\varepsilon_r(T)$ were retrieved from the D-E loops at 22, 90, and 140^{o}C based on Equation (2.9).

Table 5.1: [001] PMN-28PT properties reported in the literature used in Equation (2.12) to predict N_D.

Properties	**Units**				**Ref.**
T	(^{o}C)	22	90	140	
P_s	(μC/cm^2)	19.11	23.05	16.78	
ε_r	-	3475	2037	4026	
d_{33}	(pC/N)	2365	-	-	[92]
s_{33}	(pm^2/N)	86.46	-	-	[92]
x_3 (from 22^{o}C to T)	(%)	-	0.0831	0.1154	

Figure 5.1 shows the isothermal bipolar D-E loops taken at 22, 90, and 140^{o}C. The D-E loops at 22 and 90^{o}C featured high remnant and saturation polarizations, indicating that the sample was in a ferroelectric state. Interestingly, the D-E loop at 90^{o}C saturated at a displacement approximately 20% larger than that at 22^{o}C. The D-E loop at 140^{o}C showed double hysteresis characterized by paraelectric behavior (in pseudocubic phase) at low electric field and ferroelectric behavior at high electric field, due to field-induced phase transition.

Figure 5.1 also shows the Olsen cycles performed at 0.0173 and 0.0211 Hz for T$_C$=22^{o}C and T$_H$=140^{o}C while the electric fields were taken as E$_L$=0.2 MV/m and E$_H$=0.75 MV/m. The Olsen cycle was plotted in the D-E diagram by matching state 3 of the cycle with the D-E loop at 140^{o}C at electric field 0.75 MV/m, as performed by Olsen and Evans.[136] Indeed, only changes in displacement could be measured during the Olsen cycle and the isothermal bipolar D-E loop at T_{hot} typically overlaps well with that of process 3-4 in the Olsen cycle.[97,98] The two Olsen cycles shown in Figure 5.1 were performed consecutively on the same PMN-28PT sample. It should be noted that the results were repeatable from one cycle to another and among PMN-28PT samples as observed with PZN-5.5PT.[52]

The Olsen cycle performed at lower frequency followed the path of the isothermal D-E loops at 22 and 140^{o}C except during process 1-2 for electric fields between 0.65 and

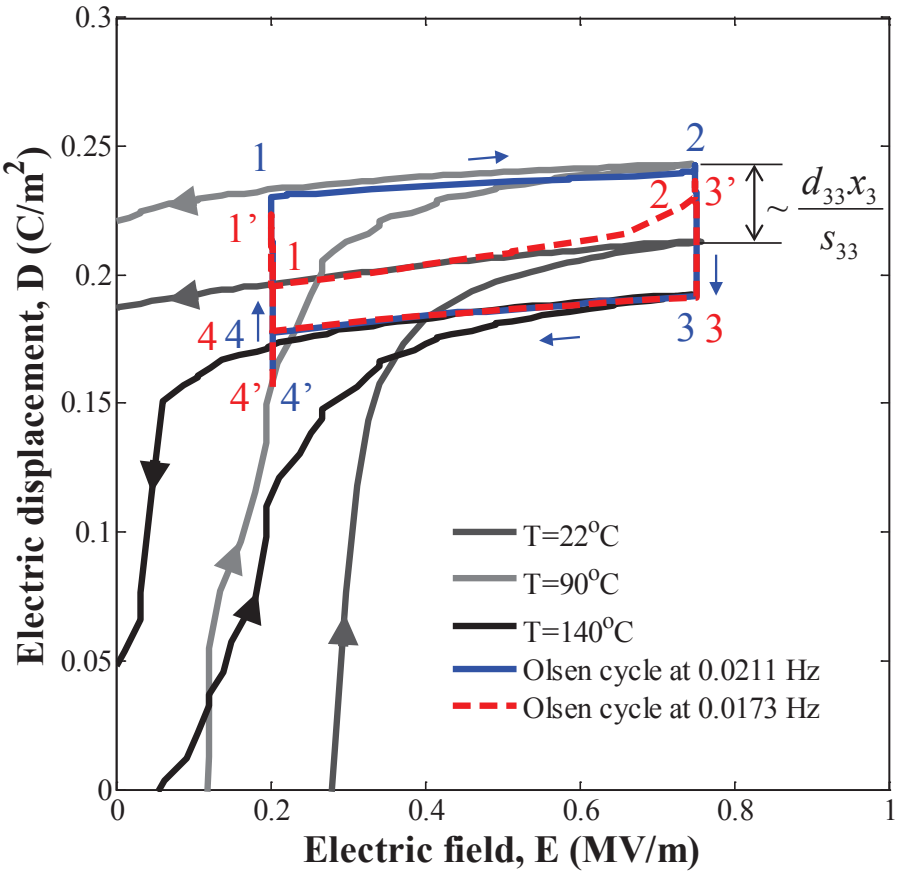

Figure 5.1: Isothermal bipolar D-E loops at T=22, 90, and 140^{o}C and experimental Olsen cycles at 0.0173 and 0.0211 Hz for PMN-28PT with E_L=0.2 MV/m, E_H=0.75 MV/m, T_C=22^{o}C, and T_H=140^{o}C.

0.75 MV/m. By contrast, the Olsen cycle performed at higher frequency extended beyond the electric displacement span of the isothermal D-E loops at 22 and 140^{o}C for the entire electric field span between E_L and E_H. This difference can be attributed to the fact that when process 1-2 was performed at higher frequency, the sample did not have time to reach the temperature of the oil bath during the cooling process 4-1 i.e., $T_{cold}>T_C$. In fact, the D-E loop at 90^{o}C was found to closely match the electric displacement of the Olsen cycle at 0.0211 Hz. Moreover, the Olsen cycle at 0.0173 Hz shown in Figure 5.1 features spikes at points 1, 2, and 3'. A similar spike at point 2 was observed by Olsen and Bruno[23] with

polyvinylidene fluoride. In addition, for both frequencies, points 4 and 4' did not fall on the same point due to leakage current through the sample at high temperature and electric field.[23,101] The following sections explain the physical phenomena responsible for the spikes observed in the lower frequency Olsen cycle.

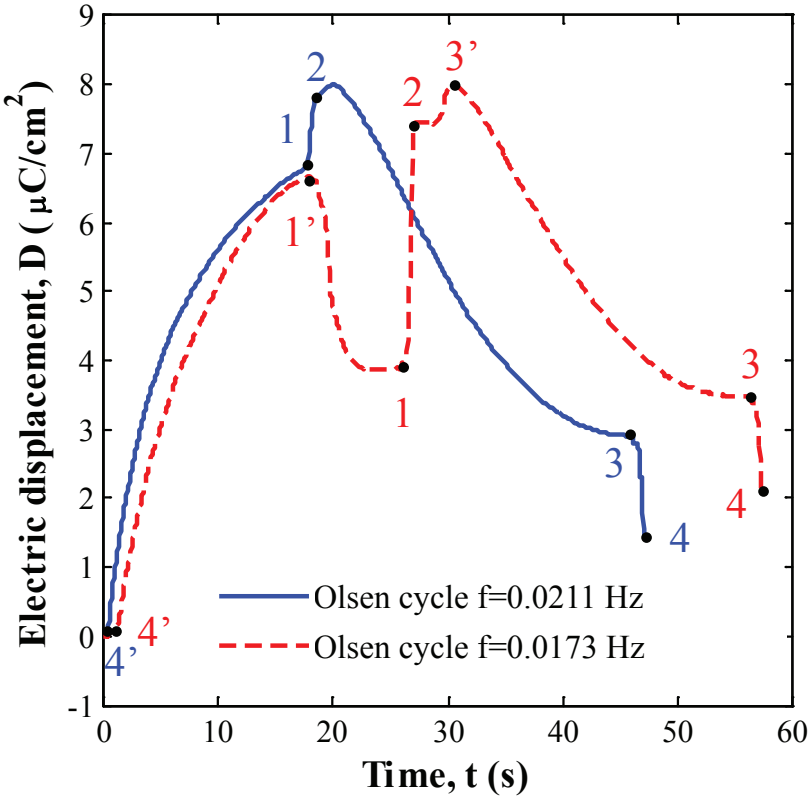

Figure 5.2: Measured electric displacement vs. time during the Olsen cycles at 0.0211 and 0.0173 Hz, respectively. Here, T_C=22^{o}C, T_H=140^oC, E_L=0.2 MV/m, and E_H=0.75 MV/m.

Figure 5.2 shows the electric displacement measured as a function of time for Olsen cycles performed at 0.0173 and 0.0211 Hz. States 1 through 4' correspond to those shown in Figure 5.1. Note that, for both frequencies, processes 1-2 and 3-4 were performed in 1.5 s while the heating time τ_{23} was 27 s. Thus, changes in the sample temperature during processes 1-2 and 3-4 were negligible compared with those in processes 2-3 and 4-1. For the lower frequency, the cooling time τ_{41} was identical to the heating time τ_{23}, i.e., τ_{41}=τ_{23}=27 s. However, it was

shorter ($\sim$ 17 s) for the higher frequency cycle. Thus, the sample temperature reached the hot bath temperature T_H = 140^{o}C for both frequencies but did not have time to reach the cold bath temperature T_C=22^oC for higher frequency. In the Olsen cycle performed at 0.0211 Hz, the electric displacement reached a maximum during the cooling process 4-1 immediately before performing the isothermal charging process 1-2. In this case, the duration of the cooling process 4-1 was 17 s. However, for the cycle performed at 0.0173 Hz, the sample was held in the cold bath at 22^{o}C for an additional 10 s for a total of 27 s before performing process 1-2. During this additional time, the material cooled down and depoled as a result of a phase transition, and the electric displacement reached a steady state around 4 μC/cm^2.

Figure 5.3 plots the Olsen cycles, performed in this study, in the E-T phase diagram of [001]-oriented PMN-28PT reported by Herklotz *et al.*[74] It also shows the crystalline structure of each phase and the corresponding polarization. The shaded region corresponds to conditions when the material has been electrically induced into a ferroelectric state but possesses electric displacements smaller than those of the tetragonal phase as discussed by Merz.[72] The E-T phase diagram suggests that during the cooling process 4-1 of the Olsen cycle at higher frequency of 0.0211 Hz, the material transitioned from a pseudocubic state at T_{hot}=T_H=140^{o}C to the highly-polarized tetragonal phase at T_{cold}=90^{o}C where it remained at state 1 (on blue cycle). Indeed, the sample did not have time to reach the cold bath temperature of T_C=22^{o}C. Instead, it reached about 90^{o}C, as suggested by the superposition of the D-E loop at 90^{o}C and process 1-2 of the Olsen cycle shown in Figure 5.1. This was corroborated by the lumped capacitance approximation presented in Appendix A.1. Thus, the sample retained the polarization generated by the pseudocubic to tetragonal phase transition at state 1. On the other hand, at lower cycle frequency of 0.0173 Hz, the polarization that appeared from the pseudocubic to tetragonal phase transition (state 1') disappeared during further cooling down to T_{cold}=T_C=22^{o}C as the sample underwent subsequent phase transitions to the less polarized monoclinic phases[74] where it remained at state 1.

Furthermore, at lower frequency, we speculate that the sample underwent a phase transi-

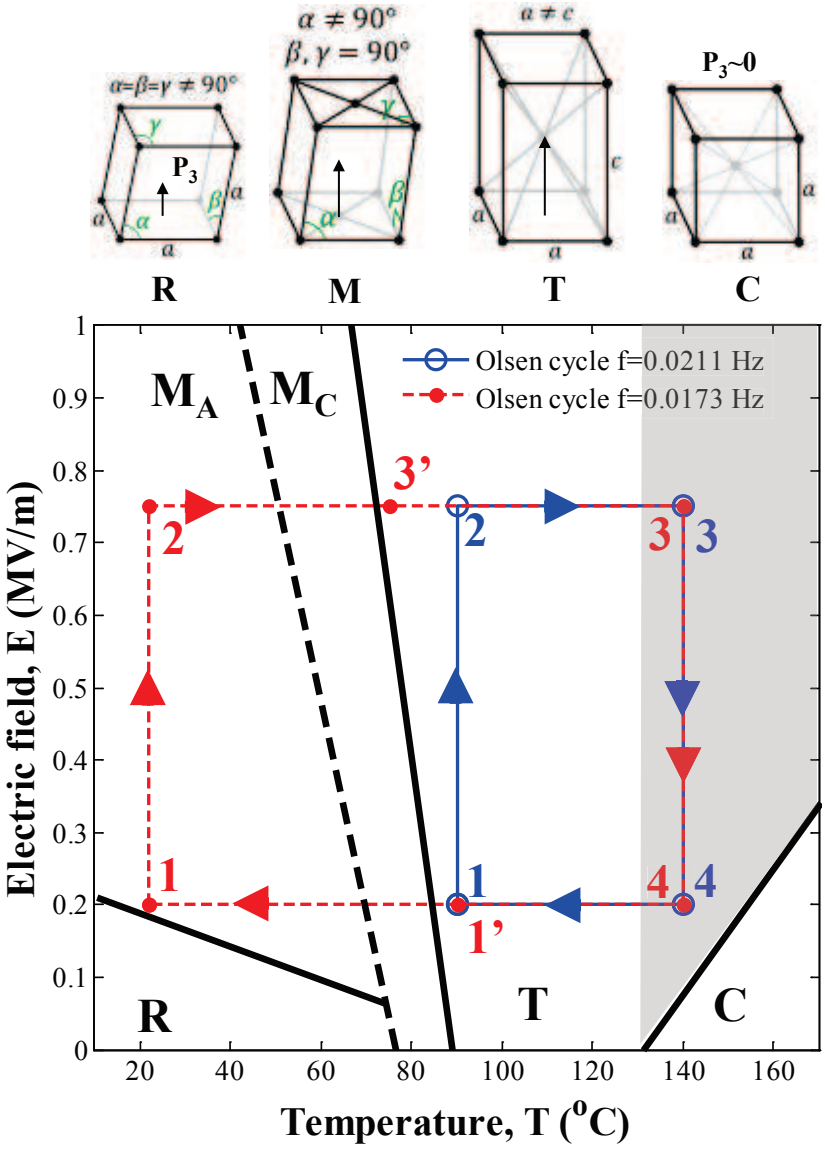

Figure 5.3: Olsen cycles performed at 0.0173 and 0.0211 Hz in the E-T diagram and phase boundaries for [001]-poled PMN-28PT (Ref.[74]). The M_A-M_C phase boundary (dashed line) was not always observed. The shaded region corresponds to electrically-induced ferroelectric state with polarizations smaller than that of the T phase (Ref.[72]).

tion from M_A to M_C phase during process 1-2 of the cycle. Then, the deviation of the Olsen cycle from the D-E loop at 22°C near state 2 (Figure 5.1) can be attributed to electric-field-induced phase transition from M_A to M_C phase. Indeed, the M_C phase is more polarized than

the M_A phase due to the continuous polarization rotation occurring between the rhombohedral and tetragonal phases.[95] Finally, the spike between states 2 and 3' can be attributed to the sample transitioning from the M_C phase to the tetragonal phase during the heating process 2-3 before transitioning to the pseudocubic phase at state 3 (Figure 5.3).

The energy density measured experimentally for the lower frequency Olsen cycle at 0.0173 Hz was 12.5 J/L. That predicted by Equation (2.12) using properties at T_C=22^{o}C and T_H=140^{o}C reported in Table 5.1 and ignoring the thermal expansion term was 11.5 J/L. For the higher frequency Olsen cycle at 0.0211 Hz, the measured energy density was 27.6 J/L. Equation (2.12) predicted an energy density of 28.9 J/L using properties at T_C=22^{o}C and T_H=140^{o}C and accounting for thermal expansion between 22 and 140^{o}C. The model predictions fell within 8.0% and 5.0% of the energy densities measured experimentally for the cycles at lower and higher frequency, respectively. This good agreement indicates that the additional energy density obtained at higher frequency can be attributed to the secondary pyroelectric effect accounted for by the thermal expansion term $d_{33}x_3/s_{33}$ estimated to be 0.033 C/m^2. In addition, Figure 5.1 suggests that the displacement in the D-E loop at 90^{o}C between states 1 and 2 is equal to that for 22^{o}C translated by a displacement $d_{33}x_3/s_{33}$ or $P_s(90^oC) = P_s(22^oC) + d_{33}x_3/s_{33}$ (see Figure 5.1). In fact, the difference between the upper portion of the D-E loops at 90^{o}C and 22^{o}C for electric field decreasing from E_H to E_L was 0.034±0.003 C/m^2 and fell within 2.9% of the value of $d_{33}x_3/s_{33}$. Consequently, using the properties $\varepsilon_r(T)$ and $P_s(T)$ in Table 5.1 between T_{cold}=90^{o}C and T_{hot}=140^{o}C and ignoring thermal expansion in Equation (2.12) predicted an energy density of 29.9 J/L which fell within 8.4% of that measured experimentally at 0.0211 Hz. These results demonstrate that the D-E loops at the actual sample temperatures include the contribution of the secondary pyroelectric effect. Thus, if the actual sample temperature is known, the thermal expansion term in Equation (2.12) should be ignored in predicting the energy density.

All pyroelectric materials are also piezoelectric and a positive thermal expansion corresponds to a positive change in polarization within the material as described by the secondary pyroelectric coefficient. Thus, performing the Olsen cycle on PMN-28PT between the tetrag-

onal and pseudocubic phases, when the thermal expansion is entirely positive during cooling, resulted in larger energy density than when cooling from the pseudocubic to the monoclinic phase region, when negative thermal expansion takes place. Thus, higher energy density was achieved at higher cycle frequency by limiting the temperature swing and the phase transition from the tetragonal to the pseudocubic phase. In addition, the combination of larger energy density and higher cycle frequency resulted in larger power density. Performing the Olsen cycle at higher frequency also reduced the thermal stress on the samples which could increase their lifetime.

This interpretation was also valid for results reported for PMN-32PT,[97] PZN-5.5PT,[52] and 8/65/35 PLZT.[98] Indeed, Kandilian *et al.*[97] performed the Olsen cycle on [001]-oriented PMN-32PT with cold source temperature T_C=80^{o}C and E_L=0.2 MV/m. These conditions were near the phase boundary between tetragonal and M_C phases of PMN-32PT estimated to be at 0.2 MV/m and 85^{o}C.[117] At 80^{o}C, the material was likely in the M_C phase featuring a polarization smaller than that of the tetragonal phase. However, for the cycle frequency considered, the samples' temperature did not fall below 85^{o}C during the Olsen cycle. In fact, Kandilian *et al.*[97] performed process 1-2 as soon as the electric displacement had reached a maximum. This was identical to the way the Olsen cycle at 0.021 Hz in the present study was performed. Thus, the samples did not undergo the tetragonal to monoclinic M_C phase transition. Then, the presence of the tetragonal phase and the associated large polarization caused the electric displacement span in the Olsen cycle to extend beyond that of the isothermal bipolar D-E loop at 80^{o}C.[97] Finally, the energy density of the Olsen cycle could be predicted by accounting for the secondary pyroelectric coefficient in Equation (2.12) using T_C=80^{o}C and T_H=130 and 140^{o}C.[97]

The Olsen cycle performed on PZN-5.5PT was characterized by sample temperature larger than 100^{o}C[52] corresponding to the tetragonal phase for all electric fields considered according to the PZN-4.5PT phase diagram.[86] Similarly, for Olsen cycles performed on 8/65/35 PLZT ceramics with T_C equal to 45 and 65^{o}C,[98] the samples remained in the ferroelectric phase away from any phase boundaries.[98] Thus, in absence of phase boundaries

near T_C and E_L, thermal expansion did not contribute significantly to energy generation and could be ignored in the physical model given by Equation (2.12). This resulted in good predictions of the experimental data.[52,98]

5.4 Chapter summary

The Olsen cycle was performed on [001]-oriented PMN-28PT single crystals for two different cycle frequencies, namely 0.0173 and 0.0211 Hz. The electric field was cycled between E_L=0.2 and E_H=0.75 MV/m and the samples were alternately dipped in silicone oil baths at T_C=22^{o}C and T_H=140^{o}C. A significant increase in measured energy density from 12.5 to 27.6 J/L was obtained at higher frequency. This was caused by a phase transition from the pseudocubic phase to the strongly polarized tetragonal phase during cooling process 4-1. At lower cycle frequency, the material had time to cool down to a lower temperature and underwent a second phase transition from tetragonal to the less polarized monoclinic M_A phase. Then, the thermal expansion did not contribute to the energy density generated. These results and interpretation were in excellent agreement with the predictions of the physical model derived by Kandilian *et al.*[97] and with experimental data collected for PMN-32PT,[97] PZN-5.5PT,[52] and 8/65/35 PLZT.[98]

Overall, in order to maximize the energy density of the Olsen cycle while maintaining a large power density, E_L and T_{cold} should be chosen so that the material exhibits the highest electric displacement. This is not necessarily achieved by maximizing (T_{hot}-T_{cold}). Instead, the material should undergo a single phase transition resulting in the highest change in polarization. In the case of PMN-28PT and PMN-32PT, this corresponds to the transition from the pseudocubic to the tetragonal phase.

CHAPTER 6

A Novel Thermomechanical Energy Conversion Cycle

This chapter aims to demonstrate the feasibility of a novel power cycle performed on pyroelectric materials to convert both thermal and mechanical energies directly into electrical energy. It was demonstrated on [001]-poled PMN-28PT single crystals. This cycle takes advantage of the fact that phase transitions can be induced by both heat and compressive stress. It aims to be more versatile than the Olsen cycle and to achieve large power densities by increasing the cycle frequency. In addition, it aims to achieve larger material efficiencies than the Olsen cycle by reducing the thermal energy consumed during the cycle.

6.1 Introduction

Pyroelectric materials possess a temperature-dependent spontaneous polarization. They are also piezoelectric, meaning the electric charge at the material surface changes when the material is mechanically deformed. Therefore, applying a compressive stress in the poling direction decreases the electric displacement for a given temperature and electric field. The reduction in surface charge results in current in the external load. Figures 6.1a and 6.1b show the isothermal D-E loops exhibited by a typical pyroelectric material at two different temperatures T_{cold} and T_{hot} under compressive stress σ equal to 0 and σ_H. Figure 6.1a also shows the Olsen cycle previously described in Chapter 2 Section 2.3.4 in the D-E diagram for σ=0 MPa. The Olsen cycle has been demonstrated to produce the largest energy densities of any power cycle performed on ferroelectric materials.[50] However, the Olsen cycle performed on a given material requires the hot source temperature to be larger than T_{Curie} in order to generate energy. Moreover, the power density of the Olsen cycle is limited by the low

cycle frequency due to slow heat transfer and relaxation processes. The energy and power densities generated by a pyroelectric material undergoing the Olsen cycle could be increased by increasing the electric displacement span between temperatures T_{cold} and T_{hot}. This can be achieved by subjecting the sample to compressive stress. This is particularly true at temperatures around T_{Curie}.

Here, we present a new cycle using uniaxial compressive stress in addition to thermal and electric field cycling. It circumvents the above mentioned difficulties of the Olsen cycle to increase both energy and power densities (i) by combining piezoelectric and pyroelectric energy conversion and (ii) by increasing the cycle frequency by quickly forcing the material into a specific state using mechanical stress instead of heating and cooling which are inherently slow.

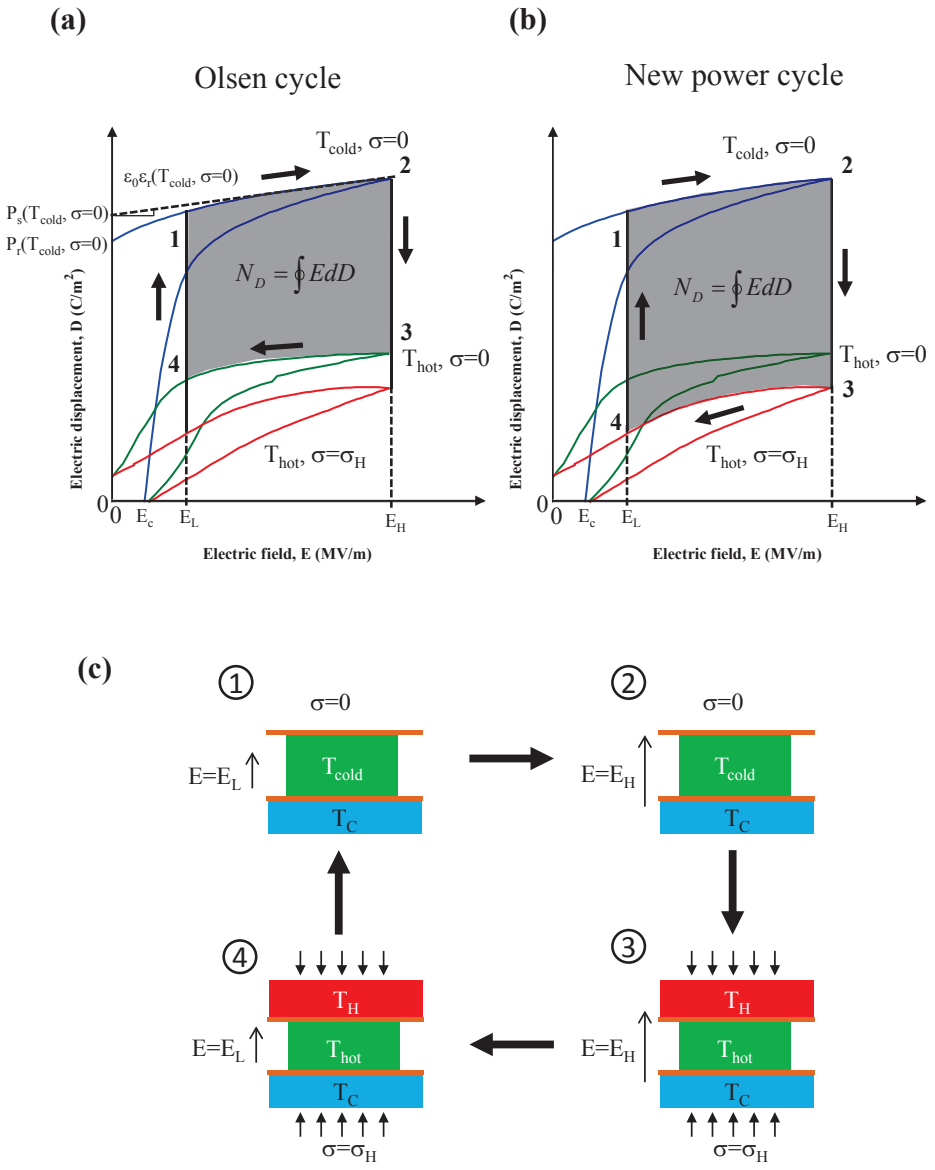

Figure 6.1: Two-dimensional projections of (a) the Olsen cycle and of (b) the new power cycle in the D-E plane as well as electric displacement versus electric field loops at T_{cold} for uniaxial stress σ=0 and T_{hot} for σ=0 and σ_H. The electrical energy generated per cycle is represented by the grey areas enclosed by states 1-2-3-4. (c) The thermal, electrical, and stress states of the ferroelectric sample at each state of the new power cycle.

6.2 New thermomechanical power cycle

6.2.1 Principle

Figure 6.1b illustrates the new power cycle projected onto the D-E plane overlaid with the corresponding isothermal bipolar hysteresis curves (D-E loops) at cold temperature T_{cold} under zero stress and at hot temperature T_{hot} under compressive stress σ_H. Figure 6.1c schematically illustrates the practical implementation of the new power cycle and the stress, temperature, and electric field imposed in each state. Process 1-2 consists of an isothermal increase in electric field from E_L to E_H at T_{cold} in the absence of compressive stress. Process 2-3 corresponds to simultaneously compressing the sample at σ_H and heating it up to T_{hot}. Process 3-4 consists of an isothermal decrease in electric field from E_H to E_L at T_{hot} under compressive bias stress σ_H. Finally, process 4-1 closes the cycle by simultaneously cooling the sample to T_{cold} and removing the loading under constant electric field E_L. The area enclosed by the four processes in the D-E diagram, shown in Figure 6.1b, corresponds to the generated energy density N_D defined by Equation (1.1). The overall cycle frequency (in Hz) is defined as $f = (\tau_{12} + \tau_{23} + \tau_{34} + \tau_{41})^{-1}$ with τ_{ij} corresponding to the duration of process i-j. This new cycle can be implemented using a procedure similar to the "stamping procedure" developed by Lee *et al.*[44] to perform the Olsen cycle but under significantly larger compressive stress. This was implemented experimentally to directly convert both thermal and mechanical energies into electrical energy using single crystal PMN-28PT.

6.2.2 Material efficiency

The material efficiency of a power cycle is typically defined as the ratio of the energy produced by the material to the energy consumed by performing the cycle. Overall, the material efficiency of the thermomechanical cycle can be expressed as

$$\eta = \frac{N_D}{Q_{in} + W_{in}} \tag{6.1}$$

where N_D is the electrical energy produced per unit volume of the material per cycle while Q_{in} and W_{in} are the thermal energy and mechanical work provided per unit volume of the material during the cycle. Similarly, the Olsen cycle material efficiency may be defined as $\eta_{Olsen} = N_D/Q_{in}$. The area enclosed by the cycle in the D-E diagram corresponds to the generated energy density per unit volume N_D and is given by Equation (1.1). The thermal energy consumed by the material during the cycle may be expressed, per unit volume, as

$$Q_{in} = \oint \rho c_p(T) \mathrm{d}T \tag{6.2}$$

where ρ and $c_p(T)$ are the density and specific heat of the ferroelectric material in kg/m^3 and J/kgK, respectively. The specific heat of ferroelectric materials $c_p(T)$ is temperature-dependent and can be measured by differential scanning calorimetry[130] as discussed in Chapter 4 Section 4.3.3. The mechanical work W_{in} per unit volume of material can be expressed as

$$W_{in} = \oint \sigma(x_3) \mathrm{d}x_3 \tag{6.3}$$

where x_3 represents the strain in the longitudinal direction parallel to the polarization. For ferroelectric materials undergoing phase transitions, the relationship between σ and x_3 is typically non-linear.[113,137] Thus, W_{in} cannot be expressed in terms of the Young's modulus. Instead, it should be estimated from stress-strain curves.[138] Note that the material efficiency defined above accounts for the conversion of thermomechanical energy into electricity by the material itself. It does not represent the efficiency of a potential device implementing the cycle and subject to heat losses, friction, and other irreversible processes. In other words, η represents the upper limit of a device efficiency.

6.3 Materials and methods

6.3.1 Samples

Single crystal PMN-28PT was chosen for its advantageous piezoelectric properties in a broad temperature range.[92] The PMN-28PT samples used in this study were similar to those described in Chapter 4 Section 4.3.1.

6.3.2 Experimental setup

The experimental setup consisted of an electrical and a thermomechanical subsystem. The electrical subsystem was a Sawyer-Tower circuit identical to that used in our previous studies[52,97–101] and presented in Chapter 2 Section 2.3.4. Figures 6.2a and 6.2b show a schematic and a photograph of the thermomechanical subsystem used to perform the novel power cycle, respectively. This subsystem consisted of a spring return air cylinder (McMaster-Carr 6498K252) vertically actuated using compressed air at a maximum pressure of 469 kPa. A 24 V DC solenoid valve was used to control the extension and contraction of the cylinder rod. A 100-Watt cartridge heater was imbedded in a 1.27 cm thick aluminum plate serving as a heat source. A type-K thermocouple was embedded at the center of this heating block whose temperature was maintained at T_H with an Omega CN-7823 proportional integral derivative (PID) temperature controller. The PMN-28PT sample was sandwiched between two copper tapes used to provide electrical contact between the sample's electrodes and the wires. This assembly was placed on top of a 5 mm thick steel die. An aluminum heat sink (Cool Innovations 3-151514M) was placed in thermal contact with the steel die by epoxy adhesive OMEGABOND® 200 to passively cool the pyroelectric sample to T_{cold} during process 4-1. A 140 μm thick Kapton film was used to electrically isolate the sample's electrodes from the metallic heat source and sink. Note that the sample temperature could not be measured during electric field cycling due to electrical conduction between the sample and the thermocouple.

This setup was modified slightly when collecting isothermal D-E loops under different compressive stresses. Then, the heat sink and steel die were replaced with an aluminum heating plate and wood block identical to the heat source placed above the sample. This was done to ensure the sample was uniformly heated to T_{hot} from both sides and to minimize the temperature gradient in the sample. In this case, a type-K thermocouple placed directly on the sample was used to measure the sample temperature. It was removed before electric field cycling began.

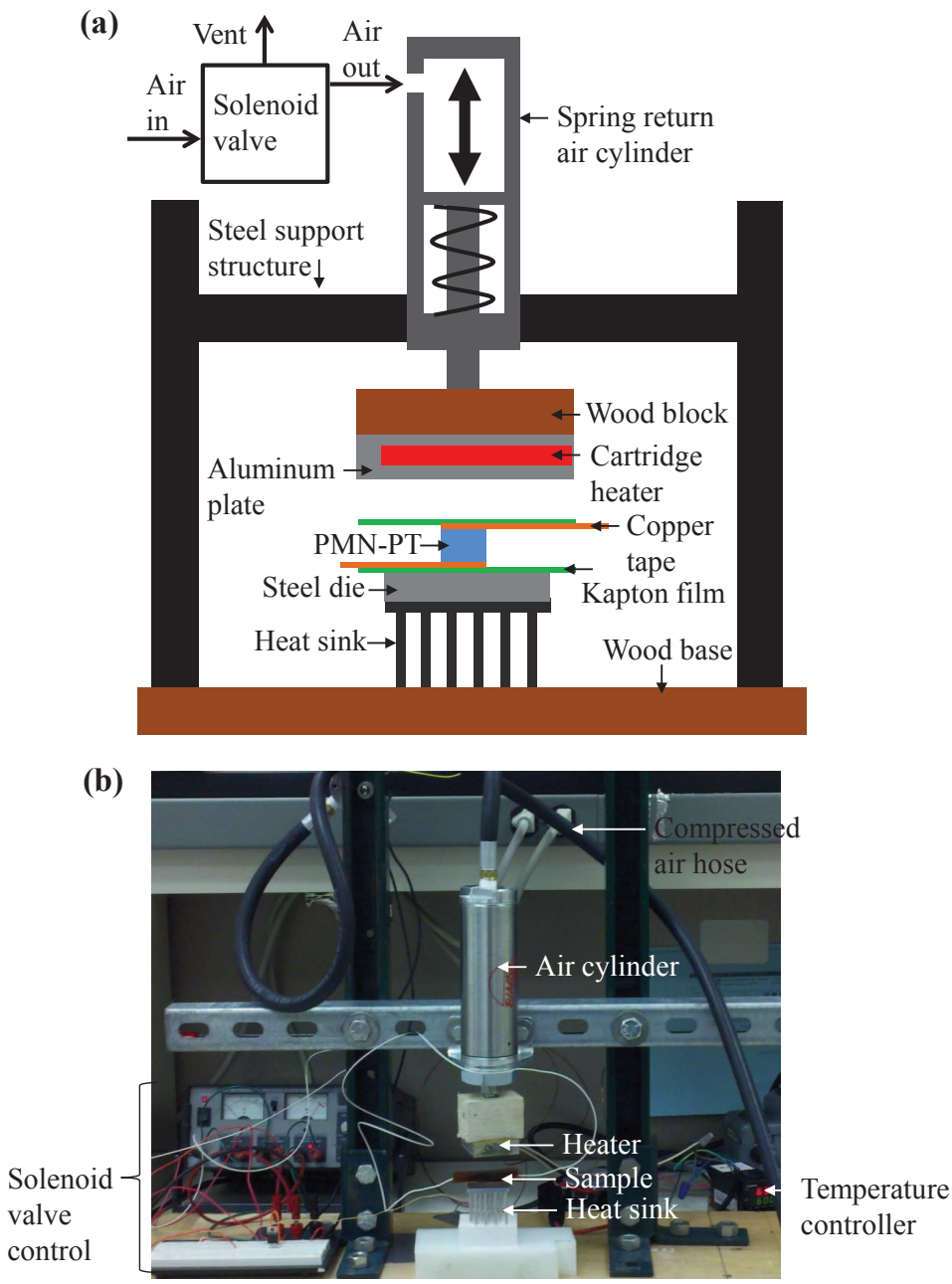

Figure 6.2: (a) Schematic and (b) photograph of the thermomechanical subsystem used to create the periodic temperature oscillations and to apply compressive stress during the new thermoelectromechanical power cycle depicted in Figure 6.1b. Dimensions in (a) are not to scale.

6.3.3 Experimental procedure

Isothermal D-E loops under different compressive stresses were collected and the new power cycle was performed on the PMN-28PT samples using the above-described experimental setup. For comparison purposes, the Olsen cycle was also performed using "dipping experiments" and the experimental setup described in Refs.[97,101] and in Chapter 2 Section 2.3.4.

6.3.3.1 Isothermal D-E loops

Isothermal bipolar D-E hysteresis loops were collected on the samples for temperature ranging between 22 and 170^{o}C and compressive stress varying from 0 to 25.13 MPa. These measurements were taken by applying a triangular voltage signal at 0.1 Hz across the single crystal samples. The amplitude of the applied voltage corresponded to an electric field varying from -0.75 to 0.75 MV/m. All measurements were repeated three times to assess repeatability and to estimate the experimental uncertainty.

6.3.3.2 New power cycle

The new power cycle was performed so that the duration of each process was $\tau_{23} = \tau_{41}$ and $\tau_{12} = \tau_{34} = \tau_{23}/7$. It was executed for frequency ranging from 0.025 to 1 Hz by varying τ_{23} between 17.5 and 0.438 seconds. The high electric field E_H varied from 0.75 to 0.95 MV/m while T_H varied from 60 to 217^{o}C, and the uniaxial stress σ_H applied during processes 2-3 and 3-4 ranged from 0 to 33.56 MPa. The low electric field E_L was fixed at 0.2 MV/m. The cold source temperature T_C was passively maintained near room temperature around 22^{o}C and never exceeded 30^{o}C. In addition, thermomechanical cycling was performed without electric field cycling for the above conditions on one of the samples in order to calibrate the sample temperature oscillations for different frequencies and hot source temperature T_H. To do so, a type-K thermocouple was bonded with OMEGABOND® 101 to the center of one of the 3×5 mm^2 faces.

6.3.3.3 Olsen cycle

The Olsen cycle was performed to achieve the maximum energy density with cold source temperature T_C set at 22^{o}C and hot source temperature T_H ranging from 80 to 170^{o}C. The electric fields E_L and E_H were fixed at 0.2 and 0.75 MV/m, respectively. The cycle frequency f was dependent on T_H based on the amount of time necessary for the sample's electric displacement to reach a minimum or maximum during the heating and cooling processes, respectively. Note that the maximum energy density for [001] PMN-28PT undergoing the Olsen cycle has previously been achieved with sample temperature T_{cold}=90^{o}C.[100] For both cycles, the energy density generated per cycle N_D was evaluated by numerically integrating experimental data for D vs. E according to Equation (1.1) using the trapezoidal rule.

6.4 Results and discussion

6.4.1 Isothermal bipolar D-E loops

Figure 6.3 plots the isothermal bipolar D-E loops measured at 0.1 Hz at temperature (a) 22, (b) 80, (c) 140, and (d) 150^{o}C and under mechanical loading varying between 0 and 25.13 MPa. It illustrates the effect of compressive stress on the D-E loops. The isothermal D-E loops were closed and consecutive D-E loops overlapped for any temperature and compressive stress considered. This indicates that leakage current through the sample was negligibly small. The non-linearity in D-E loops, observed as the electric field was reduced from 0.75 to 0.0 MV/m under zero stress, corresponded to electric field induced phase transitions.[72] According to the E-T phase diagram at 10 Hz,[74] tetragonal to monoclinic M$_C$ phase transition occurs at 80^{o}C and 0.4 MV/m. Similarly, the tetragonal to cubic phase transition at temperature 140, 150, and 160^{o}C occurred at electric fields 0.1, 0.18, and 0.25 MV/m, respectively.[74] At T=170^{o}C, the sample remained in the paraelectric pseudocubic phase for all electric fields considered and compressive stress had negligible effect on the D-E loops (not shown).

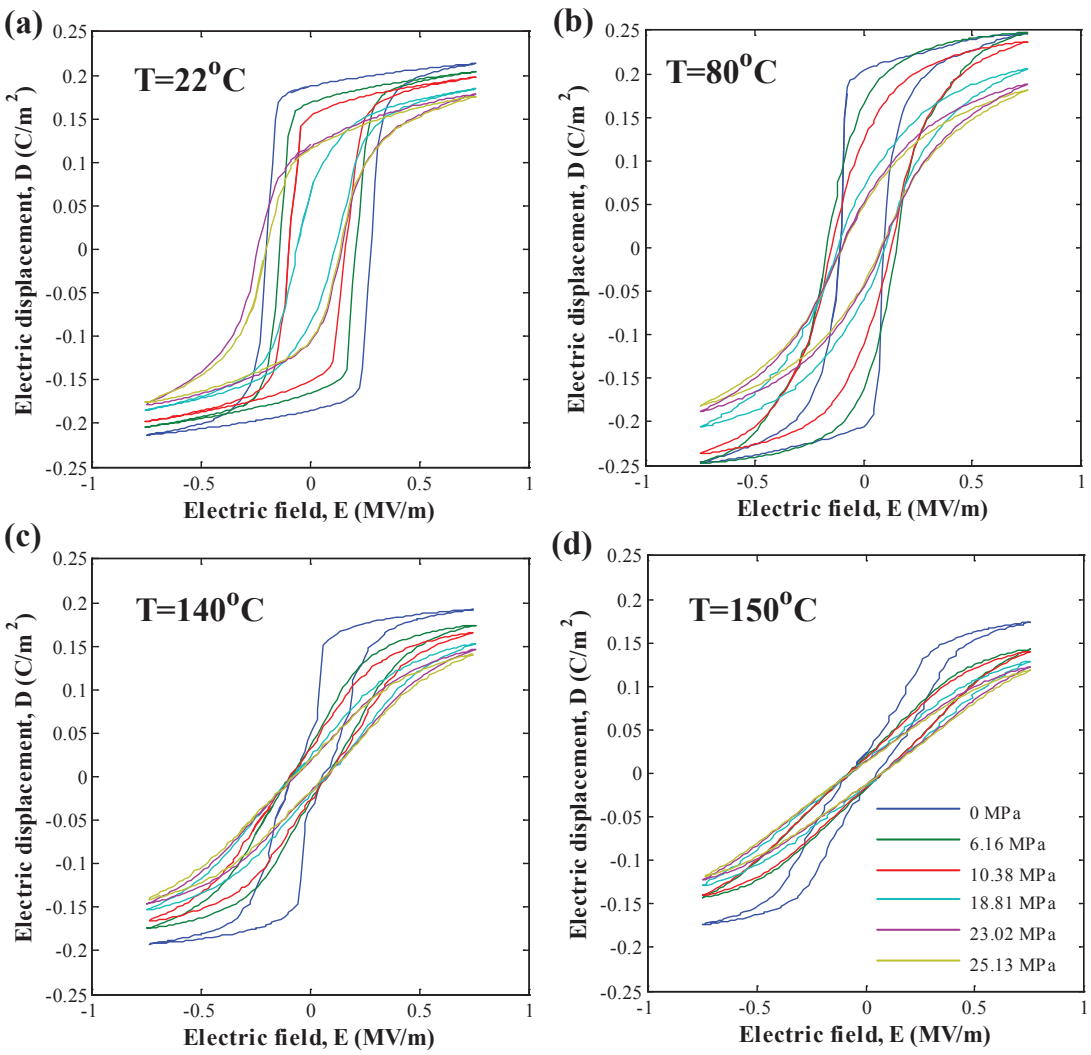

Figure 6.3: Isothermal bipolar D-E loops of PMN-28PT Sample 1 at 0.1 Hz for temperatures (a) 22, (b) 80, (c) 140, and (d) 150^{o}C and compressive stress σ between 0 and 25.13 MPa.

6.4.2 Sample temperature calibration

Figures 6.4a to 6.4d show the sample temperature oscillations as a function of time for different heater temperatures T_H varying from 80 to 200^{o}C measured at 0.025, 0.125, 0.5, and 1 Hz, respectively. For all heater temperatures, the sample temperature took around 40 seconds to reach oscillatory steady-state. For a given frequency, the peak to peak temperature

span and the maximum and minimum sample temperatures T_{hot} and T_{cold} increased with increasing heater temperature T_H. Figures 6.5a and 6.5b show the sample temperature calibration for sample temperatures T_{hot} and T_{cold} as a function of heater temperature T_H for frequency varying from 0.025 to 1 Hz. Each data point corresponds to the arithmetic mean of T_{hot} and T_{cold} measured over five consecutive cycles in the oscillatory steady-state regime. The solid lines correspond to the linear fit of T_{hot} or T_{cold} versus T_H (in ^{o}C) for a given frequency. This fit was used to compute T_{hot} or T_{cold} for a given heater temperature and cycle frequency. In addition, the sample cold temperature T_{cold} increased with increasing T_H and frequency. In fact, the difference between T_{hot} and T_{cold} decreased as the frequency increased to nearly vanish at 1 Hz. Furthermore, the sample temperature was found to be independent of compressive stress for any given heater temperature. Note that in the D-E loop experimental setup where the sample was heated from both top and bottom, its temperature was approximately 27^{o}C less than the heater temperature under steady-state conditions due to the low thermal conductivity ($\sim$0.12 W/m K) of the electrically insulating Kapton film.

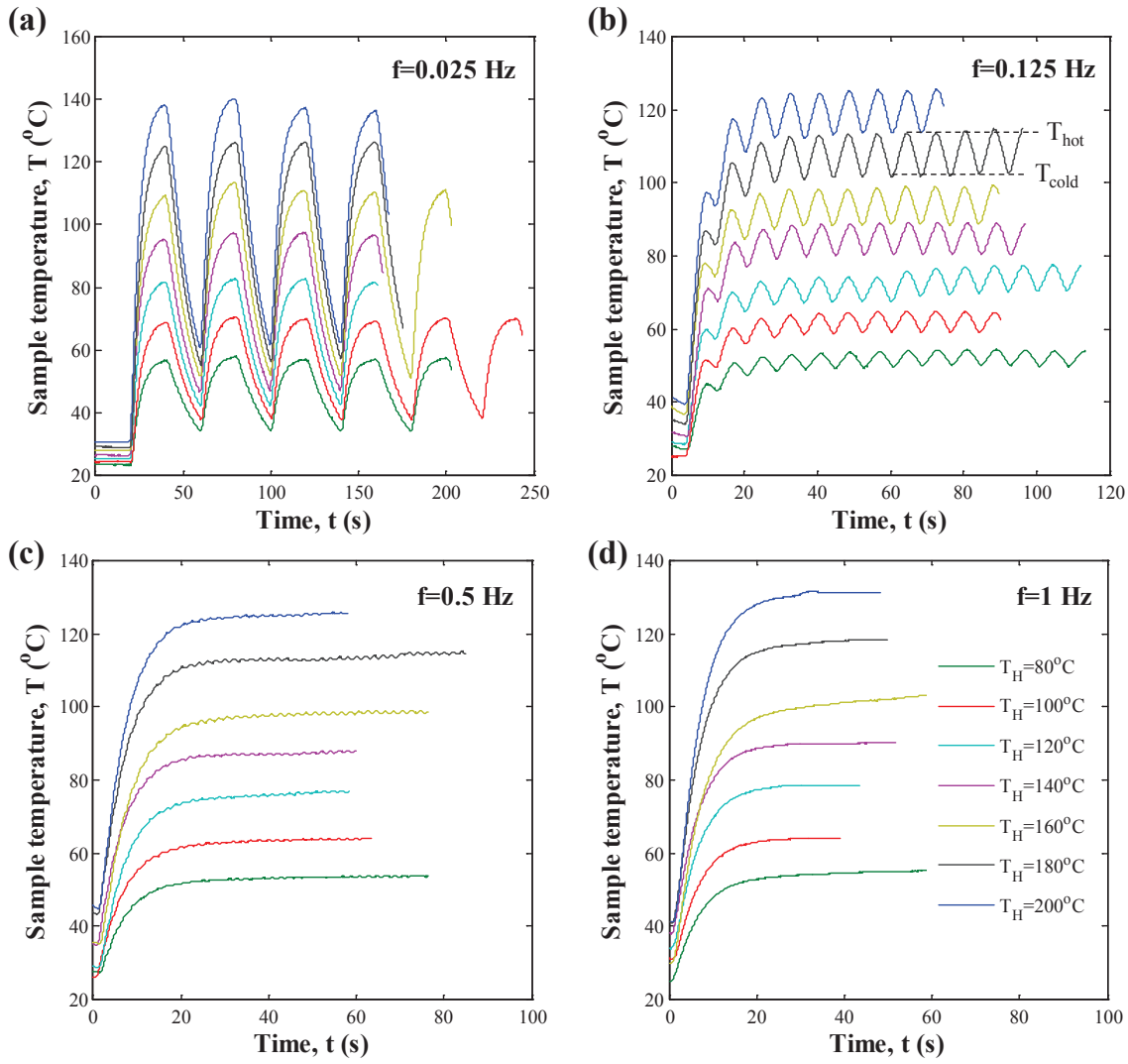

Figure 6.4: (a) Sample temperature as a function of time for the new cycle performed at (a) 0.025 Hz, (b) 0.125 Hz, (c) 0.5 Hz, and (d) 1 Hz.

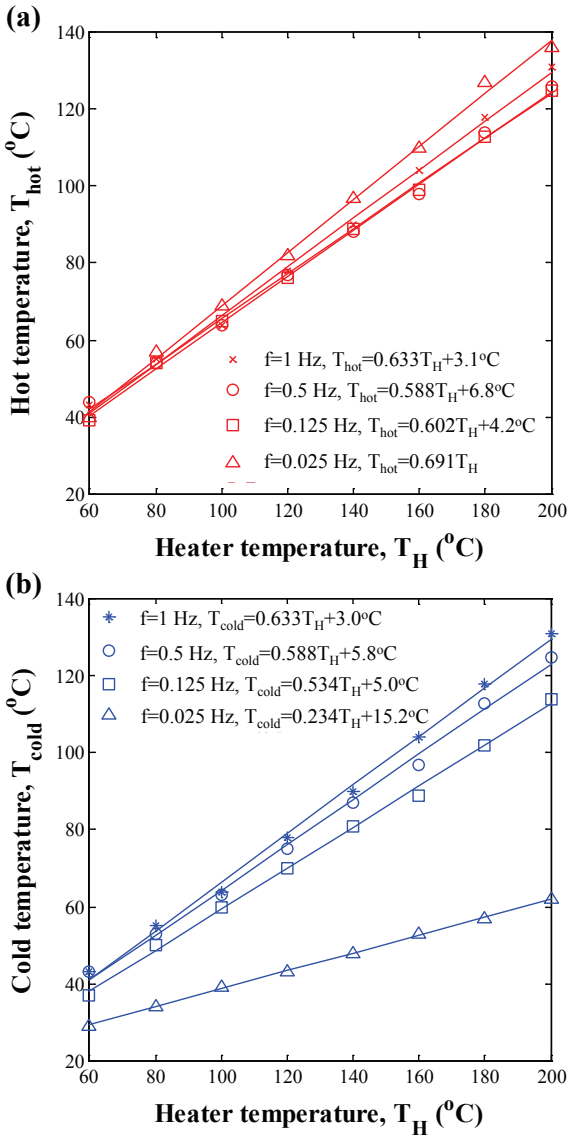

Figure 6.5: Calibration curves for maximum and minimum sample temperatures (a) T_{hot} and (b) T_{cold} as functions of heater temperature T_H for frequency varying from 0.025 to 1 Hz. The lines correspond to linear fits of the experimental data for a given f.

6.4.3 Power cycle energy density comparison

Figures 6.6a and 6.6b depict, in the D-E diagram, the new thermomechanical power cycle performed at 0.025 Hz between temperatures T_C=22^{o}C and T_H=157^{o}C or T_H=187^{o}C corre-

sponding to (a) T_{cold}=52^{o}C and T_{hot}=109^{o}C or (b) T_{cold}=59^{o}C and T_{hot}=129^{o}C, respectively. For both cycles, the electric field was cycled between E_L=0.2 MV/m and E_H=0.75 MV/m. A compressive stress of σ_H=18.81 MPa was applied during processes 2-3 and 3-4. Based on sample temperature calibration curves (Figure 6.5), the sample did not reach the cold source temperature of 22^{o}C, and instead, cooled to approximately 52 and 59^{o}C during process 4-1 before process 1-2 was performed. Figure 6.6 also shows the isothermal bipolar D-E loops previously collected at temperatures near T_{hot} and T_{cold} and under compressive stress 0 and σ_H. The power cycles shown were vertically translated to match the electric displacement of the D-E loop for T_{hot} and σ_H at E_H (state 3) as performed by Olsen and Evans.[136] The new power cycles shown in Figures 6.6a and 6.6b generated energy densities of 24.0 and 33.6 J/L, respectively. The Olsen cycle performed under similar operating temperatures and electric fields would yield much smaller energy densities considering the area bounded by the D-E loops at temperatures T_{cold} and T_{hot}.[100] In fact, it is evident that for T_{cold}=52^{o}C and T_{hot}=109^{o}C (6.6a), the Olsen cycle would generate no energy. For T_{cold}=59^{o}C and T_{hot}=129^{o}C, the Olsen cycle would generate approximately half of the energy density of the new cycle.

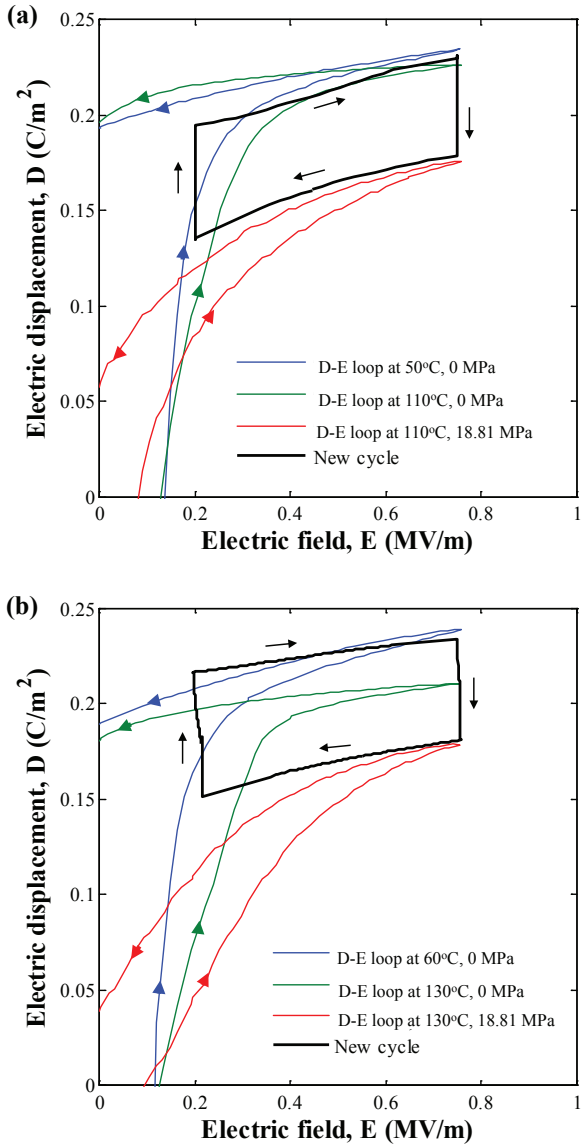

Figure 6.6: Isothermal bipolar D-E loops and experimental power cycles for PMN-28PT for electric field between E_L=0.2 MV/m and E_H=0.75 MV/m and temperatures between (a) T_{cold}=52^{o}C and T_{hot}=109^{o}C or (b) T_{cold}=59^{o}C and T_{hot}=129^{o}C. The power cycles were performed at frequency f=0.025 Hz. State 3 of the power cycles were vertically displaced to match the corresponding D-E loop at T_{hot} and E_H. The compressive stress applied during processes 2-3 and 3-4 was equal to 18.81 MPa.

Figure 6.7 plots the energy density experimentally generated (i) by the new thermomechanical power cycle at frequency 0.025 Hz and (ii) by the Olsen cycle for T_{cold}~90^{o}C at frequency ranging from 0.013 to 0.021 Hz as a function of temperature T_{hot} varying between 80 and 170^{o}C. Note that data for the Olsen cycle corresponded to the maximum energy density.[100] Each data point represents an average over four cycles and the error bars correspond to one standard deviation or 63% confidence interval. The Olsen cycle was performed using the dipping method[101] on the same PMN-28PT sample used to perform the new cycle. The error bars associated with the Olsen cycle were larger because it was not automated, unlike the new cycle. Figure 6.7 shows that, for T_{hot} between 80 and 150^{o}C, the energy density generated by the new power cycle was larger than that generated by the Olsen cycle. In fact, the Olsen cycle did not generate positive energy density for T_{hot} below 130^{o}C. However, it generated the largest energy density of 85.9 J/L/cycle at T_H=T_{hot}=170^{o}C. Similarly, the energy density obtained with the new power cycle increased with increasing T_{hot} and reached a maximum of 42.6 J/L/cycle for T_{hot}=150^{o}C.

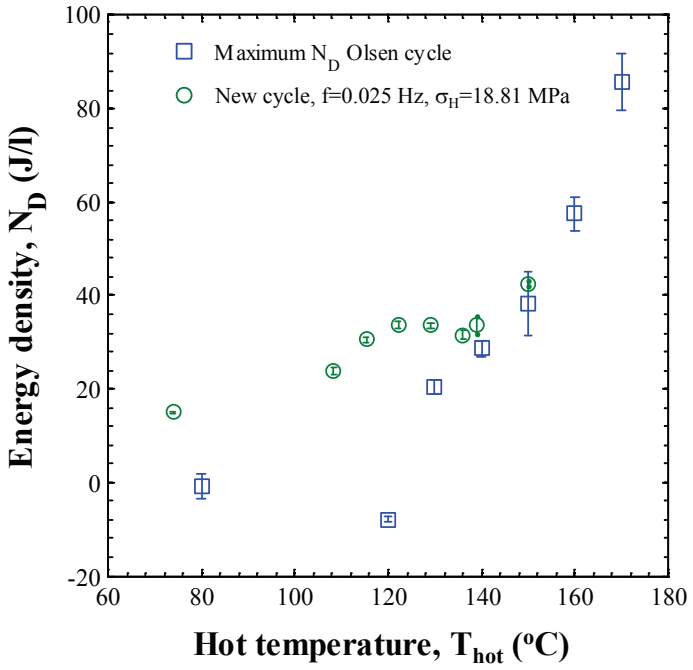

Figure 6.7: Experimentally measured energy density generated with PMN-28PT as a function of hot temperature T_{hot} for maximum energy density Olsen cycles and new power cycles at 0.025 Hz. The Olsen cycle was performed with zero compressive stress (σ_H=0 MPa) and the new power cycle was performed with σ_H=18.81 MPa. For all cycles T_C=22^{o}C, E_L=0.2 MV/m, and E_H=0.75 MV/m.

6.4.4 Effect of compressive stress and temperature

Figure 6.8 shows the generated energy density of the new thermomechanical power cycle as a function of applied compressive stress σ_H for heater temperatures T_H varying between 60 and 170^{o}C. Here, the frequency was fixed at 0.125 Hz while the electric field was cycled between E_L=0.2 MV/m and E_H=0.75 MV/m. It is evident that the energy density increased nearly linearly with increasing σ_H for any given heater temperature T_H. It also increased slightly with increasing heater temperature up to T_H=160^{o}C. For this heater temperature and frequency, the sample temperature T_{cold} was 90^{o}C, corresponding to the temperature

at which [001] PMN-28PT was in the tetragonal phase and exhibited the highest saturation polarization under zero stress.[100] On the other hand, for T_H=170^{o}C and f=0.125 Hz, T_{cold} was 96^{o}C, corresponding to the beginning of relaxation into the pseudocubic phase featuring a smaller saturation polarization. Therefore, the energy density generated at 0.125 Hz for a given compressive stress was the largest for T_H=160^{o}C.

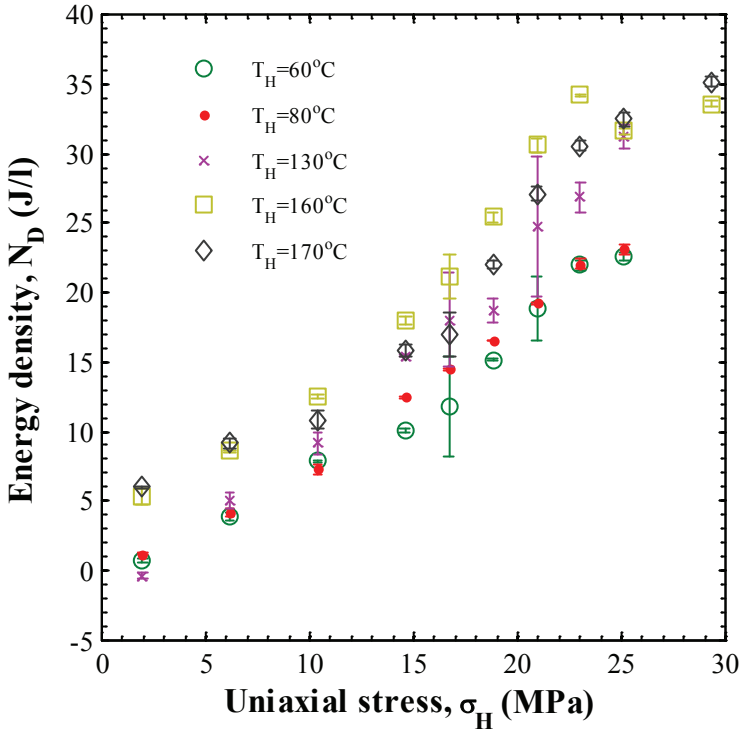

Figure 6.8: Experimentally measured energy density generated by performing the new thermomechanical power cycle on PMN-28PT as a function of compressive stress. The heater temperature T_H varied from 60 to 170^{o}C while T_C=22^{o}C, f=0.125 Hz, E_L=0.2 MV/m, and E_H=0.75 MV/m.

6.4.5 Effect of frequency

Figure 6.9a shows the energy density generated using the new power cycle as a function of heater temperature T_H for frequency 0.125, 0.5, and 1 Hz. The applied compressive stress

σ_H was fixed at 25.13 MPa, the low and high electric fields E_L and E_H were respectively set at 0.2 and 0.75 MV/m, and the cold source temperature T_C was 22^{o}C. It is evident that the energy density increased with increasing heater temperature for any given frequency. In addition, it decreased only slightly with increasing cycle frequency. This was due to the fact that the change in electric displacement as a result of a change in compressive stress (process 2-3) occurred quickly and was nearly similar for all frequencies. Furthermore, longer heating and cooling durations τ_{23} and τ_{41} at lower cycle frequency allowed the slow thermal relaxation processes to take place. This enabled more charge to build up at the electrode surfaces during process 4-1 resulting in the largest N_D generated for T_H above 110^{o}C at 0.125 Hz. In fact, the difference between T_{cold} and T_{hot} was around 10^{o}C at 0.125 Hz, while it was less than 1^{o}C at higher cycle frequency.

Figure 6.9b shows the power density generated by the new power cycle as a function of heater temperatures T_H corresponding to the data shown in Figure 6.9a. It is evident that increasing the cycle frequency resulted in significantly larger power density. In fact, the power density P_D ($=N_D f$) at 1 Hz was nearly ten times larger than that at 0.125 Hz for heater temperature T_H above 100^{o}C. This can be attributed to the fact that N_D did not decrease significantly as the frequency increased from 0.125 to 1 Hz (Figure 6.9a).

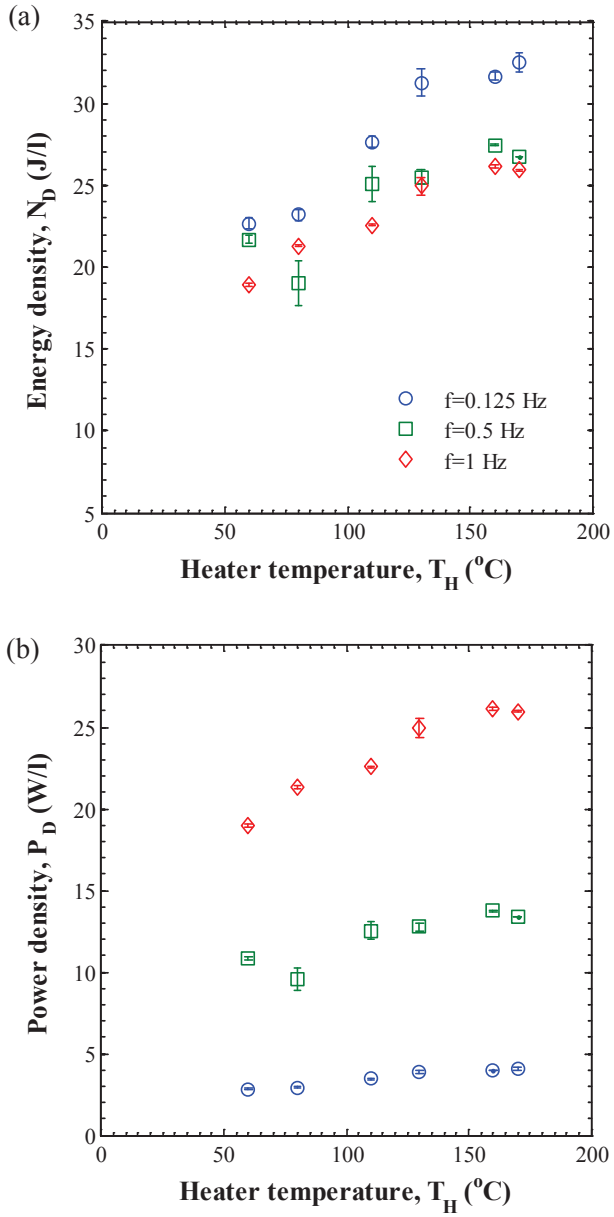

Figure 6.9: Experimentally measured (a) energy density and (b) power density generated by performing the new power cycle on PMN-28PT as a function of heater temperature T_H for frequency varying from 0.125 to 1 Hz with T_C=22^{o}C, E_L=0.2 MV/m, E_H=0.95 MV/m, and σ_H=25.13 MPa.

Figures 6.10a and 6.10b show typical electric displacement changes D-D_4 versus time t for

the new thermomechanical power cycle performed at frequency 0.125 and 1 Hz, respectively. For illustration purposes, state 4 of the cycle was used as a reference. Figures 6.10a and 6.10b also show the states 1 to 4 of the cycle corresponding to those shown in Figure 6.1c. In both cases, the heater temperature T_H was maintained at 160^{o}C, the low and high electric fields E_L and E_H were respectively 0.2 and 0.75 MV/m, and the compressive stress was σ_H=25.13 MPa. Figure 6.10a clearly illustrates the piezoelectric and pyroelectric contributions to the cycle at 0.125 Hz. During process 4-1, approximately 85% of the rise in electric displacement from 0 to 6 μC/cm^2 occurred in the first 0.25 seconds. This change can be attributed to the change in compressive stress from σ_H to 0 MPa. Then, the remaining 15% of the change in electric displacement during process 4-1 occurred between 0.25 and 3.5 seconds and can be attributed to cooling of the sample from T_{hot}=101^{o}C to T_{cold}=90^{o}C. In addition, Figure 6.10b shows a similar response to the reduction in compressive stress during process 4-1 as the electric displacement increased from 0 to 6 μC/cm^2 in the first 0.25 seconds. However, at 1 Hz the sample did not have time to experience cooling during process 4-1 and no additional changes in electric displacement took place. As a result, the generated energy density as well as the overall change in electric displacement between states 4 and 2 for the cycle at 1 Hz were approximately 85% of those at 0.125 Hz. This indicates that the piezoelectric contribution to the new cycle was independent of cycle frequency between 0.125 and 1 Hz while the pyroelectric contribution decreased with increasing frequency.

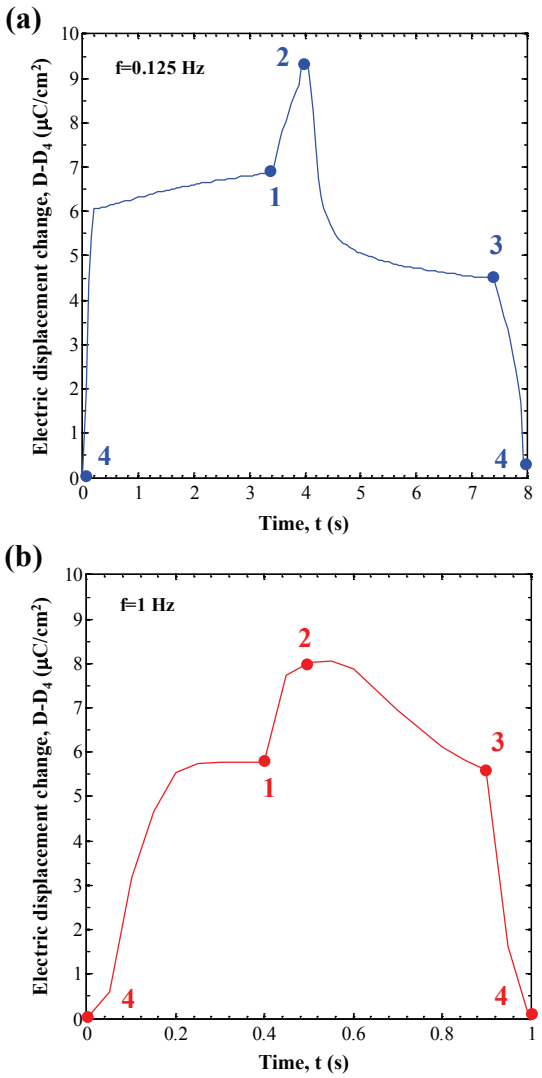

Figure 6.10: Experimentally measured electric displacement versus time for the new power cycle for frequency (a) 0.125 and (b) 1 Hz. The temperature T_H was maintained at 160^{o}C, the low and high electric fields E_L and E_H were set at 0.2 and 0.75 MV/m, while σ_H was 25.13 MPa.

6.4.6 Maximum power density

Figure 6.11 shows five consecutive new cycles performed on PMN-28PT in the D-E diagram corresponding to the maximum generated power density. The heat sink and heat source temperatures T_C and T_H were set at 22 and 130^{o}C, respectively. The high compressive stress σ_H was 33.56 MPa. The low and high electric fields were 0.2 and 0.95 MV/m, respectively. The cycle frequency was 1 Hz and the resulting sample temperature was $T_{hot} \simeq T_{cold}$=85^{o}C, corresponding to the phase boundary between the monoclinic phase and the highly polarized tetragonal phase. The consecutive cycles nearly overlapped indicating that the cycle was highly repeatable resulting in power density of 41.3±0.4 W/L.

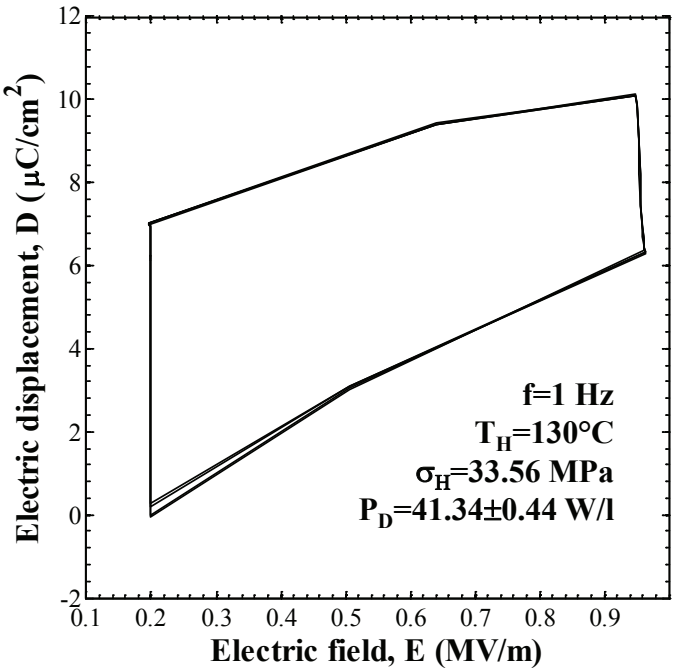

Figure 6.11: D-E path of five consecutive cycles of the highest experimentally measured power density generated with PMN-28PT with T_C=22^{o}C, T_H=130^{o}C, f=1 Hz, E_L=0.2 MV/m, E_H=0.95 MV/m, and σ_H=33.56 MPa.

6.4.7 Material efficiency

Table 6.1 summarizes the operating conditions, energy inputs Q_{in} and W_{in}, generated energy density N_D, and the material efficiency η obtained experimentally for various conditions of the new power cycle performed on PMN-28PT. It also gives conditions corresponding to the maximum material efficiency of the Olsen cycle. The material efficiency of the thermomechanical power cycle and of the Olsen cycle was estimated using Equation (6.1). The thermal energy Q_{in} was estimated according to Equation (6.2) using the measured density and specific heat c_p presented Chapter 4 Section 4.4.5 and shown in Figure 4.9. The mechanical energy input W_{in} was computed from Equation (6.3) using the area enclosed by the stress-strain curves at 20^{o}C measured at 0.17 and 1.01 MV/m reported by McLaughlin *et al.*[76] for [001] PMN-32PT single crystals. When the new cycle was performed at low frequency, the large heat input resulted in small efficiencies. These results illustrate the importance of operating under small temperature swings and heat input to improve the cycle efficiency.

Table 6.1: List of operating conditions, energy inputs Q_{in} and W_{in}, generated energy density N_D, and material efficiency η for the new cycle and the maximum Olsen cycle efficiency. In all cases, the low electric field was E_L=0.2 MV/m.

Cycle type	f (Hz)	E_H (MV/m)	T_H (^{o}C)	T_{hot} (^{o}C)	T_{cold} (^{o}C)	σ_H (MPa)	W_{in} (kJ/m^3)	Q_{in} (kJ/m^3)	N_D (kJ/m^3)	η (%)
Olsen	0.021	0.75	-	170	90	0	0	540	86	15.9
TM	0.025	0.75	157	108.5	51.9	18.81	31	1202	24	1.9
TM	0.025	0.75	107	73.9	40.2	18.81	31	292	15	4.6
TM	0.125	0.75	160	103.1	90.4	25.13	43	301	32	9.3
TM	0.125	0.75	130	85.1	74.4	25.13	43	469	31	6.1
TM	0.5	0.75	160	100.9	99.9	25.13	43	21	27	42.2
TM	0.5	0.75	130	83.2	82.2	25.13	43	62	26	24.8
TM	1	0.75	160	104.4	104.3	25.13	43	2	26	57.8
TM	1	0.75	130	85.4	85.3	25.13	43	9	25	48.1
TM	1	0.95	130	85.4	85.3	33.56	61	9	41	58.6

Moreover, for a given temperature swing, the efficiency was highly dependent on the operating temperatures. For example, the two cycle performed at 0.5 Hz in Table 6.1 both

had similar energy density N_D, the same W_{in}, and a temperature swing T_{hot}-T_{cold}=1^{o}C, but their efficiencies differed by a factor of two. This difference can be attributed to the operating temperatures. One cycle was performed between 82.3 and 83.2^{o}C where $c_p(T)$ exhibited a phase transition peak and a large thermal hysteresis (Figure 4.9) while the other was performed between 99.9 and 100.9^{o}C, where no phase transition occurred. This emphasizes the importance of choosing the operating temperatures such that the heat input is minimized and the energy density is maximized in order to maximize the material efficiency η. In fact, the maximum power density cycle performed at 1 Hz and shown in Figure 6.11 achieved an efficiency larger than 58%. In this case, the heat input was Q_{in}=9 kJ/m^3 and the mechanical work performed was W_{in}=61 kJ/m^3. Although the sample underwent small temperature fluctuations T_{hot}-$T_{cold}$$\simeq$0.1^{o}C during the cycle, the corresponding thermal energy input Q_{in} was comparable to the mechanical energy W_{in}.

In addition, at low frequencies, it is important to choose T_{cold} such that heating and applying compressive stress have a similar effect on the electric displacement. The two cycles performed at 0.125 Hz in Table 6.1 illustrate this fact. The cycle performed between 90.4 and 103.1^{o}C had a material efficiency of 9.3%. In this case, the material was in the highly polarized tetragonal phase at T_{cold}=90.4^{o}C and E_H=0.75 MV/m.[74] Then, both heating and the addition of compressive stress during process 2-3 worked cooperatively to decrease the electric displacement of the material. On the other hand, for the cycle performed between 74.4 and 85.1^{o}C, the sample was near the phase boundary between monoclinic M_C and tetragonal at T_{cold}=74.4^{o}C and E_H=0.75 MV/m.[74] Then, during process 2-3, the electric displacement decreased with applied compressive stress and increased with heating. In this case, the material efficiency was 6.1%. Both of these cycles yielded a similar energy density, however one consumed an additional 168 kJ/m^3 of thermal energy per cycle.

Finally, note that the efficiency reported corresponds to the material's ability to convert thermomechanical energy into electricity. The efficiency of a device implementing the new cycle on PMN-28PT is expected to be significantly lower. In addition, W_{in} was estimated based on properties of PMN-32PT measured at room temperature.[76] In practice, the me-

chanical work was performed at two different temperatures at which properties were typically unknown. Moreover, Q_{in} was estimated based on the specific heat $c_p(T)$ measured under zero mechanical stress. In practice, the heat input occurred under large uniaxial compressive stress known to affect the phase transition temperatures and the corresponding peaks in $c_p(T)$. Furthermore, note that the material efficiency of the Olsen cycle reached 88% of the Carnot efficiency between T_{cold}=70^{o}C and T_{hot}=170^{o}C.

6.5 Chapter summary

This chapter presented the concept and experimental implementation of a novel thermomechanical power cycle. It reported the experimentally measured energy and power densities generated by performing the novel thermomechanical power cycle on [001]-poled PMN-28PT single crystals. Maximum energy and power densities of 41 J/L/cycle and 41 W/L were achieved at 1 Hz for heat sink and heat source temperatures T_C=22^{o}C and T_H=130^{o}C and electric field cycled between 0.2 and 0.95 MV/m with compressive stress σ_H=33.56 MPa. These conditions also yielded the maximum material efficiency of converting thermomechanical energy into electric energy of 58.6%. The energy density of the new cycle was found to be nearly independent of cycle frequency, while the power density and efficiency increased with increasing cycle frequency. In addition, both N_D and P_D increased with increasing compressive stress. Furthermore, the cycle was able to produce energy and power with T_{hot} below T_{Curie} and was adaptable to changing thermal and mechanical conditions. Future work should consist of implementing this cycle into autonomous and integrated devices.

CHAPTER 7

A Novel Thermally-Biased Mechanical Energy Conversion Cycle

This chapter presents experimental measurements of energy and power densities generated by performing a new power cycle for direct conversion of mechanical energy into electrical energy under a thermal bias. It uses compressive stress to induce phase transitions in [001]-poled PMN-28PT single crystals heated near their morphotropic phase boundary. It aims to improve the power density and material efficiency of the thermomechanical cycle presented in Chapter 6 by substituting the thermal cycling by a thermal bias. In addition, this chapter presents a physical model predicting the energy and power densities of the new cycle.

7.1 Introduction

The Olsen cycle performed on pyroelectric materials can convert temporal temperature oscillations directly into electricity[20] as previously discussed in Chapter 2 Section 2.3.4. In addition, time-dependent mechanical deformations imposed on piezoelectric materials connected to an external electrical load can generate electricity.[6,110] These mechanical deformations can be small deflections at high frequency due to vibrations[6] or can be large strains due to the application of large cyclic compressive stress.[110] Furthermore, the thermomechanical power cycle demonstrated by McKinley *et al.*[111] and presented in Chapter 6 Section 6.2.1 performed on ferroelectric materials utilizes time-dependent temperature and compressive stress oscillations to convert both thermal and mechanical energies directly into electricity. This cycle achieved larger energy and power densities than the Olsen cycle for lower operating temperatures.[111] This was achieved (i) by combining both piezoelectric and pyroelectric

energy conversion and (ii) by increasing the cycle frequency by quickly forcing the material into a specific state using mechanical stress instead of heating and cooling which are inherently slow. However, the heat input still dominated the energy consumption of this power cycle at low cycle frequencies and negatively affected the material efficiency.[111] This chapter presents a new cycle using variable uniaxial compressive stress in addition to electric field cycling but at a fixed temperature. We hope that this new cycle can achieve larger cycle efficiency than the thermomechanical cycle by reducing the required heat input. In addition, we hope that this cycle can make use of waste heat to enhance mechanical energy harvesting.

7.2 Thermally-biased mechanical power cycle

7.2.1 Principle

Figure 7.1a illustrates the new power cycle in the D-E diagram overlaid with the corresponding isothermal bipolar D-E loops at constant bias-temperature T_b under zero stress and under compressive stress σ_H. Figure 7.1b schematically illustrates the practical implementation of the new power cycle and the stress, temperature, and electric field imposed in each state. Process 1-2 consists of an isothermal increase in electric field from E_L to E_H, performed in the absence of compressive stress. Process 2-3 corresponds to compressing the sample under stress σ_H. Process 3-4 consists of an isothermal decrease in electric field from E_H to E_L under compressive stress σ_H. Finally, process 4-1 closes the cycle by removing the loading under constant electric field E_L. The area enclosed by the four processes in the D-E diagram, shown in Figure 7.1a, corresponds to the generated energy density N_D defined by Equation (1.1). It is evident that the energy density N_D can be increased by increasing the electric field span E_H-E_L and/or increasing the change in electric displacement during processes 2-3 and 4-1.

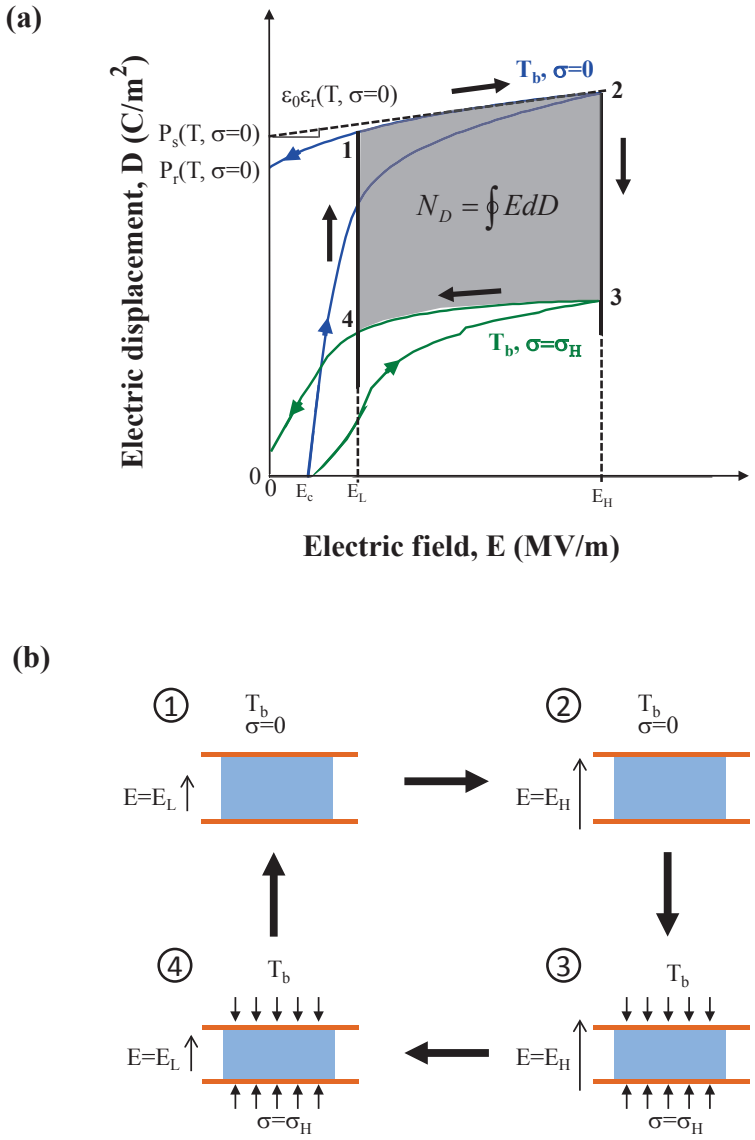

Figure 7.1: (a) Two-dimensional projection of the new power cycle in the D-E plane. Electric displacement versus electric field loops for uniaxial stress σ=0 and for σ_H at temperature T_b. The electrical energy generated per cycle is represented by the grey areas enclosed between 1-2-3-4. (b) The thermal, electrical and stress states of the ferroelectric sample during each point of the new power cycle.

7.2.2 Experiments

Samples

Single crystal PMN-28PT was chosen to demonstrate the thermomechanical power cycle[111] presented in Chapter 6 for its strong piezoelectric response in a broad temperature range.[92] The PMN-28PT samples used in this study were similar to those described in Chapter 4 Section 4.3.1. In addition, two strain gages were mounted to opposite 5×3 mm^2 faces of one of the samples to measure longitudinal strain x_3 (parallel to the polarization direction).

Experimental setup

The experimental setup included an electrical and a thermomechanical subsystem. The electrical subsystem was a Sawyer-Tower circuit identical to that used in our previous studies that simultaneously measured electric field and electric displacement.[52,97–101,111] Figure 7.2 shows a schematic of the thermomechanical subsystem used to perform the novel power cycle. The subsystem consisted of a spring return air cylinder (McMaster-Carr 6498K252) vertically actuated using compressed air at a maximum pressure of 469 kPa. A 24 V DC solenoid valve was used to control the extension and contraction of the cylinder rod applying pressure on the sample between two copper rods. The PMN-28PT sample was sandwiched between two copper tapes used to provide electrical contact between the sample's electrodes and the wires. A 0.14 mm thick Kapton film was used to electrically isolate the sample's electrodes from the copper rods. The sample was placed inside an acrylic support structure submerged in a heated silicone oil bath. A 100-Watt cartridge heater was imbedded in a 1.27 cm thick aluminum plate serving as a heat source to the oil bath. A type-K thermocouple was embedded at the center of this heating block whose temperature was maintained at T_H with an Omega CN-7823 proportional integral derivative (PID) temperature controller. The corresponding sample bias-temperature T_b was measured by a type-K thermocouple placed on the sample. After the desired steady-state temperature was reached, this second thermocouple was removed prior to performing the cycle so that it did not electrically interfere

with electrical measurements performed on the sample.

In addition, a servo-hydraulic test frame described in Ref.[137] was used in place of the spring return air cylinder for mechanical characterization of the sample during the cycle. The compressive force applied by this servo-hydraulic mechanism was computer-controlled enabling strain to be measured as a function of stress while also simultaneously measuring electric field and electric displacement.

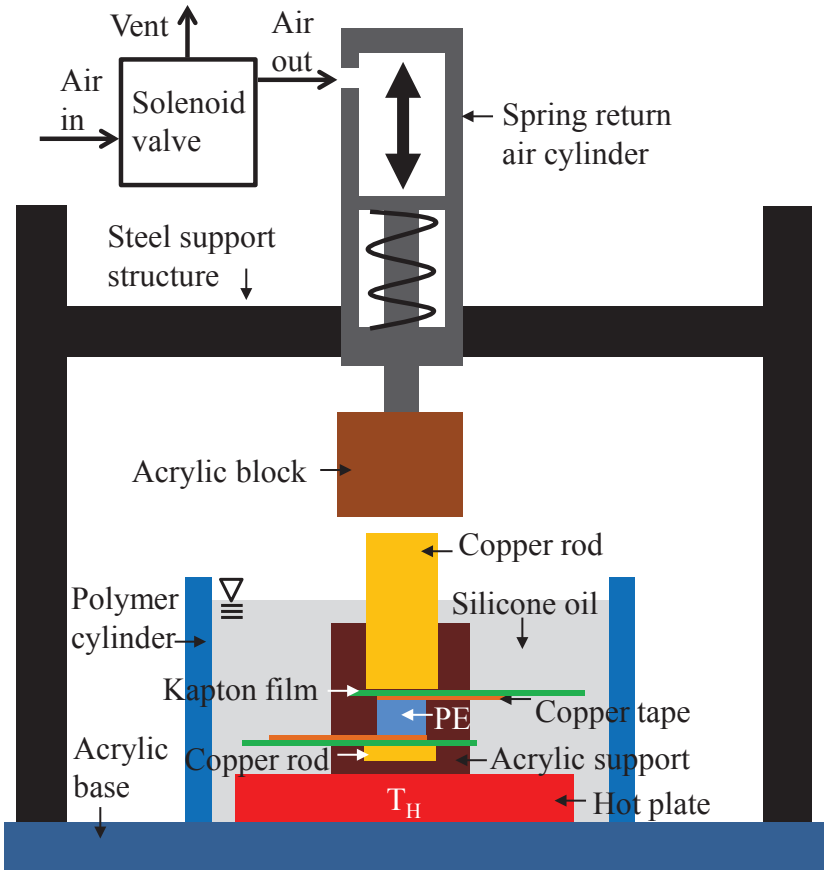

Figure 7.2: Schematic of the thermomechanical subsystem used to create the temperature bias and to apply compressive stress during the new thermally-biased mechanical power cycle depicted in Figure 7.1. Dimensions are not to scale.

Experimental procedure

First, isothermal bipolar D-E hysteresis loops of [001] PMN-28PT were collected for bias-temperature of 100^{o}C and compressive stress varying from 0 to 25.13 MPa. D-E loops under similar compressive stress but for bias-temperature of 22 and 80^{o}C were reported in our pre-

vious study.[111] The dielectric properties of PMN-28PT were estimated from the isothermal bipolar D-E loops. The saturation polarization $P_s(T,\sigma)$ and the large-field dielectric constant $\varepsilon_r(T,\sigma)$ were evaluated by linearly fitting the bipolar D-E loops corresponding to a decrease in electric field from 0.75 to 0.5 MV/m according to Equation (2.9) and as illustrated in Figure 7.1a.

Second, the new cycle was performed so that the duration of each process was equal $\tau_{12} = \tau_{23} = \tau_{34} = \tau_{41}$. The new power cycle was executed for frequency ranging from 0.5 to 3 Hz by varying τ_{ij} between 1 and 0.083 seconds, respectively. The sample bias-temperature T_b varied from 22 to 100^{o}C, and the uniaxial stress σ_H applied during processes 2-3 and 3-4 ranged from 0 to 35.67 MPa. The low and high electric fields E_L and E_H were fixed at 0.2 and 0.8 MV/m, respectively.

In addition, the new power cycle was performed at very low cycle frequency ($f \sim$0.004 Hz) in the servo-hydraulic test frame[137] while the electric field, electric displacement, stress, and strain were simultaneously measured. The load frame measured the applied force ranging from 0 to 850 N corresponding to stress of 0 to 34 MPa. The energy density generated per cycle N_D was evaluated by numerically integrating experimental data for D versus E according to Equation (1.1) using the trapezoidal rule. The mechanical work done per cycle W_{in} was evaluated by numerically integrating experimental data for σ versus x according to Equation (6.3) using the trapezoidal rule. Finally, the material efficiency η given by Equation (6.1) was estimated.

7.2.3 Physical Modeling

Recently, Kandilian *et al.*[97] developed a model to predict the energy density generated by the Olsen cycle. This model can easily be adapted to predict the power density generated by materials undergoing the present thermally-biased mechanical cycle. According to Equation (2.9), the large-field dielectric constant $\varepsilon_r(T,\sigma)$ and the saturation polarization $P_s(T,\sigma)$ are functions of both temperature and compressive stress. Assuming the D-E path of the new

cycle follows that of the D-E loops at bias-temperature T_b both under zero and σ_H stress, the power density of the new cycle at frequency f can be expressed as

$$\begin{aligned} P_D &= f\frac{\varepsilon_0}{2}\left(E_H - E_L\right)\left(E_H + E_L\right)\left[\varepsilon_r(T_b,0) - \varepsilon_r(T_b,\sigma_H)\right] + \\ &+ f\left(E_H - E_L\right)\left[P_s\left(T_b,0\right) - P_s\left(T_b,\sigma_H\right)\right] \end{aligned} \tag{7.1}$$

This model could enable the rapid determination of the power density of materials undergoing the new cycle from intrinsic dielectric properties of PMN-28PT without physically having to perform the cycle. But first, it must be validated experimentally.

7.3 Results and discussion

7.3.1 Isothermal bipolar D-E loops

Figure 7.3 plots isothermal bipolar D-E loops measured at 0.1 Hz on [001] PMN-28PT samples for bias-temperature T_b of (a) 80^o and (b) 100^oC under mechanical loading ranging between 0 and 25.13 MPa. The D-E loops were closed and consecutive D-E loops overlapped for any temperature and compressive stress considered. This indicates that leakage current through the sample was negligibly small. Figure 7.3 illustrates that the D-E loops gradually became slimmer with increasing compressive stress. This behavior is indicative of continuous polarization rotation and was previously observed with [001] PMN-32PT.[75]

Figure 7.4 shows (a) the saturation polarization $P_s(T,\sigma)$ and (b) the large-field dielectric constant $\varepsilon_r(T,\sigma)$ retrieved from the isothermal bipolar D-E loops for temperatures 22, 80, and 100^oC and compressive stress between 0 and 25.13 MPa. Each data point represents the average over three D-E loops. The error bars have been omitted because they fell within the data markers. In addition, Figure 7.4 also shows the piecewise cubic hermite interpolating polynomial fit of the properties for each temperature considered. Figure 7.4a indicates that the saturation polarization P_s decreased nearly linearly with increasing stress at 22 and 100^oC. This behavior is also characteristic of continuous polarization rotation corresponding to a continuous phase transition.[75,76] On the other hand, at 80^oC, the saturation polarization

was nearly constant below 6.16 MPa and decreased linearly with compressive stress beyond. This can be attributed to phase transition from tetragonal to monoclinic at 80^{o}C and compressive stress between 6.16 and 10.38 MPa. Indeed, at 80^{o}C, [001] PMN-28PT assumes the tetragonal phase under zero stress and electric field above 0.4 MV/m.[74] In addition, [001] PMN-32PT was reported to assume the monoclinic phase at 80^{o}C under stress above 10 MPa and electric field below 1 MV/m.[76] As stress increased from 0 to 25 MPa, the largest change in saturation polarization occurred at 80^{o}C, while the smallest change occurred at 22^{o}C. Figure 7.4b indicates that the large-field relative permittivity increased with increasing compressive stress for all temperatures considered. This behavior is consistent with bipolar D-E loops reported for [001] PMN-30PT[113] and [001] PMN-32PT[75] at room temperature for compressive stress up to 30 MPa.

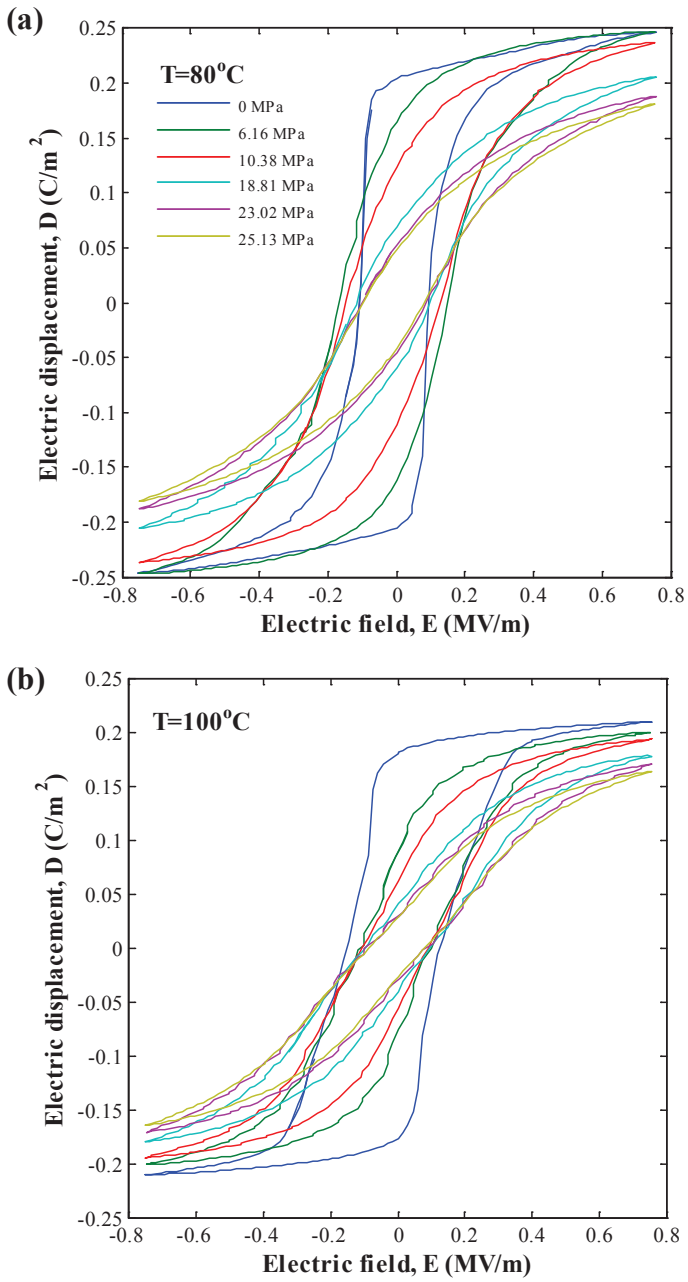

Figure 7.3: Isothermal bipolar D-E loops of [001] PMN-28PT at 0.1 Hz for temperatures (a) 80^{o}C and (b) 100^{o}C and compressive stress σ between 0 and 25.13 MPa.

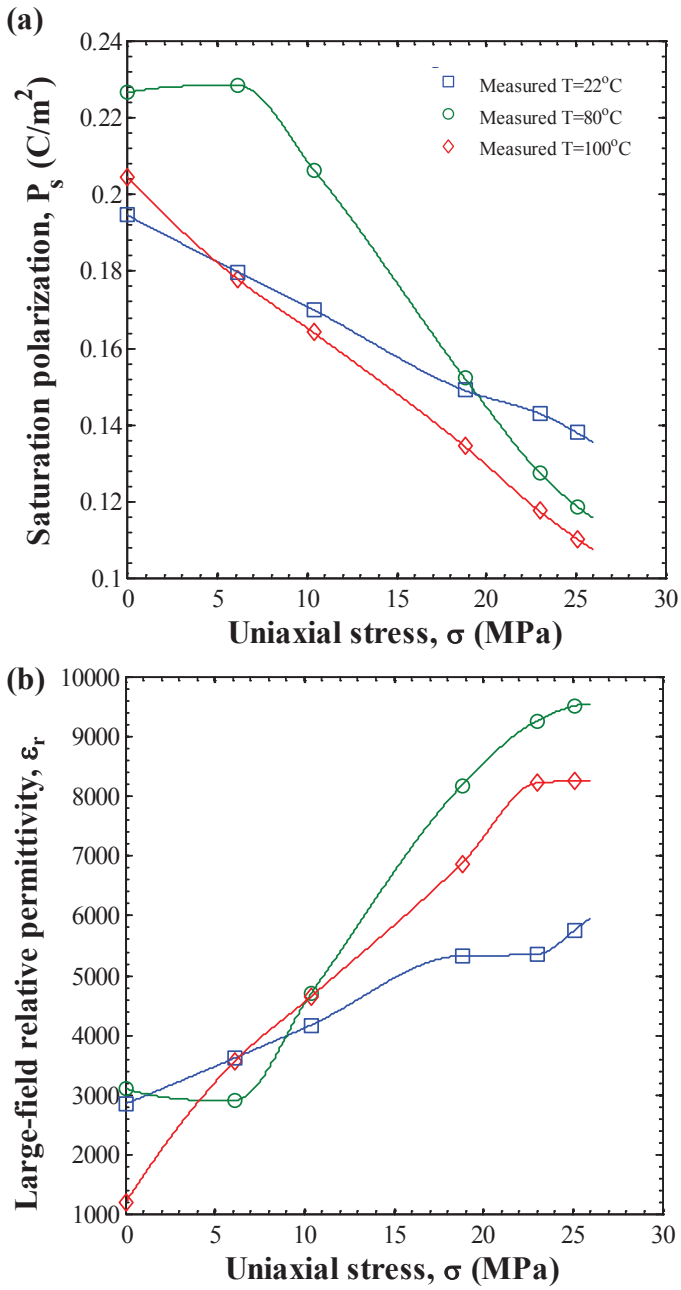

Figure 7.4: (a) Saturation polarization $P_s(T, \sigma)$ and (b) large-field relative permittivity $\varepsilon_r(T, \sigma)$ as a function of uniaxial stress retrieved from the isothermal bipolar D-E loops of PMN-28PT at 0.1 Hz for temperatures 22, 80, and 100°C (Figure 7.3). The solid lines correspond to the piecewise cubic hermite interpolating polynomial fit.

7.3.2 Thermally-biased mechanical power cycle

Demonstration

Figure 7.5 depicts, in the D-E diagram, the new mechanical power cycle performed at 1 Hz at bias-temperature T_b=80^{o}C. The electric field was cycled between E_L=0.2 MV/m and E_H=0.8 MV/m. A compressive stress of σ_H=25.13 MPa was applied during processes 2-3 and 3-4. The cycle traveled in the clockwise direction and therefore produced electrical energy. Figure 7.5 also shows the isothermal bipolar D-E loops measured at 80^{o}C at 0.1 Hz under zero stress and σ_H=25.13 MPa as well as at 0.75 Hz under zero stress. Note that the rate of electric field change dE/dt for the D-E loops at 0.1 Hz and 0.75 Hz was 0.3 and 2.4 MV/m·s, respectively. Processes 1-2 and 3-4 of the cycle performed at 1 Hz corresponded to a time rate of change in electric field of 2.4 MV/m·s. However, Figure 7.5 indicates that at the frequencies considered, the D-E loops were independent of dE/dt. In addition, the power cycle shown was vertically translated to match the electric displacement of the D-E loop for T_b and σ=25.13 MPa, as performed by Kandilian *et al.*[97] It is evident that the cycle closely followed the bipolar D-E loops corresponding to the conditions of the cycle. Thus, using the properties $P_s(T,\sigma)$ and $\varepsilon_r(T,\sigma)$ previously retrieved from the bipolar D-E loops at 0.1 Hz was appropriate to predict the power density based on Equation (7.2).

Given the phase diagram of PMN-28PT reported in Ref.[74] at frequency of 10 Hz, we speculate that, at bias-temperature of 80^{o}C, PMN-28PT was in the tetragonal T phase at both state 1 and 2 of the cycle. This is supported by the fact that (i) the coercive electric field in the D-E loops at low frequency of 0.1 Hz was around 0.1 MV/m and (ii) the change in electric displacement between these states was small as illustrated in Figure 7.5. In addition, we speculate that the application of compressive stress during process 2-3 caused the sample to undergo a phase transition into the monoclinic M_A phase, as suggested by the T-M_A phase transition occurring in [001] PMN-32PT at 0.8 MV/m and 80^{o}C under σ=13 MPa.[76] Furthermore, the decrease in electric field during process 3-4 caused another phase transition into the depolarized orthorhombic O phase. This was suggested by the

M_A-O phase transition in [001] PMN-32PT occurring at 0.2 MV/m and 80^{o}C under σ=20 MPa.[76] Finally, during process 4-1, when stress was removed at constant electric field 0.2 MV/m, the sample transitioned back to the tetragonal phase. Thus, during the cycle at 80^{o}C, the sample successfully alternated between a depolarized state and a highly polarized state corresponding to a large change in electric displacement and a large energy density.

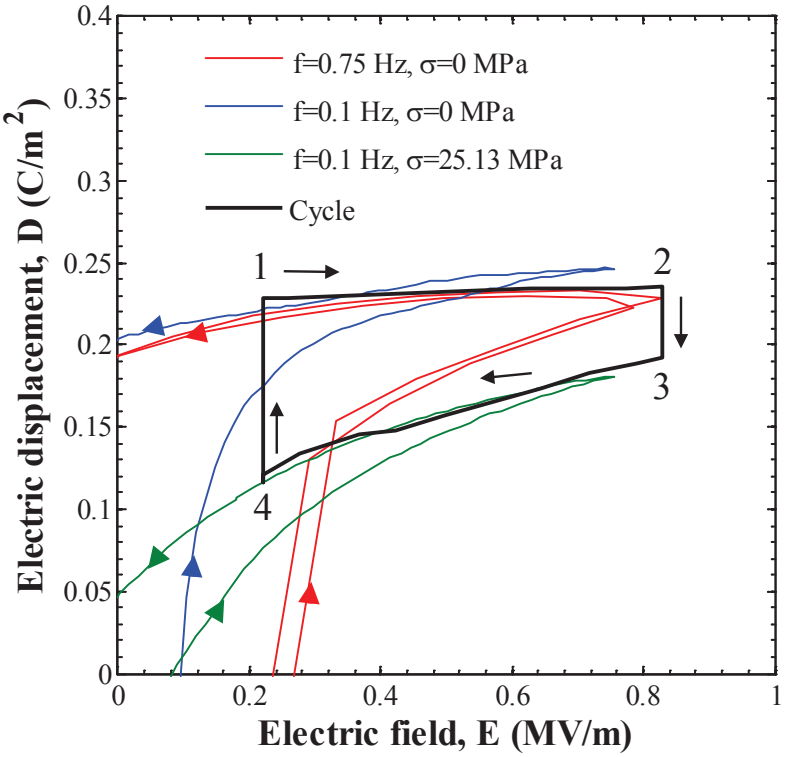

Figure 7.5: Isothermal bipolar D-E loops collected at 0.1 or 0.75 Hz and experimental power cycle performed at frequency f=1 Hz on PMN-28PT for electric field between E_L=0.2 MV/m and E_H=0.8 MV/m at T_b=80^{o}C and compressive stress between σ=0 to σ_H=25.13 MPa. The power cycle was vertically displaced to match the D-E loop at T=80^{o}C and σ_H=25.13 MPa.

Effect of temperature and compressive stress

Figure 7.6 shows the power density generated by the new power cycle as a function of applied compressive stress σ_H for bias-temperature T_b ranging between 22 and 100^{o}C. Here, the frequency was fixed at 1 Hz while the electric field was cycled between 0.2 and 0.8 MV/m. Each data point represents an average of five cycles and the error bars correspond to one standard deviation or 63% confidence interval. Figure 7.6 indicates that the power density increased nearly linearly with increasing σ_H for any given bias-temperature T_b. For T_b above 80^{o}C, the power density decreased and was nearly identical for 90 and 100^{o}C. In fact, the largest power density of 44 W/L was achieved for bias-temperature of 80^{o}C with a compressive stress of 25.13 MPa. This optimum performance can be explained by the tetragonal to monoclinic to orthorhombic phase transition sequence previously discussed. On the other hand, for bias-temperatures of 90 and 100^{o}C, the material remained in the highly polarized tetragonal phase away from any phase boundaries for all electric fields considered under zero stress.[74] At these temperatures, the application of large compressive stress during process 2-3 also caused a phase transition into the monoclinic phase. However, the decrease in electric field during process 3-4 did not lead to a phase transition into the orthorhombic phase. This interpretation is supported by extrapolation of the [001] PMN-32PT phase diagram reported in Ref.[76] to PMN-28PT at 90^{o}C and 100^{o}C. This resulted in nearly identical power density generated versus compressive stress at these temperatures.

Furthermore, for cycles performed at 22^{o}C, the material transitioned from the rhombohedral to the monoclinic phase during process 1-2, as suggested by the PMN-28PT phase diagram at zero stress.[74] Then, for large compressive stress σ_H, the sample transitioned into the orthorhombic phase during process 3-4, as suggested by the PMN-32PT phase diagram.[76] Overall, the power density with T_b=22^{o}C was limited by the fact that the sample never reached the highly polarized tetragonal phase. These results indicate that to maximize power generation of PMN-28PT, the new cycle should be performed at temperatures where the tetragonal phase is present. In addition, the compressive stress σ_H should be large enough to induce the orthorhombic phase at the temperature and electric field corresponding

to state 2 of the cycle.

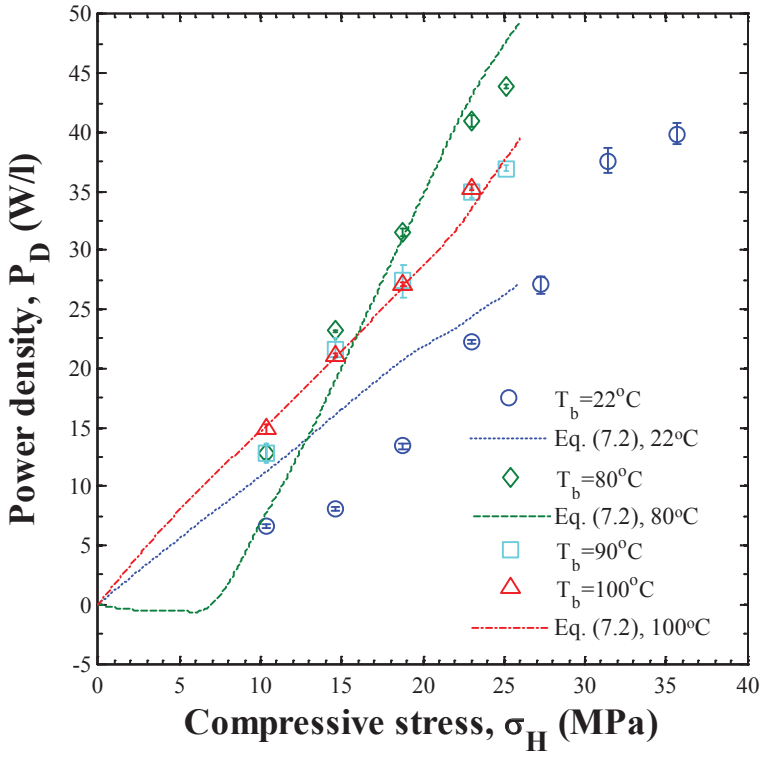

Figure 7.6: Experimentally measured power density generated by performing the thermally-biased mechanical power cycle on [001] PMN-28PT as a function of compressive stress. The bias-temperature T_b ranged from 22 to 100^{o}C. The frequency was fixed at 1 Hz. The low and high electric fields E_L and E_H were set at 0.2 and 0.8 MV/m. The lines represent the predictions of the model given by Equation (7.2) using properties retrieved from bipolar D-E loops.

Effect of frequency

Figure 7.7 shows the power density generated by the thermally-biased mechanical power cycle as a function of compressive stress σ_H for frequency of 0.5, 1, 2, and 3 Hz. The low and high electric fields E_L and E_H were set at 0.2 and 0.8 MV/m, and the bias-temperature T_b was 80^{o}C. Each data point represents an average over five cycles and the error bars correspond to one standard deviation or 63% confidence interval. It is evident that the power density increased with increasing compressive stress for frequency below 1 Hz. However, at higher frequency, the power density reached a maximum at compressive stress of 23.02 MPa and decreased beyond. This can be attributed to the fact that, at high cycle frequency, the electric displacement did not reach an equilibrium value during processes 2-3 and 4-1. Furthermore, the large error bars for frequency of 3 Hz was due to inconsistent changes in electric displacement during each process from one cycle to the next. Figure 7.7 establishes that a cycle frequency of 1 Hz yields the highest power density for high compressive stress at 80^{o}C.

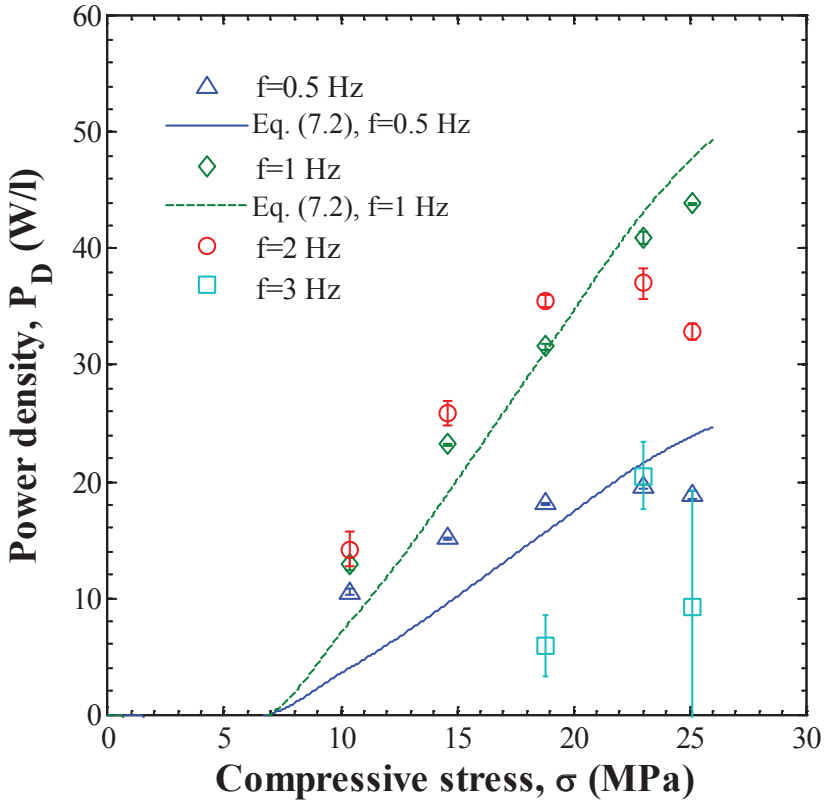

Figure 7.7: Experimentally measured power density generated by performing the new power cycle on [001] PMN-28PT as a function of compressive stress σ_H for frequency ranging from 0.5 to 3 Hz. The bias-temperature T_b was maintained at 80^{o}C. The low and high electric fields E_L and E_H were set at 0.2 and 0.8 MV/m. The lines represent the predictions of the model given by Equation (7.2) using properties retrieved from bipolar D-E loops.

7.3.3 Model predictions

Figure 7.6 compares experimental data and model predictions obtained from Equation (7.2) for the power density P_D at bias-temperature T_b of 22, 80, and 100^{o}C. Predictions were based on the dielectric properties previously estimated from isothermal bipolar D-E loops

measured at these temperatures. Analysis of the electric displacement variations $D(t)$-D_4 versus time t with T_b=80^{o}C for cycle frequency ranging from 0.5 to 2 Hz confirmed that the properties extracted from the D-E loops at 0.1 Hz can be used in the model given by Equation (7.2) (see Appendix B). However, predictions for T_b=90^{o}C were not included because isothermal D-E loops were not collected at 90^{o}C. Figure 7.6 indicates that the model predictions agreed well with experimental data. In fact, the average relative error between experimental data and model predictions was 47.6%, 13.9%, and 2.4% for T_b equal to 22, 80, and 100^{o}C, respectively. The largest error for T_b=22^{o}C corresponded to small values of σ_H. Overall, the model predictions were acceptable.

Figure 7.7 shows the model predictions of the power density at T_b=80^{o}C for frequency of 0.5 and 1 Hz. Here also, the model yields reasonable predictions. In fact, the average relative error between experimental data and model predictions at 0.5 and 1 Hz was 29.1% and 13.9%, respectively. Note that the model did not yield accurate predictions for frequencies larger than 1 Hz because then, the cycle did not follow the path of the D-E loops at 0.1 Hz. In other words, D did not reach its equilibrium value during processes 2-3 and 4-1 as previously discussed. Overall, these results validate the model for P_D given by Equation (7.2). It can be used to predict energy (N_D=P_D/f) and power densities from the material dielectric properties.

7.3.4 Material efficiency

Figure 7.8a presents the relative electric displacement D-D_4 as a function of electric field E experimentally measured during the new thermally-biased mechanical cycle performed at T_b=80^{o}C and T_b=100^{o}C at low frequency f∼0.004 Hz with E_L=0.2 MV/m, E_H=0.8 MV/m, and σ_H=25 MPa. Figure 7.8b shows the corresponding experimentally measured stress σ versus relative strain x_3-$x_{3,1}$. The energy density N_D was measured as 39.7±1.0 and 31.2±1.0 J/L/cycle and the mechanical work W_{in} was 53.1±1.3 and 47.7±3.1 J/L/cycle for cycles performed at 80 and 100^{o}C, respectively. The corresponding material efficiency η, given by Equation (6.1), was equal to 74.6±0.1% and 65.3±3.3%, respectively. Note

that the heat input Q_{in} was taken as zero thanks to the bias-temperature kept constant during the cycle. These large efficiencies demonstrate that the material undergoing the new cycle was very efficient at converting mechanical energy into electrical energy. The largest energy density, power density, and material efficiency were obtained at 80^{o}C thanks to the tetragonal-monoclinic-orthorhombic phase transition sequence resulting in large changes in electric displacements, as previously discussed. In addition, less mechanical energy was required to cause these phase transitions at 80^{o}C than at 90 or 100^{o}C. At 100^{o}C, the PMN-28PT sample had not transitioned to the orthorhombic phase for the stresses considered. This is illustrated in Figure 7.8 by the fact that increasing compressive stress from 0 to 25 MPa during process 2-3 produced a larger change in (i) strain and (ii) electric displacement at 80^{o}C than at 100^{o}C.

Finally, a maximum material efficiency of 87.3±5.6% was obtained at low frequency f∼0.004 Hz with T_b=85^{o}C, E_L=0.2 MV/m, E_H=0.95 MV/m, and σ_H=34 MPa. Under these conditions, N_D=47.8±1.4 J/L/cycle and W_{in}=54.9±1.9 J/L/cycle. These operating conditions were the same as those that yielded the maximum material efficiency of 64.1% for our previous thermomechanical power cycle.[111] Note that originally we estimated this efficiency to be 58.6%[111] based on a mechanical energy input of 61 J/L/cycle estimated from the stress-strain curves of PMN-32PT at 0.17 and 1.01 MV/m reported in Ref.[76] However, the mechanical energy input measured here provided a more accurate estimate and yielded a material efficiency of 64.1%. Thus, the thermally-biased mechanical power cycle achieved larger material efficiency by replacing the thermal cycling in the thermochanical power cycle with a temperature-bias.

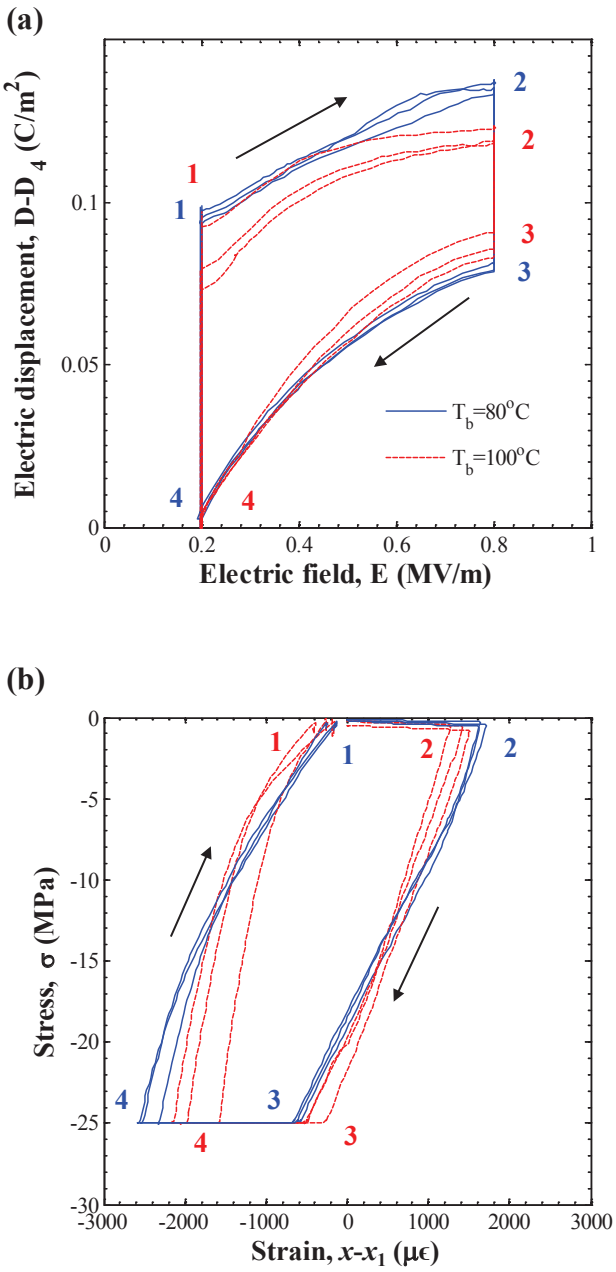

Figure 7.8: (a) Experimentally measured stress versus strain diagrams for the thermally-biased mechanical power cycle performed at T_b=80^{o}C and 100^{o}C. (b) Experimentally measured electric displacement versus electric field diagrams for the thermally-biased mechanical power cycle performed T_b=80^{o}C and 100^{o}C. In all cases E_L=0.2 MV/m, E_H=0.8 MV/m, and σ_H=25 MPa.

7.3.5 Comparison of direct mechanical energy conversion methods

Table 7.1 compares the operating frequency as well as the power and energy densities experimentally harvested using various direct mechanical energy conversion methods. Roundy *et al.*[6] used a piezoelectric lead zirconate titantate (PZT) linear bimorph cantilever driven at a resonant frequency of 120 Hz and acceleration of 2.5 m/s^2 to harvest 0.98 W/L. However, the large beam deflections required to induce large strains in the PZT were only achievable at frequency near the resonance frequency. Alternatively, Wang and Yuan[139] applied a time-varying magnetic field to PZT sandwiched between magnetostrictive Terfenol-D layers to harvest 0.9 W/L at 58 Hz. The outer Terfenol-D layers were able to induce larger strains in the piezoelectric PZT than the traditional bending approach.[139] This resulted in larger energy density than the linear piezo bimorph method. However, the smaller cycle frequency caused the two methods to achieve similar power densities. In addition, Cottinet *et al.*[140] applied cyclic transverse strain of 0.2% at 100 Hz to electrostrictive terpolymer P(VDF-TrFE-CFE) films containing 1 vol.% carbon black and harvested 0.015 W/L. In this case, a bias electric field of 5 MV/m was applied continuously throughout the cycle.[140] Moreover, Dong *et al.*[110] applied cyclic compressive stress between 20 and 26 MPa at 1 Hz in the [001] direction to [110]-poled piezoelectric PIN-PMN-PT single crystals at room temperature. The increase in compressive stress induced a phase transition that increased the polarization of the material and its subsequent decrease induced the reverse phase transition. The resulting power density harvested from this cycle was 0.75 W/L corresponding to the largest energy density N_D=0.75 J/L/cycle among the previously mentioned mechanical energy harvesting methods.[110] Note that this solid-state phase change method did not have performance peaks limited to resonant frequency.[110] In addition, it differed from the new cycle in that (i) it was performed in the absence of an applied electric field and (ii) compressive stress was used to increase rather than decrease the polarization of the material. Table 7.1 indicates that the present thermally-biased mechanical cycle generated energy and power densities orders of magnitude larger than other popular methods using piezoelectric materials. However, in the present study, the energy generated was not harvested, unlike the other conversion methods.

Thus, it is critical to design an electric circuit to condition the power and to harvest the energy generated by the new cycle.

Table 7.1: Comparison of frequency, maximum power density, and energy density experimentally measured using different methods of mechanical to electrical energy conversion

Conversion method	f **(Hz)**	**Max** P_D **(W/L)**	N_D **(J/L/cycle)**	**Ref.**
Linear piezo bimorph	120	0.98	0.008	[6]
Magnetostrictive	58	0.9	0.0015	[139]
Electrostrictive polymer	100	0.015	0.0002	[140]
Mechanical phase change	1	0.75	0.75	[110]
Thermally-biased mechanical cycle	1	44	44	[112]

7.4 Chapter summary

This chapter demonstrated a novel thermally-biased mechanical power cycle on ferroelectric [001]-poled PMN-28PT single crystals. Maximum energy and power densities of 44 J/L/cycle and 44 W/L were achieved at 1 Hz for bias-temperature T_b of 80^{o}C and electric field cycled between 0.2 and 0.8 MV/m with compressive stress σ_H=25.13 MPa. In addition, the power density increased with increasing compressive stress for cycle frequency less than or equal to 1 Hz. For higher cycle frequency, the power density reached a maximum for compressive stress equal to σ_H=23.03 MPa. The maximum power density of the new cycle was obtained for temperature bias of 80^{o}C thanks to tetragonal to monoclinic to orthorhombic phase transition sequence during the cycle resulting in large changes in electric displacement. The material efficiency of this new power cycle exceeded that of the thermomechanical power cycle previously presented.[111] The energy and power densities generated by the new cycle were orders of magnitude larger than alternative mechanical energy conversion methods. Finally, a physics-based model predicting the power density was derived and validated against experimental data. It can be used to predict the energy and power densities for any mate-

rial based on their dielectric properties and the operating electric fields, temperature, and frequency.

CHAPTER 8

Summary and Recommendations

8.1 Summary

This study was concerned with the direct conversion of thermal and/or mechanical energy into electricity using ferroelectric materials. The objectives of the study were as follows: (1) to improve our understanding and the performance of the Olsen cycle by exploring the use of different materials and by taking advantage of solid-state phase transitions, (2) to explore new methods to simultaneously convert mechanical and thermal energy directly into electricity.

The first objective was achieved by measuring the energy and power densities of PZN-5.5PT and PMN-28PT single crystals undergoing the Olsen cycle under varying operating conditions. For both materials, the maximum energy density was on the order of 100 J/L/cycle. A recently developed model[97] accurately predicted the energy and power densities generated. In addition, the dielectric and thermal properties as well as the phases of PMN-28PT single crystals were characterized under various temperatures and uniaxial stress. These properties proved useful in determining the optimum operating conditions of the Olsen cycle performed on PMN-28PT. Finally, the dynamic effects of phase transitions and thermal expansion in PMN-28PT undergoing the Olsen cycle were elucidated. Both the energy and power densities increased with increasing cycle frequency thanks to a tetragonal to cubic phase transition. Moreover, the resulting thermal expansion provided additional energy density generation from the Olsen cycle.

The second objective was met by conceiving and demonstrating two novel thermomechan-

ical power cycles capable of simultaneously harvesting waste heat and/or mechanical energy. These cycles were also performed on PMN-28PT. The first cycle was able to generate larger power densities and exhibited larger material efficiencies than the Olsen cycle by taking advantage of the piezoelectric response of the material. Indeed, the sample was subjected to a compressive stress to force the phase transitions more rapidly during the cycle. The energy density of this cycle was nearly independent of cycle frequency, while the power density and material efficiency increased with increasing cycle frequency. Both the generated energy and power densities increased with increasing compressive stress. The second cycle consisted of a thermally-biased mechanical power cycle capable of harvesting mechanical energy under a thermal bias. This cycle was able to generate larger power densities and exhibited larger material efficiencies than the first thermomechanical cycle by eliminating cyclic heating and cooling. It also generated significantly larger power densities than alternative mechanical energy conversion methods. The maximum performance was achieved with a thermal bias of 85^{o}C so that the material underwent a tetragonal to orthorhombic phase transitions sequence during the cycle. Finally, a physical model predicting the energy and power densities of the new thermally-biased mechanical power cycle was derived and validated against experimental data. It can be used to predict the energy and power densities for any material based on their dielectric properties and the operating electric fields, temperature, and frequency.

8.2 Recommendations

Thermal, mechanical, and thermomechanical to electrical energy conversion using ferroelectric materials are technologies in their infancy. In order to make them viable and practical, there are a number of issues that require further research attention. Recommendations and suggestions for future research are as follows.

Improvements in cycle performance

This study demonstrated two new energy conversion cycles performed on PMN-28PT. However, there are many other promising ferroelectric materials available that may outperform PMN-28PT. The ideal material should possess (i) large electromechanical coupling as well as (ii) large saturation polarization, (iii) large electric breakdown field, and (iv) fast phase transitions. The energy density of a ferroelectric material undergoing the cycles discussed in this study can be improved by increasing the change in electric displacement it experiences during the cycle. The latter is related to the magnitude of the saturation polarization of the material. Therefore, materials with large saturation polarizations are very desirable. In addition, the energy density of these cycles can also be improved by increasing the electric field span E_H-E_L. This can be achieved by increasing the high electric field E_H in excess of 1 MV/m. Furthermore, the material efficiency and power density can be improved by minimizing the energy and time required to depolarize the material at large electric field. Therefore, materials that quickly and easily depole need to be identified.

Moreover, the two new energy conversion cycles were performed with uniaxial stress applied in the direction parallel to poling. This type of loading was successful in depoling the material. However, the material efficiency and power densities may be improved by exploring different loading and poling configurations. For example, loading the material perpendicular to the poling direction during processes 4-1 and 1-2 would increase the electric displacement achieved during these two processes. In addition, hydrostatic pressure occurring in all directions could be used during process 2-3 to induce a depolarized state.

Prototypical devices for potential applications

The two new cycles presented in this study were capable of achieving large material efficiencies. However, the efficiency of devices implementing the cycles is expected to be much lower. Several prototypical pyroelectric energy converters[20–22,24,36,46] implementing the Olsen cycle have been built that utilized laminar forced convection between a working fluid and the py-

roelectric sample. Recently, others have developed self-sustaining MEMS scale devices that utilized transient heat conduction.[39,40] Similarly, devices need to be developed to implement the novel cycles presented in this study. They should be designed to perform the cycles in a specific application. Potential applications include harvesting wasted energy from electricity generation or combustion based systems as well as transportation systems. Indeed, electricity generation and moving vehicles have an electricity source and waste both thermal and mechanical energy. Thus, the new cycles can be implemented in these systems to increase their energy conversion efficiencies or to power sensors to better monitor and control them.

Develop advanced power electronics for harvesting the generated power

The cycles presented in this study are capable of generating large power relative to passive energy conversion. However, the power is generated in series with a high voltage power supply. This presents challenges in harvesting the generated power without simultaneously drawing power from the high voltage power supply. There are a number of circuits that have been demonstrated to harvest the energy generated by constant electric field systems.[43,141] These circuits include (i) a pseudo-piezoelectric energy harvesting device consisting of a synchronized switch harvesting on inductor (SSHI)[43,141] and (ii) a wireless identification and sensing platform (WISP).[142] These circuits should be adapted, modeled, and implemented experimentally to harvest and condition the electrical energy generated by the new cycles for use and storage.

APPENDIX A

Phase Transitions and Thermal Expansion in Pyroelectric Energy Conversion (Supplementary Material)

A.1 Thermal analysis

The lumped capacitance approximation[105] can be used to predict the sample temperature $T_{PE}(t)$ after it is transferred from the hot silicone oil bath at 140^{o}C to the cold one at 22^{o}C during the Olsen cycle. It is valid when the Biot number, defined as $Bi = h(t)L/k$, is less than 0.1 where $h(t)$ is the heat transfer coefficient, k is the thermal conductivity of the sample in W/m·K, and L is its characteristic length defined as $\mathcal{V}/A_s$ where A_s and $\mathcal{V}$ are the surface area and volume of the sample, respectively. They are such that A_s=1.1 cm^2 and $\mathcal{V}$=0.075 cm^3. Then, the overall energy balance equation governing the sample temperature can be expressed as

$$-h(t)A_s\left[T_{PE}(t)-T_C\right]=\rho c_p\,\mathcal{V}\frac{\mathrm{d}T_{PE}}{\mathrm{d}t} \tag{A.1}$$

where ρ and c_p are the density (in kg/m^3) and specific heat capacity (in J/kg·K) of the sample and t is the time. The time-dependent heat transfer coefficient $h(t)$ due to natural convection around a PMN-28PT cube of 5 mm side length was estimated based on a correlation for the Nusselt number Nu given by[135]

$$Nu(t)=\frac{h(t)L^*}{k_f}=6.65+0.623\left[\frac{Ra(t)}{F(Pr_f)}\right]^{0.261} \tag{A.2}$$

where $Ra(t)$ is the Rayleigh number and Pr_f is the Prandtl number of the fluid. They are given by[135]

$$Ra(t) = \frac{Pr_f \alpha_f g[T_{PE}(t) - T_C]L^{*3}}{\nu_f^2} \quad \text{and} \quad Pr_f = \frac{\nu_f \rho_f c_{p,f}}{k_f} \tag{A.3}$$

Here, the subscript f refers to the fluid and ρ_f, ν_f, $c_{p,f}$, and k_f are the fluid density, kinematic viscosity (in m^2/s), specific heat, and thermal conductivity, respectively. In addition, α_f is the thermal expansion coefficient of the fluid and g is equal to 9.81 m/s^2. The parameter L^* is given by $L^* = 3S\pi^{-0.5}$ where S is the side length of the cube oriented so that the gravity vector is normal to one of its faces.[135] Finally, the function $F(Pr_f)$ is given by[143]

$$F(Pr_f) = [1 + (0.492/Pr_f)^{9/16}]^{16/9} \tag{A.4}$$

Combining Equations (A.2) to (A.4) and integrating the differential Equation (A.1) with respect to time yields the following expression for the sample temperature $T_{PE}(t)$ as

$$T_{PE}(t) = \left[\frac{\kappa(t)h_0}{1 - \kappa(t)\gamma}\right]^{1/0.261} + T_C \tag{A.5}$$

where the parameters $\kappa(t)$, h_0, and γ are given by

$$\kappa(t) = \frac{(T_H - T_C)^{0.261}}{h_0 + \gamma(T_H - T_C)^{0.261}} exp\left(\frac{-0.261 h_0 A_s t}{\rho c_p V}\right), \tag{A.6}$$

$$h_0 = \frac{6.65 k_f}{L^*}, \quad \text{and} \quad \gamma = \frac{0.623 k_f}{L^*}\left[\frac{Pr \alpha_f g L^{*3}}{\nu_f^2 F(Pr_f)}\right]^{0.261}$$

The fluid properties were those of 500 cSt silicone oil[144] and were such that ρ_f = 960 kg/m^3, ν_f = 500×10^{-6} m^2/s, $c_{p,f}$ = 1473 J/kg·K, α_f = 9.6×10^{-4}, and k_f = 0.1 W/m·K. The maximum heat transfer coefficient occurred at t=0 s and was equal to 100 W/m^2·K corresponding to a maximum Biot number Bi=0.023. This confirms the validity of the lumped capacitance approximation.

The density ρ and specific heat c_p of the PMN-28PT single crystal were taken as those of PMN-25PT single crystal and equal to 8000 kg/m^3 and 350 J/kg·K, respectively.[145] The thermal conductivity was taken as that of PMN-34PT[146] equal to 3.01 W/m·K at the arithmetic mean of the initial and ambient temperatures T_H and T_C, respectively. Then, this

thermal model predicted the sample temperature after 17 seconds in the cold bath to be T_{PE}(17 s)=74^{o}C. This confirms that the sample did not reach the cold bath temperature. Given the uncertainties in the correlation and material properties, this temperature prediction is acceptable, but D-E loops appear to provide a more accurate estimate of the sample temperature.

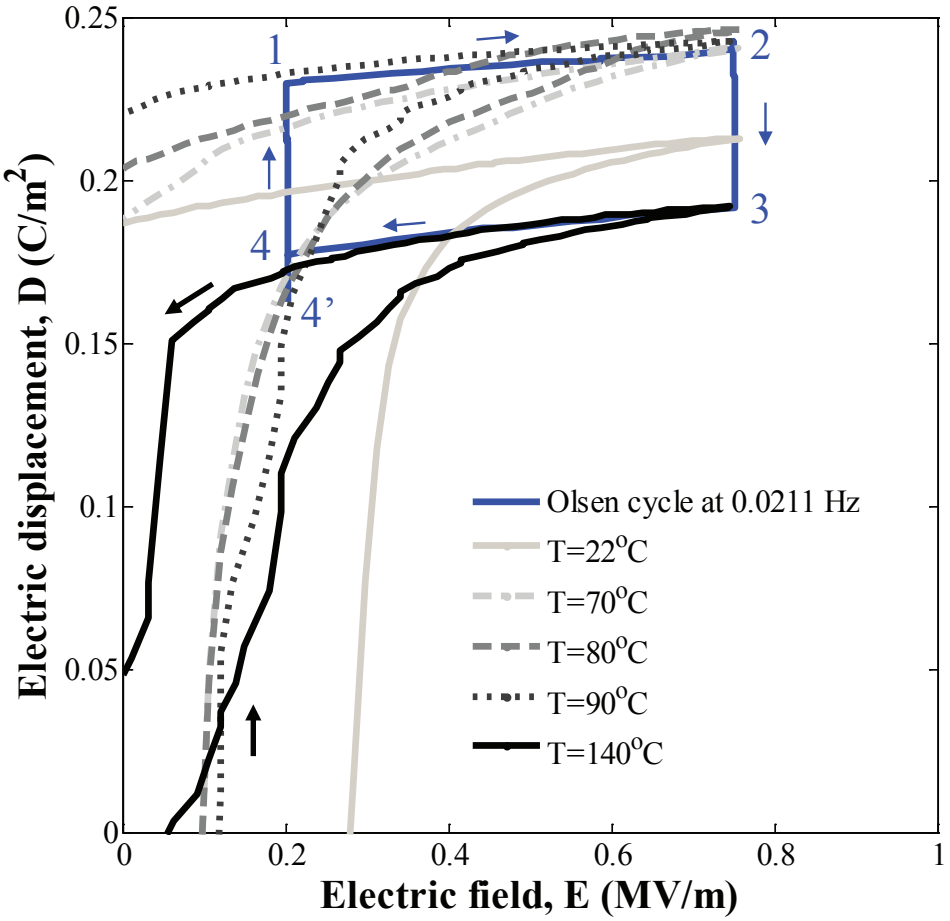

Figure A.1: Isothermal bipolar D-E loops at T=22, 80, 90, and 140^{o}C and experimental Olsen cycle at 0.0211 Hz for PMN-28PT with E_L=0.2 MV/m, E_H=0.75 MV/m, T_C=22^{o}C, and T_H=140^{o}C.

Figure A.1 shows the Olsen cycles performed at 0.0211 Hz as well as the D-E loops at 22, 70, 80, 90, and 140^{o}C. It is evident that the Olsen cycle at 0.0211 Hz followed the path

of the D-E loop at 90^{o}C more closely than those at 70 or 80^{o}C during process 1-2. This indicates that the sample temperature did not reach 70 or 80^{o}C during process 4-1 of the Olsen cycle at 0.0211 Hz.

APPENDIX B

A Novel Thermally-Biased Mechanical Energy Conversion Cycle (Supplementary Material)

B.1 Effect of frequency (supplement)

Figure B.1 shows the electric displacement variations $D(t)$-D_4 versus time t for representative power cycles performed at frequency 0.5, 1, and 2 Hz. The bias-temperature T_b was maintained at 80^{o}C, the low and high electric fields E_L and E_H were set at 0.2 and 0.8 MV/m, and the compressive stress was σ_H=18.81 MPa. The states of the cycle correspond to those shown in Figure 7.1. The time rate of change in electric displacement dD/dt during process 4-1 was identical for all three cycle frequencies. At frequency 0.5 Hz, D(t)-D_4 reached an equilibrium value during both process 4-1 and 2-3. However, the change in electric displacement between states 2 and 4 (D_2-D_4) at frequency 1 and 2 Hz was 90 and 84% smaller than that at 0.5 Hz. Doubling the cycle frequency from 0.5 to 1 Hz resulted in 10% reduction in energy density N_D but an 80% increase in power density P_D. Furthermore, Figure B.1 demonstrates that the time rate of change of electric displacement dD/dt during the electric field increase of process 1-2 was similar for all cycle frequencies while the time rate of change in electric field dE/dt ranged from 1.2 to 4.8 MV/m·s for frequency ranging from 0.5 to 2 Hz, respectively. This result indicates that the change in electric displacement during electric poling and de-poling was independent of dE/dt for the frequencies considered. This is consistent with the conclusion reached previously for PZN-4.5PT[34] and observations previously made from Figure 7.5. Thus, the properties extracted from the D-E loops at 0.1 Hz corresponding to dE/dt equal to 0.3 MV/m·s can be used in the model of Equation (7.2)

to predict the power density of the cycle.

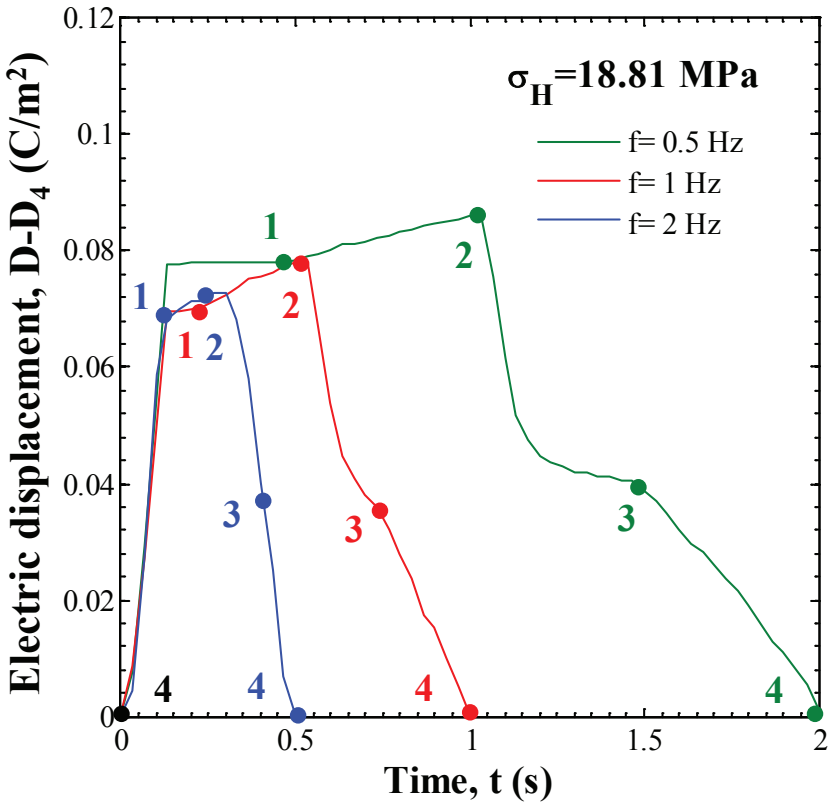

Figure B.1: Experimentally measured electric displacement $D(t)$-D_4 versus time t for the new power cycle for frequency ranging from 0.5 to 2 Hz with compressive stress σ_H=18.81 MPa. The bias-temperature T_b was maintained at 80^{o}C. The low and high electric fields E_L and E_H were set at 0.2 and 0.8 MV/m.

References

[1] U.S. Census Bureau, "U.S. and world population clocks", http://www.census.gov/main/www/popclock.html, July 11, 2012.

[2] The United Nations Department of Economics and Social Affairs, "United nations press release", http://esa.un.org/unpd/wpp/other-information/Press_Release_WPP2010.pdf, May 3, 2011.

[3] The United Nations Department of Economics and Social Affairs, "World urbanization prospects, the 2009 revision, highlights", http://esa.un.org/unpd/wup/Documents/WUP2009_Highlights_Final.pdf, March 2010.

[4] S.R. Anton and H.A Sodano, "A review of power harvesting using piezoelectric materials (2003-2006)", *Smart Materials and Structures*, vol. 16, pp. R1–R21, 2007.

[5] G. Despesse, J.J. Chaillout, S. Boisseau, and C. Jean-Mistral, *Energy Autonomous Micro and Nano Systems*, chapter Mechanical Energy Harvesting, John Wiley & Sons, Inc., Hoboken, NJ, 2012.

[6] S. Roundy and P.K. Wright, *Energy Scavenging for Wireless Sensor Networks: With Special Focus on Vibrations*, Kluwer Academic Publishers, Boston, MA, 2004.

[7] S.P. Beeby, M.J. Tudor, and N.M. White, "Energy harvesting virbation sources for microsystems applications", *Measurement Science and Technology*, vol. 17, pp. R175–R195, 2006.

[8] W.C. Turner and S. Doty, *Energy Management Handbook*, Fairmont Press, 6^{th} edition, 2007.

[9] M.J. Moran and H.N. Shapiro, *Fundamentals of Engineering Thermodynamics, 5th edition*, John Wiley and Sons, New York, NY, 2004.

[10] Lawrence Livermore National Laboratory and Department of Energy, "U.S. Energy Flow Trends - 2012", May 2013.

[11] C.F. Taylor, *The Internal Combustion Engine in Theory and Practice - Chapter 8: Heat Losses*, The MIT Press, Cambridge, MA, 1985.

[12] C.R. Bowen, H.A. Kim, P.M. Weaver, and S. Dunn, "Piezoelectric and ferroelectric materials and structures for energy harvesting applications", *Energy and Environmental Science*, vol. in press, 2013.

[13] A. Erturk and D.J. Inman, Eds., *Piezoelectric energy harvesting*, John Wiley & Sons, Inc., Hoboken, NJ, 2011.

[14] M.A. Rosen, M.N. Le, and L. Dincer, "Efficiency analysis of a cogeneration and district energy system", *Applied Thermal Engineering*, vol. 25, no. 1, pp. 147–159, 2005.

[15] D.G. Thombare and S.K. Verma, "Technological development in the Stirling cycle engines", *Renewable and Sustainable Energy Reviews*, vol. 12, pp. 1–38, 2008.

[16] B.T. Liu, K.H. Chien, and C.C. Wang, "Effect of working fluids on organic rankine cycle for waste heat recovery", *Energy*, vol. 29, no. 8, pp. 1207 – 1217, 2004.

[17] H. Chen, D.Y. Goswami, and E.K. Stefanakos, "A review of thermodynamic cycles and working fluids for the conversion of low-grade heat", *Renewable and Sustainable Energy Reviews*, vol. 14, pp. 3059–3067, 2010.

[18] S.B. Riffat and X. Ma, "Thermoelectrics: a review of present and potential applications", *Applied Thermal Engineering*, vol. 23, pp. 913–935, 2003.

[19] M. Zebarjadi, K. Esfarjani, M.S. Dresselhaus, Z.F. Ren, and G. Chen, "Perspectives on thermoelectrics: from fundamentals to device applications", *Energy and Environmental Science*, vol. 5, pp. 5147–5162, 2012.

[20] R.B. Olsen, D.A. Bruno, J.M. Briscoe, and W.F. Butler, "A pyroelectric energy converter which employs regeneration", *Ferroelectrics*, vol. 38, pp. 975–978, 1981.

[21] R.B. Olsen, "Ferroelectric conversion of heat to electrical energy - a demonstration", *Journal of Energy*, vol. 6, pp. 91–95, 1982.

[22] R.B. Olsen and D.D. Brown, "High-efficiency direct conversion of heat to electrical energy related pyroelectric measurements", *Ferroelectrics*, vol. 40, pp. 17–27, 1982.

[23] R.B. Olsen and D.A. Bruno, "Pyroelectric conversion materials", in *Proceedings of the 21st Intersociety Energy Conversion Engineering Conference, American Chemical Society*, San Diego, CA, August 25-29, 1986, pp. 89–93.

[24] R.B. Olsen, D.A. Bruno, and J.M. Briscoe, "Cascaded pyroelectric energy converter", *Ferroelectrics*, vol. 59, pp. 205–219, 1984.

[25] R.B. Olsen, D.A. Bruno, and J.M. Briscoe, "Pyroelectric conversion cycles", *Journal of Applied Physics*, vol. 58, pp. 4709–4716, 1985.

[26] M. Ikura, "Conversion of low-grade heat to electricity using pyroelectric copolymer", *Ferroelectrics*, vol. 267, pp. 403–408, 2002.

[27] L. Kouchachvili and M. Ikura, "High performance P(VDF-TrFE) copolymer for pyroelectric conversion", *U.S. Patent*, , no. 7,323,506, 2006.

[28] L. Kouchachvili and M. Ikura, "Improving the efficiency of pyroelectric conversion", *International Journal of Energy Research*, vol. 32, pp. 328–335, 2008.

[29] A. Navid, D. Vanderpool, A. Bah, and L. Pilon, "Towards optimization of a pyroelectric energy converter for harvesting waste heat", *International Journal of Heat and Mass Transfer*, vol. 53, no. 19-20, pp. 4060 – 4070, 2010.

[30] A. Navid and L. Pilon, "Pyroelectric energy harvesting using Olsen cycles in purified and porous poly(vinylidene fluoride-trifuoroethylene) thin films", *Smart Materials and Structures*, vol. 20, no. 2, pp. 025012, 2011.

[31] G. Sebald, L. Seveyrat, D. Guyomar, L. Lebrun, B. Guiffard, and S. Pruvost, "Electrocaloric and pyroelectric properties of $0.75Pb(Mg_{1/3}Nb_{2/3})O_3$-$0.25PbTiO_3$ single crystals", *Journal of Applied Physics*, vol. 100, pp. 124112 1–6, 2006.

[32] D. Guyomar, S. Pruvost, and G. Sebald, "Energy harvesting based on FE-FE transition in ferroelectric single crystals", *IEEE Transactions on Ultrasonics, Ferroelectrics, and Frequency Control*, vol. 55, pp. 279–285, 2008.

[33] A. Khodayari, S. Pruvost, G. Sebald, D. Guyomar, and S. Mohammadi, "Nonlinear pyroelectric energy harvesting from relaxor single crystals", *IEEE Transactions on Ultrasonics, Ferroelectrics, and Frequency Control*, vol. 56, pp. 693 –699, 2009.

[34] H. Zhu, S. Pruvost, D. Guyomar, and A. Khodayari, "Thermal energy harvesting from $Pb(Zn_{1/3}Nb_{2/3})_{0.955}Ti_{0.045}O_3$ single crystals phase transitions", *Journal of Applied Physics*, vol. 106, no. 12, pp. 124102, 2009.

[35] J. Fang, H. Frederich, and L. Pilon, "Harvesting nanoscale thermal radiation using pyroelectric materials", *ASME Journal of Heat Transfer*, vol. 132, no. 9, pp. 092701, 2010.

[36] H. Nguyen, A. Navid, and L. Pilon, "Pyroelectric energy converter using co-polymer P(VDF-TrFE) and Olsen cycle for waste heat energy harvesting", *Applied Thermal Engineering*, vol. 30, no. 14-15, pp. 2127–2137, 2010.

[37] A. Cuadras, M. Gasulla, and V. Ferrari, "Thermal energy harvesting through pyroelectricity", *Sensors and Actuators A: Physical*, vol. 158, no. 1, pp. 132 – 139, 2010.

[38] P. Mane, J. Xie, K. Leang, and K. Mossi, "Cyclic energy harvesting from pyroelectric materials", *IEEE Transactions on Ultrasonics, Ferroelectrics, and Frequency Control*, vol. 58, no. 1, pp. 10–17, 2011.

[39] S. Hunter, N. Lavrik, T. Bannuru, S. Mostafa, S. Rajic, P. Datskos, edited by N. Dhar, P. Wijewarnasuriya, and A. Dutta, "Development of MEMS based pyroelectric thermal energy harvesters", in *Energy Harvesting and Storage: Materials, Devices, and Applications II*, Orlando, FL, April 25 2011, p. 80350V.

[40] S.K.T. Ravindran, T. Huesgen, M. Kroener, and P. Woias, "A self-sustaining micro thermomechanic-pyroelectric generator", *Applied Physics Letters*, vol. 99, no. 10, pp. 104102, 2011.

[41] S.B. Lang, "Pyroelectricity: from ancient curiosity to modern imaging tool", *Physics Today*, vol. 58, pp. 31–36, 2005.

[42] G. Sebald, D. Guyomar, and A. Agbossou, "On thermoelectric and pyroelectric energy harvesting", *Smart Materials and Structures*, vol. 18, pp. 125006, 2009.

[43] D. Guyomar, G. Sebald, E. Lefeuvre, and A. Khodayari, "Toward heat energy harvesting using pyroelectric materials", *Journal of Intelligent Material Systems and Structures*, vol. 20, no. 3, pp. 265–271, 2009.

[44] F.Y. Lee, A. Navid, and L. Pilon, "Pyroelectric waste heat energy harvesting using heat conduction", *Applied Thermal Engineering*, vol. 37, pp. 30–37, 2012.

[45] S.B. Lang and D.K. Das-Gupta, *Handbook of Advanced Electronic and Photonic Materials and Devices*, vol. 4, Academic Press, San Diego, CA, 2001.

[46] R.B. Olsen, D.A. Bruno, and J.M. Briscoe, "Pyroelectric conversion cycle of vinylidene fluoride-trifluoroethylene copolymer", *Journal of Applied Physics*, vol. 57, pp. 5036–5042, 1985.

[47] L. Kouchachvili and M. Ikura, "Pyroelectric conversion-effects of P(VDF-TrFE) preconditioning on power conversion", *Journal of Electrostatics*, vol. 65, pp. 182–188, 2006.

[48] V. Sencadas, S. Lanceros-Mendez, and J.F. Mano, "Characterization of poled and non-poled β-PVDF films using thermal analysis techniques", *Thermocimica Acta*, vol. 424, pp. 201–207, 2004.

[49] B. Chu, X. Zhou, K. Ren, B. Neese, M. Lin, Q. Wang, F. Bauer, and Q.M. Zhang, "A dielectric polymer with high electric energy density and fast discharge speed", *Science*, vol. 313, pp. 334–336, 2006.

[50] F.Y. Lee, H.R Jo, C.S. Lynch, and L. Pilon, "Pyroelectric energy conversion using PLZT ceramics and relaxor-ferroelectric phase transition", *Smart Materials and Structures*, vol. 22, no. 2, pp. 025038, 2013.

[51] G. Cha and Y.S. Ju, "Pyroelectric energy harvesting using liquid-based switchable thermal interfaces", *Sensors and Actuators A: Physical*, vol. 189, pp. 100–1078, 2013.

[52] I.M. McKinley, R. Kandilian, and L. Pilon, "Waste heat energy harvesting using the Olsen cycle on 0.945Pb($Zn_{1/3}Nb_{2/3}$)O_3-0.055$PbTiO_3$ single crystals", *Smart Materials and Structures*, vol. 21, pp. 035015, 2012.

[53] R. Zhang, B. Jiang, and W. Cao, "Orientation dependence of piezoelectric properties of single domain 0.67$PbMg_{1/3}Nb_{2/3}O_3$–0.33 $PbTiO_3$ single crystals", *Applied Physics Letters*, vol. 82, no. 21, pp. 3737–3739, 2003.

[54] Z. Li, Z. Xu, Z. Xi, F. Xiang, and X. Yao, "Thermal expansion characteristics in [001]-oriented PMN-0.32PT single crystals", *Ferroelectrics*, vol. 355, no. 1, pp. 245–251, 2007.

[55] R. Kumar, D. Molin, L. Young, and F. Ke, "New high temperature polymer thin coating for power electronics", *Applied Power Electronics Conference and Exposition*, vol. 2, pp. 1247–1249, 2004.

[56] N. Yasuda, T. Banno, K. Fujita, H. Ohwa, M. Matushita, Y. Yamashita, M. Iwata, and Y. Ishibashi, "Piezoelectric properties of relaxor ferroelectric solid solution single crystals PMN-PT and PZN-PT near MPB under pressures", *Ferroelectrics*, vol. 347, no. 1, pp. 44–49, 2007.

[57] K.B.R. Varma, "Morphology and dielectric properties of fish scales", *Current science*, vol. 59, no. 8, pp. 420–423, 1990.

[58] C. Brown, R. Kell, R. Taylor, and L. Thomas, "Piezoelectric materials, a review of progress", *Component Parts, IRE Transactions on*, vol. 9, no. 4, pp. 193–211, 1962.

[59] F.J. Balta Calleja, A. Gonzalez Arche, T.A. Ezquerra, C. Santa Cruz, F. Batallan, B. Frick, and E. Lopez Cabarcos, "Structure and properties of ferroelectric copolymers of poly(vinylidene fluoride)", *Advances in Polymer Science*, vol. 108, pp. 1–48, 1993.

[60] "IEEE standard on piezoelectricity", *ANSI/IEEE Std 176-1987*, 1988.

[61] M.E. Lines and A.M. Glass, *Principles and Applications of Ferroelectrics and Related Materials*, Clarendon Press, Oxford, UK, 1977.

[62] S.B. Lang, *Sourcebook of Pyroelectricity*, Gordon and Breach, Science Publishers, Inc., New York, NY, 1974.

[63] M.A. Itskovsky, "Pyroelectric hysteresis loop at ferroelectric phase transition", *Journal of Applied Physics*, vol. 85, pp. 4256–4258, 1999.

[64] G.A. Samara, "Ferroelectricity revisited–advances in materials and physics", *Solid State Physics*, vol. 56, pp. 239 – 458, 2001.

[65] F.Y. Lee, "Experimental and analytical studies on pyroelectric waste heat energy conversion", Master's thesis, University of California Los Angeles, 2012.

[66] Z. Li, Z. Xi, Z. Xu, and X. Yao, "Dielectric/ferroelectric response and phase transition of PMN-0.32PT single crystal", *Journal of Materials Science Letters*, vol. 21, pp. 1325–1327, 2002.

[67] N. Bar-Chaim, M. Brunstein, J. Grünberg, and A. Seidman, "Electric field dependence of the dielectric constant of PZT ferroelectric ceramics", *Journal of Applied Physics*, vol. 45, no. 6, pp. 2398–2405, 1974.

[68] H.M. Bao, J.F. Song, J. Zhang, Q.D. Shen, C.Z. Vang, and Q.M. Zhang, "Phase transitions and ferroelectric relaxor behavior in P(VDF-TrFE-CFE) terpolymers", *Macromolecules*, vol. 40, pp. 2371–2379, 2007.

[69] A. Navid, *Pyroelectric Energy Conversion for Waste Heat Harvesting*, PhD thesis, University of California Los Angeles, 2010.

[70] J. Han and W. Cao, "Electric field effects on the phase transitions in [001]-oriented (1-x)Pb($Mg_{1/3}Nb_{2/3}$)O_3-x$PbTiO_3$ single crystals with compositions near the morphotropic phase boundary", *Physical Review B*, vol. 68, pp. 134102, 2003.

[71] N. Srivastava and G.J. Wang, "A theory of double hysteresis for ferroelectric crystals", *Journal of Applied Physics*, vol. 99, pp. 054103, 2006.

[72] W.J. Merz, "Double hysteresis loop of $BaTiO_3$ at the Curie point", *Physical Review*, vol. 91, pp. 513–517, 1953.

[73] M.W. Hooker, *Properties of PZT-Based Piezoelectric Ceramics Between -150 and 250°C*, National Aeronautics and Space Administration, Hampton, VA, NASA contractor report 1998-208708 edition, 1998.

[74] A. Herklotz, J.D. Plumhof, A. Rastelli, O.G. Schmidt, L. Schultz, and K. Dorr, "Electrical characterization of PMN-28%PT(001) crystals used as thin-film substrates", *Journal of Applied Physics*, vol. 108, pp. 094101, 2010.

[75] Q. Wan, C. Chen, and Y.P. Shen, "Effects of stress and electric field on the electromechanical properties of Pb($Mg_{1/3}Nb_{2/3}$)O_3-0.32$PbTiO_3$ single crystals", *Journal of Applied Physics*, vol. 97, pp. 024103 1–5, 2005.

[76] E.A. McLaughlin, T. Liu, and C.S. Lynch, "Relaxor ferroelectric PMN-32PT crystals under stress, electric field and temperature loading: II-33-mode measurements", *Acta Materialia*, vol. 53, no. 14, pp. 4001–4008, 2005.

[77] W. Ren, S.-F. Liu, and B.K. Mukherjee, "Piezoelectric properties and phase transitions of 001-oriented Pb($Zn_{1/3}Nb_{2/3}$)O_3-$PbTiO_3$ single crystals", *Applied Physics Letters*, vol. 80, no. 17, pp. 3174–3176, 2002.

[78] J. Yin, B. Jiang, and W. Cao, "Elastic, piezoelectric, and dielectric properties of 0.995Pb($Zn_{1/2}Nb_{2/3}$)O_3-0.045$PbTiO_3$", *Transactions on Ultrasonics, Ferroelectrics, and Frequency Control*, vol. 1, no. 47, pp. 285–291, 2000.

[79] S. Liu, S. Park, L. Cross, and R. Shrout, "Temperature dependence of electrostriction in rhombohedral Pb($Zn_{1/3}Nb_{2/3}$)O_3-$PbTiO_3$ single crystals", *Journal of Applied Physics*, vol. 92, no. 1, pp. 461–467, 2002.

[80] M. Shen and W. Cao, "Investigation of dipolar defects in (1-x)Pb($Zn_{1/3}Nb_{2/3}$)O_3-x$PbTiO_3$ single crystals using different poling methods", *Journal of Applied Physics*, vol. 101, no. 1, pp. 014105, 2007.

[81] J.S. Forrester, E.H. Kisi, and K.S. Knight, "Phase transitions in PZN-4.5%PT in the range 4.2-450 K", *Physica B*, vol. 385-386, pp. 160–162, 2006.

[82] W.S. Chang, L.C. Lim, P. Yang, H.O. Moser, F.T. Wang, C.T. Tseng, and C.S. Tu, "Phase transformations in poled PZN-4.5%PT single crystals revealed by combined property measurements and high-resolution diffraction technique", *Journal of Applied Physics*, vol. 104, no. 5, pp. 054102, 2008.

[83] J.J. Lima-Silva, I. Guedes, J. Mendes Filho, A.P. Ayala, M.H. Lente, J.A. Eiras, and D. Garcia, "Phase diagram of the relaxor (1-x)$Pb(Zn_{1/3}Nb_{2/3})O_3$-x $PbTiO_3$ investigated by dielectric and Raman spectroscopies", *Solid State Communications*, vol. 131, no. 2, pp. 111–114, 2004.

[84] M. Davis, D. Damjanovic, and N. Setter, "Temperature dependence of the direct piezoelectric effect in relaxor-ferroelectric single crystals: intrinsic and extrinsic contributions", *Journal of Applied Physics*, vol. 100, no. 8, pp. 084103, 2006.

[85] A. Benayad, A. Hajjaji, B. Guiffard, L. Lebrun, and D. Guyomar, "Electromechanical properties versus polarization and vibration directions of $Pb((Zn_{1/3}Nb_{2/3})_{0.955}Ti_{0.045})O_3$ single crystals grown by the modified Bridgman method", *Journal of Applied Physics*, vol. 40, no. 3, pp. 840–845, 2007.

[86] A.E. Renault, H. Dammak, G. Calvarin, and P. Gaucher, "Electric-field-induced orthorhombic phase in $Pb[(Zn_{1/3}Nb_{2/3})_{0.955}Ti_{0.045}]O_3$ single crystals", *Journal of Applied Physics*, vol. 97, no. 4, pp. 044105, 2005.

[87] S.E. Park and T.R. Shrout, "Ultrahigh strain and piezoelectric behavior in relaxor based ferroelectric single crystals", *Journal of Applied Physics*, vol. 82, no. 4, pp. 1804, 1997.

[88] Z.-G. Ye and M. Dong, "Morphotropic domain structures and phase transitions in relaxor-based piezo-/ferroelectric (1-x)$PbMg_{1/3}Nb_{2/3}O_3$-x$PbTiO_3$ single crystals", *Journal of Applied Physics*, vol. 87, no. 5, pp. 2312, 2000.

[89] D. Viehland, A. Amin, and J.F. Li, "Piezoelectric instability in <011>-oriented $Pb(B_{1/3}{}^{I}B_{2/3}{}^{II})O_3$-$PbTiO_3$ crystals", *Applied Physics Letters*, vol. 79, no. 7, pp. 1006–1008, 2001.

[90] X. Zhao, B. Fang, H. Cao, Y. Guo, and H. Luo, "Dielectric and piezoelectric performance of PMN-PT single crystals with compositions around the MPB: influence of composition, poling field and crystal orientation", *Materials Science and Engineering: B*, vol. 96, no. 3, pp. 254–262, 2002.

[91] J. Chen, H. Fan, S. Ke, X. Chen, C. Yang, and P. Fang, "Relaxor behavior and dielectric properties of lead magnesium niobate-lead titanate thick films prepared by electrophoresis deposition", *Journal of Alloys and Compounds*, vol. 478, pp. 853–857, 2009.

[92] D. Zhou, F. Wang, L. Luo, J. Chen, W. Ge, X. Zhao, and H. Luo, "Characterization of complete electromechanical constants of rhombohedral $0.72Pb(Mg_{1/3}Nb_{2/3})$-$0.28PbTiO_3$ single crystals", *Journal of Physics D: Applied Physics*, vol. 41, pp. 185402, 2008.

[93] Y. Guo, H. Luo, D. Ling, H. Xu, T. He, and Z. Yin, "The phase transition sequence and the location of the morphotropic phase boundary region in (1-x)$Pb(Mg_{1/3}Nb_{2/3})O_3$-x$PbTiO_3$ single crystal", *Journal of Physics: Condensed Matter*, vol. 15, pp. L77–L82, 2003.

[94] F. Bai, N. Wang, J. Li, D. Viehland, P.M. Gehring, G. Xu, and G. Shirane, "X-ray and neutron diffraction investigations of the structural phase transformation sequence under electric field in $0.7Pb(Mg_{1/3}Nb_{2/3})$-$0.3PbTiO_3$ crystal", *Journal of Applied Physics*, vol. 96, no. 3, pp. 1620–1627, 2004.

[95] V.H. Schmidt, R. Chien, I.-C. Shih, and C.-S. Tu, "Polarization rotation and monclinic phase in relaxor ferroelectric PMN-PT crystal", in *AIP Conference Proceedings*, 2003, vol. 677, pp. 160–167.

[96] K.G. Webber, H.C. Robinson, Jr. G.A. Rossetti, and C.S. Lynch, "A distributed step-like switching model of the continuous field-driven phase transformations observed in PMN-xPT relaxor ferroelectric single crystals", *Acta Materialia*, vol. 56, pp. 2744–2749, 2008.

[97] R. Kandilian, A. Navid, and L. Pilon, "Pyroelectric energy harvesting capabilities of PMN-PT near the morphotropic phase boundary", *Smart Materials and Structures*, vol. 20, pp. 055020, 2011.

[98] F.Y. Lee, S. Goljahi, I.M. McKinley, C.S. Lynch, and L. Pilon, "Pyroelectric waste heat energy harvesting using relaxor ferroelectric 8/65/35 PLZT and the Olsen cycle", *Smart Materials and Structures*, vol. 21, pp. 025021, 2012.

[99] T. Chin, F.Y. Lee, I.M. McKinley, S. Goljahi, C.S. Lynch, and L. Pilon, "Pyroelectric waste heat energy harvesting using 9.5/65/35 PLZT ceramics", *IEEE Transactions on Ultrasonics, Ferroelectrics, and Frequency Control*, accepted.

[100] I.M. McKinley and L. Pilon, "Phase transitions and thermal expansion in pyroelectric energy conversion", *Applied Physics Letters*, vol. 102, pp. 023906, 2013.

[101] A. Navid and L. Pilon, "Pyroelectric energy harvesting using Olsen cycle in purified and porous poly(vinylidene fluoride-trifuoroethylene [P(VDF-TrFE)] thin films", *Smart Materials and Structures*, vol. 20, pp. 025012, 2011.

[102] M. Ozgul, *Polarization Switching and Fatigue Anisotropy in Relaxor-Lead Titanate Ferroelectric Single Crystals*, PhD thesis, The Pennsylvania State University, 2003.

[103] B. Liščić, "Heat transfer control during quenching", *Materials and Manufacturing Processes*, vol. 24, pp. 879–886, 2009.

[104] J. Van Randerot and R.E. Settengton, *Piezoeletric Ceramics*, Mullard Ltd., London, UK, 2^{nd} edition, 1974.

[105] F.P. Incropera, D.P. DeWitt, T. Bergman, and A. Lavine, *Fundamentals of Heat and Mass Transfer*, John Wiley and Sons, Ltd., New York, NY, 6^{th} edition, 2006.

[106] M. Sitti, D. Campolo, J. Yan, and R. Fearing, "Development of PZT and PZN-PT based unimorph actuators for micromechanical flapping mechanisms", in *Proceedings of IEEE Intl Conf on Robotics and Automation, Seoul, Korea*, 2001, vol. 4, pp. 21–26.

[107] B. Fang, Q. Du, L. Zhou, X. Zhao, H. Xu, and H. Luo, "Structural phase transition and physical properties of tetragonal $0.85Pb(Zn_{1/3}Nb_{2/3})O_3$-$0.15PbTiO_3$ single crystals", *Journal of Applied Physics*, vol. 106, no. 7, pp. 074110–1, 2009.

[108] A. Pandey, O. Gottlieb, O. Shtempluck, and E. Buks, "Performance of an AuPd micromechanical resonator as a temperature sensor", *Applied Physics Letters*, vol. 96, pp. 203105–1, 2010.

[109] K.G. Webber, D. Hopkinson, and C.S. Lynch, "Application of a classical lamination theory model to the design of piezoelectric composite unimorph actuators", *Journal of Intelligent Materials Systems and Structures*, vol. 17, pp. 29–34, 2006.

[110] W. Dong, P. Finkel, A. Amin, and C.S. Lynch, "Mechanical energy harvesting utilizing phase transition in 32 mode relaxor-ferroelectric PIN-PMN-PT single crystals", in *SPIE Smart Structures and Materials+ Nondestructive Evaluation and Health Monitoring*. International Society for Optics and Photonics, 2012, pp. 834308–834308.

[111] I.M. McKinley, F.Y. Lee, and L. Pilon, "A novel thermoelectromechanical energy conversion cycle", *Applied Energy*, under review.

[112] I.M. McKinley, S. Goljahi, C.S. Lynch, and L. Pilon, "A novel thermally-biased mechanical energy conversion cycle", *Energy Conversion and Management*, in press.

[113] Z. Feng, D. Lin, H. Luo, S. Li, and D. Fang, "Effect of uniaxial stress on the electromechanical response of <001>-oriented $Pb(Mg_{1/3}Nb_{2/3})O_3$-$PbTiO_3$ crystals", *Journal of Applied Physics*, vol. 97, pp. 024103 1–5, 2005.

[114] E.A. McLaughlin, T. Liu, and C.S. Lynch, "Relaxor ferroelectric PMN-32PT crystals under stress and electric field loading: I-32 mode measurements", *Acta Materialia*, vol. 52, pp. 3849–3857, 2004.

[115] D. Viehland and J. Powers, "Electromechanical coupling coefficient of <001>-oriented of $Pb(Mg_{1/3}Nb_{2/3})O_3$-$PbTiO_3$ crystals: Stress and temperature independence", *Applied Physics Letters*, vol. 78, pp. 3112–3114, 2001.

[116] D. Viehland, J. Li, E.A. McLauglin, J. Powers, R. Janus, and H. Robinson, "Effect of uniaxial stress on the large-signal electromechanical properties of electrostrictive and

piezoelectric lead magnesium niobate lead titanate ceramics", *Applied Physics Letters*, vol. 95, pp. 1969–1972, 2004.

[117] L.S. Kamzina and H. Luo, "Influence of the electric field on structural transformations and phase boundary for $PbMg_{1/3}Nb_{2/3}O_3$-x$PbTiO_3$ single crystals", *Physics of the Solid State*, vol. 51, no. 11, pp. 2316–2323, 2009.

[118] Y. Tang and H. Luo, "Inverstigation of the electrical properties of (1-x)$Pb(Mg_{1/2}Nb_{2/3})O_3$-x$PbTiO_3$ single crystals with special reference to pyroelectric detection", *Journal of Physics D: Applied Physics*, vol. 42, pp. 075406, 2009.

[119] E.V. Colla, N.K. Yushin, and D. Viehland, "Dielectric properties of $(PMN)_{1-x}(PT)_x$", *Journal of Applied Physics*, vol. 83, no. 6, pp. 3298–3304, 1998.

[120] J. Suchanicz and A. Kania, "Effects of uniaxial pressure on the dielectric properties of (1-x)$PbMg_{1/3}Nb_{2/3}O_3$-$x$$PbTiO_3$ single crystals (x= 0.28 and 0.38)", *Ferroelectrics*, vol. 426, pp. 251–258, 2012.

[121] A. Slodczyk, *Structural, Dielectric and Vibrational Studies of Lead Magnesium Niobate - Lead Titanate (1-x)$PbMg_{1/3}Nb_{2/3}O_3$-x$PbTiO_3$ Solid Solutions*, PhD thesis, University of Silesia, 2006.

[122] G. Bhikshamaiah, S. Annapurna, and A.K. Singh, "Determination of lattice parameters and thermal expansion of $CuGe_2P_3$ + 0.2 Ge_3P_4 at elevated temperatures", *Crystal Research and Technology*, vol. 41, no. 9, pp. 911–913, 2006.

[123] Z. Kutnjak and R. Blinc, "Electric field induced critical points and polarization rotations in relaxor ferroelectrics", *Physical Review B*, vol. 76, pp. 104102, 2007.

[124] F. Preisach, "Über die magnetische Nachwirkung", *Zeitschrift für Physik*, vol. 94, pp. 277–307, 1935.

[125] B. Jiang, J.C. Lee, P. Zurcher, and Jr. R.E Jones, "Modeling ferroelectric capacitor switching using a parallel-elements model", 1997, vol. 16, pp. 199–208.

[126] Y.-J. Zhang, T.-L. Ren, and L.-T. Liu, "An improved ferroelectric capacitor compact model based on probability theory for circuits simulation", *Integrated Ferroelectrics*, vol. 95, pp. 199–204, 2007.

[127] I. Schultz, H. Goebel, and M. Ullman, "Modelling polarisation of ferroelectrid SBT capacitors including temperature dependence", *Electronics Letters*, vol. 37, no. 20, pp. 1216–1217, 2001.

[128] E. Supriyanto, I. Schultz, M. Ullmann, and H. Goebel, "Ferroelectric capacitor compact model including dynamic and temperature behavior", in *Proceedings of the 13th IEEE International Symposium on Applications of Ferroelectrics, 2002.*, Nara, Japan, May 28 2002, IEEE, pp. 61–64.

[129] C.B. Sawyer and C.H. Tower, "Rochelle salt as a dielectric", *Physical Review*, vol. 35, pp. 269–275, 1930.

[130] A. Navid, C.S. Lynch, and L. Pilon, "Purified and porous poly(vinylidene fluoride-trifluoroethylene) thin films for pyroelectric infrared sensing and energy harvesting", *Smart Materials and Structures*, vol. 19, pp. 055006, 2010.

[131] S.M. Sarge, W. Hemminger, E. Gmelin, G.W.H. Hohne, H.K. Cammenga, and W. Eysel, "Metrologically based procedure for the temperature, heat and heat flow rate calibration of DSC", *Journal of Thermal Analysis*, vol. 49, pp. 1125–1134, 1997.

[132] Y.S. Touloukian and C.Y. Ho, *Thermophysical Properties of Matter, Vol. 4, Specific Heat of Metallic Solids*, Plenum Press, New York, NY, 1972.

[133] J.C. Piquette, A.H. Amin, and E.A. McLaughlin, "Model of the polarization response of single-crystal lead magnesium niobate-lead titanate for transducer applications", *Journal of Applied Physics*, vol. 94, no. 8, pp. 5172 –5181, 2003.

[134] Z. Kutnjak, J. Petzelt, and R. Blinc, "The giant electromechanical response in ferroelectric relaxors as a critical phenomenon", *Nature Letters*, vol. 441, pp. 956–959, 2006.

[135] E.M. Sparrow and A.J. Stretton, "Natural convection from variously oriented cubes and from other bodies of unity aspect ratio", *In. J. Heat and Mass Transfer*, vol. 28, pp. 741, 1985.

[136] R.B. Olsen and D. Evans, "Pyroelectric energy conversion: hysteresis loss and temperature sensitivity of a ferroelectric material", *Journal of Applied Physics*, vol. 54, pp. 5941–5944, 1983.

[137] C.S. Lynch, "The effect of uniaxial stress on the electro-mechanical response of 8/65/35 PLZT", *Acta Materialia*, vol. 44, pp. 4137–4139, 1996.

[138] F.P. Beer, Jr. E.R. Johnston, and J.T. DeWolf, *Mechanics of Materials*, McGraw-Hill, New York, NY, 4th edition, 2006.

[139] L. Wang and F.G. Yuan, "Vibration energy harvesting by magnetostrictive material", *Smart Materials and Structures*, vol. 17, pp. 045009, 2008.

[140] P.J. Cottinet, D. Guyomar, M. Lallart, B. Guiffard, and L. Lebrun, "Investigation of electrostrictive polymer efficiency for mechanical energy harvesting", *IEEE Transactions on Ultrasonics, Ferroelectrics, and Frequency Control*, vol. 58, pp. 1842, 2011.

[141] P.J. Cottinet, D. Guyomar, and M. Lallart, "Electrostrictive polymer harvesting using a nonlinear approach", *Sensors and Actuators A*, vol. 172, pp. 497–503, 2011.

[142] D.J. Yeager, A.P. Sample, and J.R. Smith, "WISP: A passively powered UHF RFID tag with sensing and computation", *RFID Handbook: Applications, Technology, Security, and Privacy. CRC Press, Boca Raton, FL*, pp. 261–278, 2008.

[143] S. W. Churchill and H. H. S. Chu, "Correlating equations for laminar and turbulent free convection from a vertical plate", *International Journal Heat and Mass Transfer*, vol. 18, pp. 1323, 1975.

[144] "Dow Corning product information: 200® fluid", 1998, Ref. no. 22-0069N-01.

[145] G. Sebald, S. Pruvost, and D. Guyomar, "Energy harvesting based on Ericsson pyroelectric cycles in a relaxor ferroelectric ceramic", *Smart Materials and Structures*, vol. 17, pp. 1–6, 2008.

[146] D.-M. Zhu and P.D. Han, "Thermal conductivity and electromechanical property of single-crystal lead magnesium niobate titanate", *Applied Physics Letters*, vol. 75, pp. 3868, 1999.